High Speed B5G/6G Communication Network Analysis Using Machine Learning and Queueing Techniques

Thesis for the Degree of Doctor of Philosophy (PhD)

Djamila Talbi

Supervisor: Prof. Dr. Gal Zoltan

UNIVERSITY OF DEBRECEN

Doctoral Council for Natural Sciences and Engineering

Doctoral School of Informatics

Debrecen, 2025

Hereby I declare that I prepared this thesis within the Doctoral Council for Natural Sciences and Engineering, Doctoral School of Informatics, University of Debrecen in order to obtain a PhD Degree in Engineering at Debrecen University.

The results published in the thesis are not reported in any other PhD theses.

Debrecen, 2025.09.04.

……

signature of the candidate

Hereby I confirm that Djamila Talbi candidate conducted her studies with my supervision within the Information Technology Systems and Networks with Industrial Applications Doctoral Program of the Doctoral School of Informatics between 2021 and 2025. The independent studies and research work of the candidate significantly contributed to the results published in the thesis.

I also declare that the results published in the thesis are not reported in any other theses.

I support the acceptance of the thesis.

Debrecen, 2025.09.04.

……

signature of the supervisor

HIGH SPEED B5G/6G COMMUNICATION NETWORK ANALYSIS USING MACHINE LEARNING AND QUEUEING TECHNIQUES

Dissertation submitted in partial fulfilment of the requirements for the doctoral (PhD) degree

In Informatics

Written by Talbi Djamila, Master of Science in Telecommunication Systems

Prepared in the framework of the doctoral school of the University of Debrecen

(Information Technology Systems and Networks with Industrial Applications Doctoral program)

Dissertation supervisor: Dr. Gal Zoltan

The official opponents of the dissertation:

Dr. ..... ……..

Dr. ..... ……..

The evaluation board:

chairperson: Dr. ..... ……..

members: Dr. ..... ……..

Dr. ..... ……..

Dr. ..... ……..

Dr. ..... ……..

The date and venue of the dissertation defense:……

ABSTRACT

The rapid evolution of mobile communication systems has brought the research community to the frontier of the sixth-generation wireless networks. The main aim is to bring a network with high data rates, ultra-low latency, massive device connectivity, and high energy efficiency to the real world. 6G represents a technological shift with significant implications for network design and performance optimization. However, as this network operates at extremely high frequencies, this makes the researchers face a lot of challenges, such as modeling, simulation, and analysis, primarily due to the scarcity of real-world deployment and empirical data. This dissertation studies the 6G network to address this gap, as it proposes a comprehensive framework that applies advanced data processing techniques and artificial intelligence integration strategies to better understand and model 6G communication network behaviors.

This work begins by simulating a key MAC layer mechanism known as Adaptive Directional Antenna Protocol for Terahertz, which is specifically tailored for the 6G context. Using the ns-3 simulator integrated with the TeraSim module, we reproduce directional communication scenarios within THz bands. The simulation captures a range of critical Key Performance Indicators such as throughput, delay, packet collision rate, and received power. These KPIs are not only vital for characterizing network performance but also serve as the fundamental input for downstream processing and learning mechanisms.

Following data extraction, a comprehensive preprocessing stage is conducted to extract the hidden informative features and evaluate the complexity of the network behavior. This step includes both classical signal processing and advanced techniques such as Shannon entropy for quantifying uncertainty, empirical mode decomposition and ensemble variant empirical mode decomposition for adaptive multi-scale decomposition, and the marginal Hilbert

spectrum for energy distribution in the time-frequency domain. By doing so, a nuanced behavioral dynamic is revealed that is otherwise hidden in raw performance logs.

The third layer of the methodology involves the application of five AI strategies to leverage the processed data, including unsupervised machine learning methods, supervised learning models, multi-layer transfer learning, generative AI techniques, and reinforcement learning, particularly deep Q-networks. Importantly, given the absence of real-world 6G testbeds and empirical data, the dissertation emphasizes theoretical validation. Comparative metrics, entropy-based measurements, and behavioral symmetry analyses are used to assess the coherence and plausibility of the simulated and AI-generated results. The proposed pipeline thus ensures that each stage from simulation to learning is grounded in logical consistency and system behavior modeling principles.

This dissertation offers a multi-layered framework that advances the current state of research in 6G network modeling by bridging simulation, complexity analysis, and artificial intelligence. The methodology developed herein is not only applicable to 6G research but is also generalized to other high-frequency, high-complexity wireless systems. It lays a robust foundation for future work that will inevitably benefit from the availability of real-world 6G deployment data.

DECLARATION

I, the undersigned Talbi Djamila, hereby declare that I have written this doctoral dissertation myself and have used only the sources referenced within it. I have clearly marked all sections taken from other sources, whether quoted directly or paraphrased, indicating their respective origins.

Debrecen, Hungary, April 29, 2025

Djamila Talbi

ACKNOWLEDGMENTs

First and foremost, I am profoundly grateful to Allah (SWT), the Most Gracious and the Most Merciful, for blessing me with the strength, health, and perseverance to complete this dissertation.

I would like to sincerely thank my supervisor, Prof. Dr. Zoltan Gal, for his invaluable guidance, encouragement, and support throughout my research journey. Their expertise and insightful feedback have been crucial in shaping this work.

My gratitude also extends to the professors and staff of the faculty, whose dedication, knowledge, and assistance have greatly enriched my academic experience.

I am deeply thankful to my beloved parents, sisters and my brother for their constant prayers, love, and encouragement, which have been my greatest source of strength. Without forgetting my lovely nieces and nephews.

Finally, I owe my deepest appreciation to my husband, for his endless patience, support, and understanding. His unwavering belief in me has been a cornerstone of this accomplishment.

OUTLINE

LIST OF ABBREVIATIONS

AAE	Adversarial Autoencoder
ADAPT	Adaptive Directional Antenna Protocol for Terahertz frequencies
AP	Access Point
ATR	Accuracy-to-Time Ratio
BiLSTM	Bi-Directional Long-Short Term Memory
B5G	Beyond 5th Generation
CTA	Call To Action
CTMC	Continuous-Time Markov Chain
CTS	Clear-To-Send
DBScan	Density-Based Spatial clustering of applications with noise
DCGAN	Deep Convolutional Generative Adversarial Networks
DTW	Dynamic Time Warping
DQN	Deep Q-Networks
EEMD	Ensemble Empirical Mode Decomposition
EMD	Empirical Mode Decomposition
FFT	Fast Fourier Transform
FID	Fréchet Inception Distance
GAN	Generative Adversarial Networks
GRU	Gated Recurrent Units
HHT	Hilbert Huang Transform
IMF	Intrinsic Mode Functions
KPI	Key Performance Indicators
LSGAN	Least Squares Generative Adversarial Networks

LSTM	Long-Short Term Memory
MAC	Medium Access Control
MARL	Multi-Agent Reinforcement Learning
MHS	Marginal Hilbert Transform
ML	Machine Learning
MT	Mobile Terminal
OPTICS	Ordering Points To Identify the Clustering Structure
PSNR	Peak Signal-to-Noise Ratio
RL	Reinforcement Learning
RMSE	Root Mean Square Error
RQS	Retrial Queueing Systems
RTS	Request-To-Send
SVD	Singular Value Decomposition
TL	Transfer Learning
VMD	Variational Mode Decomposition
WATR	Weighted Accuracy-to-Time Ratio
WGAN	Wasserstein Generative Adversarial Networks
6G	6^{Th} Generation of wireless communication systems

LIST OF FIGURES

LIST OF TABLES

CHAPTER I

INTRODUCTION

I.1. Overview

Wireless communication systems have witnessed continuous evolution over the past decades. With each generation bringing new capabilities are achieved which reshape how society interacts, accesses information, and manages systems. As the world waits for the sixth generation (6G) networks around 2030, the scientists and researchers' expectations go beyond merely enhancing the performance of the fifth generation (5G). The upcoming generation is envisioned as a paradigm shift that brings high-speed internet connection with 1 Tbps speed, integrate ultra-high data rates, near-zero latency, massive device connectivity, and pervasive intelligence. These advancements open opportunities for new applications that require high precision and minimal latency to emerge, like holographic communications, extended reality, digital twin, autonomous systems, and large-scale Internet of Things (IoT) ecosystems.

In parallel with this transformation lies a convergence of several enablers. Integrating new technologies contributes to achieving the 6G networks requirements. Therefore, operating on the terahertz [THz] frequencies is considered as the key enabler for upcoming wireless networks. Performing on the THz frequencies addresses the unprecedented demand for bandwidth, allowing for ultra-fast and high-capacity links. Moreover, intelligent reflecting surfaces, integrating sensing communication, and AI-native network design effectively contributes to making the radio environment dynamically controllable and context-aware. Additionally, using advanced antenna systems would offer precise spatial targeting and improved spectral efficiency, such as directional and holographic Multi-Input Multi-Output (MIMO) antennas. These elements collectively define the 6G architecture of future implementations that must be adaptive, intelligent, and capable of operating under highly dynamic and dense conditions.

6G wireless communication networks vision remains largely conceptual at this stage, as no standardized implementation or operational networks yet exist. Consequently, researchers face difficulties in studying the behavior of these emerging technologies and their feasibility in realistic environments. Studying simulation

datasets becomes essential in the absence of real-world data and deployments. However, through high-fidelity simulations, it is possible to examine how different protocols and network components might behave under different conditions. Hence, simulation environments allow us to extract meaningful performance indicators such as energy consumption, latency, collisions, and throughput. To contribute to this early exploration phase, my dissertation explores a simulation-driven framework focused on two interconnected aspects of 6G networks: **i) First** is a directional antenna-based Medium Access Control (MAC) mechanism scenario operating in the THz band, which is examined under varying network conditions to extract relevant performance metrics. **ii) The second** involves a simplified queueing system with a retrial mechanism. This model is modeled under 6G traffic assumptions to study how users interact with limited access opportunities and how intelligent decision-making can improve system performance. Together, these two components allow us to observe and analyze 6G network dynamics from both infrastructure and user perspectives, providing a solid foundation for subsequent signal processing and AI-based modeling efforts.

I.2. Problem Statement and Research Objectives

While 6G is expected to deliver all the benefits mentioned, these promises remain largely theoretical. Without operational environments or large-scale testbed experiments, researchers and scientists are forced to rely on simulation and synthetic modeling to investigate the expected behavior of both the system and proposed solutions. Among the key areas of concern is the performance and adaptability of applying a new MAC mechanism designed specifically for THz bands and directional antenna systems. The newly designed MAC protocol must navigate a unique set of constraints, including many aspects such as: high susceptibility to blockage, the need for precise alignment between transmitters and receivers, and fast signal attenuation. Meanwhile, access strategies must be efficient enough to serve a massive number of users with fluctuating demands, often competing for limited opportunities to transmit. Understanding how the designed MAC protocol might behave under various conditions, and identifying the trade-offs that it could impose on the Key Performance

Indicators (KPIs) such as throughput, delay, and collision rates, is crucial for guiding future protocol design.

In parallel, the complexity of user access in a dense 6G environment also requires innovative modeling approaches. The traditional queueing models are not enough cause they fall short of capturing the dynamic retry behavior; however, integrating adaptive decision-making enhances future networks. There is a growing need to model access not just as a static allocation problem, but as a learning process in which both the system and the users adapt over time. However, building such models is not straightforward, especially when relying on simulated data and when the system must be abstracted to a manageable level for analysis.

My dissertation addresses the mentioned challenges by proposing a well-structured methodology that connects system-level simulation, signal processing, and AI-based modeling to investigate the overall system performance, extract behavioral patterns, and learn optimal strategies. The main problem lies in identifying the right set of performance indicators, designing methods to analyze their underlying complexity, and integrating AI in a meaningful and justifiable particularly in an environment where validation with real data is not yet possible. By simulating both a directional MAC protocol and a simplified queueing system with retry behavior, this work aims to provide early insights into the types of dynamics that shapes 6G communication and access, and to explore how AI can be used not merely to react to such dynamics, but to actively learn from and optimize them.

My dissertation pursues the following research objectives:

i. **To study and evaluate** a simulation-driven framework for the upcoming wireless network system, with particular emphasis on MAC mechanisms performing on the THz band using directional antenna configurations.
ii. **To analyze** the performance of the MAC protocol under diverse network conditions and evaluate the behavior of the system's KPIs such as throughput, collision rate, and energy consumption.
iii. **To extract and cluster** complexity patterns from simulation datasets using different mathematical tools and signal processing methods such as Shannon entropy, empirical mode decomposition, and Hilbert transform.

iv. **To integrate** multiple artificial techniques into the 6G MAC analysis pipeline. The objective is to enable a predictive modeling for the system and dynamic decision-making based on the system conditions.

v. **To develop** a simplified smart 6G retrial queueing model for capturing user access dynamics and improving the system performance using intelligent strategies.

vi. **To provide early insights** for the 6G research using simulations, bridging system-level examination with AI optimization tools in the absence of real-world 6G deployments.

I.3. Research Structure

This dissertation is structured in a certain paradigm to provide a progressive exploration of 6G system modeling, starting with reviewing the existing literature works, introducing the used methodology, exploring the used simulator, and explaining data extraction, how it was the advancement throughout the simulation, data analysis, and intelligent decision-making. Each presented chapter is built based on the previous one, producing a coherent methodological framework that responds to the early-stage challenges of 6G network research.

Chapter II reviews the existing literature across three main domains: 6G communication technologies, data analysis methods, and the integration of artificial intelligence into communication system modeling. The goal of this section is to situate the proposed approach within current research efforts, identify gaps in simulation-based evaluation of MAC protocols and access mechanisms, and highlight the role of AI in making sense of complex network behavior. Chapter III presents the overarching research methodology, which consists of four complementary main methods. The first method presented focuses on conceptual system design for 6G network modeling, , the second method addresses feature extraction and complexity analysis using traditional signal processing techniques, the third method shifts toward intelligent learning, proposing AI strategies including unsupervised learning, supervised learning with wavelet transforms, transfer learning, generative modeling, and reinforcement learning as tools for extracting knowledge and optimizing behavior from simulated

data, and the fourth method focuses on evaluation and theoretical validation in the absence of real-world 6G data, relying on system decomposition, entropy-based analysis, and synthetic benchmarking.

Chapter IV explains in detail the simulation-based data extraction process. It describes the implementation of the MAC protocol within the ns-3 simulator, the setup of network topologies and scenarios, and the collection of raw data representing the system's behavior under varying 6G-relevant conditions. Additionally, Chapter V applies the signal processing techniques to analyze the extracted data. Through approaches such as Shannon entropy, Empirical Mode Decomposition (EMD), ensemble EMD (EEMD), and Marginal Hilbert Spectrum (MHS). The chapter reveals the underlying complexity and trends of the 6G KPIs. This analysis serves both as a tool for understanding system behavior and as a foundation for feeding refined features into AI models.

Chapter VI focuses on integrating the AI methods, where different learning paradigms are used to model, predict, and optimize the 6G system behavior. Each AI approach is selected based on its suitability to the problem structure: clustering, classification, pattern generalization, or strategic learning. Special emphasis is given to reinforcement learning, which is applied in the context of a modeled retrial queueing system to learn dynamic access policies. Finally, Chapter VII concludes the dissertation by summarizing the main findings, reflecting on the implications of simulation-based research in the early 6G era, and proposing directions for future work. These include the eventual validation of the proposed models with real-world 6G deployments and exploring the scalability of AI integration within operational systems.

CHAPTER II

RELATED WORK

We organize the related work into distinct sections. This approach allows us to systematically explore the relevant literature, ensuring that we adequately cover the various aspects of the topic. By segmenting the related work into three main parts, we aim to provide a clearer understanding of how each part contributes to the overall framework of the presented research.

II.1. Current Landscape of 6G Network Research

In the field of high-speed wireless networks, a lot of research work has been done for investigation and development purposes. This section gives a brief overview of the most relevant studies, highlighting their contributions and the objectives of this research.

Medium Access Control Mechanism for 6G networks

Developing the next generation of wireless communication requires several efforts due to the new frequency band that operates on, therefore researchers in [1] propose to use a new IP architecture having new Quality of Service (QoS) aspects, integrating Machine Learning (ML) along with 6G technology enhance the service efficiency and help to meet its requirements [2]. In addition, the authors in [3] propose to use a receiver-initiated handshake for ensuring the synchronization in the THz communication channel, however moving to new frequencies causes new challenges, therefore, a transceiver architecture having ultra-broadband and multi-band was suggested to overcome the objections, while in [4] a wireless link called Single Input Single Output (SISO) is proposed to reach 100 Gbit/s data rate. The growth of internet use and technology requires network infrastructure, based on the QoS of the 5G networks, an enhanced cat swarm optimization (ECSO) was proposed for optimization purposes [5]. The applied method increases the throughput by 8% and shortens response time by 7% compared to the existing algorithms. This study would underscore the importance of maintaining user experience in dense and high-demand settings in the 6G wireless communication network.

The importance of developing terahertz communication lies in its potential to achieve data rates over 100 Gbps and latency under 1 millisecond for 6G systems [6].

This technology supports applications such as Tera-WIFI and THz wireless backhaul, and advancement in THz technologies is pivotal in bridging the THz GAP, positioning terahertz communication as a foundational element of future wireless systems. Nevertheless, developing a suitable MAC protocol for terahertz communication is essential to address challenges such as high path loss and scattering, which restrict communication distances [7]. As a solution for the bandwidth demands of the 6G technology, it introduced full-spectrum wireless communication (FSWC) [8], which utilizes the entire electromagnetic spectrum, from microwaves to ultraviolet light, addressing the spectrum shortage and enabling a new communication paradigm.

Queueing theory in the next-generation networks

Queueing systems have been a hot research topic among researchers for a long time, and this is because of their vast applicability fields, particularly in networking and wireless communications, where efficient allocation and congestion control mechanisms are essential. There are many research works that leverage queueing theory to analyze network performance, enhance quality of service, and optimize scheduling policies. A recent study has introduced a queueing theory-based framework for modeling fog computing systems, which helps to optimize the resource allocation to meet the QoS requirements [9]. This model helps to identify the bottlenecks and improve the system performance by allowing user-defined parameter adjustments. In the same field, a research group proposed another task allocation method to minimize the latency in Mobile Edge Computing (MEC) for future internet applications with dedicated, shared, and cloud servers [10]. They used queueing theory to model transmission delay and solve an optimization problem, where results show an efficient allocation of tasks and a reduction in the overall delay. However, another study has been made to explore cybertwin-based multiaccess edge computing as an alternative to the traditional Virtual Machine (VM) systems, where they show its benefits in cooperating through a control plane, and the results promise future solutions for the upcoming wireless communication network beyond 5G [11].

A comprehensive survey on network delay was conducted in [12] with a focus on a special key performance indicator of the queueing model which is the delay and its

impact on communication performance, they examined the delay effect in different networks including wireless, mobile and IoT and others, offering insights into delay management strategies. Moreover, other research groups have analyzed the performance of different queueing mechanisms in managing network traffic over Wi-Fi. Results highlight the good performance of the weighted fair queueing (WFQ) in allocating bandwidth and reducing packet variation [13]. QoS challenges were explored in [14] in the next generation wireless sensor networks (WSNs) and the 5th generation, the research group proposes a dynamic queueing mechanism for prioritizing traffic based on data type and queue length, and other KPIs aspects, the findings show the improvements of the QoS efficiency for real-time communication in limited bandwidth networks. Nevertheless, queueing models for cognitive radio networks were examined by focusing on the sensing time of secondary users and their access to idle channels that are originally allocated to primary users [15]. It was found that both models share the same stability condition, with a non-interrupting model having fewer sensing secondary users.

For congestion control in network systems, a new scheme was introduced, called a self-adaptive random early detection (SARED), that dynamically adjusts its drop pattern based on the current traffic load, and this comes to overcome the limitation of traditional active queue management (AQM) [16]. A different study was conducted to investigate the age of information (AoI) and peak AoI (PAoI) metrics in the multisource IoT systems [17], which analyzes three queueing disciplines for the status update process. Meanwhile, queueing network-based approaches were presented to analyze the consistency of consortium blockchain protocols and their performance [18].

The research papers mentioned above highlighted the critical role of queueing systems with different models and motivated us to explore a more refined approach for adapting it to our system.

II.2 Data Analysis Methods

This section provides some related research work that used similar data processing methods and gave a considerable result.

Shannon Entropy in Wireless Networks

The application of Shannon entropy in wireless communication and sensor networks has emerged as a crucial field, being a crucial decision metric, reducing energy consumption [19]. The idea of enhancing the corona IPv6 routing protocol for low-power and lossy networks (CoRPL) [20] routing protocol by integrating the mobility entropy helps in reducing the packet loss and optimizing the used power, meanwhile, the entropy was used for the same purpose in [21, 22]. In the IoT domain, Shannon entropy plays an important role in enhancing the feature selection for wireless signal processing and for small electronics [23] and helps in increasing the significance of harnessing energy from environmental sources [24]. Shannon entropy was used for other aims in wireless communication technologies and meshed with some applications due to its capability in the information theory field, showing its strength in optimizing data transmission, encoding, and compression techniques [25, 26, 27]. Moreover, research was made to explore the transport capacity of multi-node wireless networks through information theory, considering how distance and signal attenuation impact information transfer [28]. Information-theoretic principles reveal that cooperation between nodes and multiuser estimation can significantly improve capacity under favorable conditions.

Topological entropy was used to analyze wireless networks affected by scattering and shadowing [29]. New entropy bounds are derived based on fading distributions, showing that different models lead to distinct network entropies. These recent research papers demonstrate how important is using Shannon entropy in network uncertainty quantification, traffic prediction, and anomaly detection in wireless networks and IoT fields.

Empirical Mode Decomposition, Ensemble Empirical Mode Decomposition, and Marginal Hilbert Transform for Non-Stationary Signals

EMD and EEMD are two signal processing methods used to decompose non-stationary and nonlinear signals into Intrinsic Mode Functions (IMFs). They are mainly applied in the telecommunications field for wireless interference cancelation, channel estimation, and anomaly detection. The authors in [30] aim to compare those

two methods in the analysis of a seismic signal. The results of this work show that the time-frequency spectrum obtained through EEMD more accurately reflects real geological conditions as compared to EMD. Other work has been done on the same topic using EMD, EEMD, and Variational Mode Decomposition (VMD) in [31] for chatter detection in milling. The researchers compared the three methods and found that EEMD and VMD were more effective than EMD. EMD has been widely used for trend extraction in various fields, It is a powerful tool for analyzing non-stationary signals and extracting meaningful information from them. However, trend extraction methods using the IMFs might differ.

In [32], the authors decompose the IMFs into two parts, and the trend is one of them. Moreover, in [33], the authors proposed a method for extracting the trend. The method involves decomposing the signal into IMFs and then fitting the extracted trend component using the least squares method. The proposed method was validated using experimental data and was found to be effective in identifying the trend of the cement-burning zone flame temperature. Research conducted in [34] compared EMD and EEMD and revealed that EMD suffers from mode mixing, leading to inaccurate extraction of signal characteristics. On the other hand, EEMD successfully extracts meaningful components and exhibits superior performance in fault diagnosis for rotating machinery, as demonstrated through simulations and real-world applications. In a related study, another group of researchers investigated EEMD's effectiveness in overcoming mode mixing by introducing white noise [35]. EEMD accurately decomposed signals into distinct IMFs, thereby enhancing time-frequency analysis and providing more realistic time-frequency spectra in geology applications.

The team in [36] introduced a hybrid denoising method that combines threshold IMFs with data-driven VMD, proving highly suitable for non-stationary seismic signals with reduced noise sensitivity. Additionally, [37] demonstrated that EEMD outperforms EMD and VMD for calculating respiration rates from PPG signals, achieving over 90% accuracy with an average error rate of 1 rate/minute. EEMD shows potential in simplifying sensor devices for accurate RR calculation.

As a related research paper, impulsive interference bursts were addressed in wireless communication, which degrades system performance. However, by using

EMD, it adaptively decomposes and filters noisy signals, demonstrating significant signal recovery [38]. EMD was also used for enhancing anomaly detection in multipath TCP networks [39]. Moving to the Hilbert Huang Transform (HHT), a research group that focuses on predicting epileptic seizures using EEG signals by analyzing their low-pass spectral attributes in the Hilbert domain [40], which achieved high prediction accuracy with low false alarm rates. HHT was used as well in other research [41] to develop an asynchronous demodulation method for single sideband (SSB) signals in mobile radio paths. Furthermore, in 42] other signal processing methods besides the HHT were explored, like wavelet decomposition and Fast Fourier Transform (FFT), to improve signal detection and tracking.

The use of HHT and EEMD helped extract satellite signal fingerprint features in complex maritime communication environments [43]. And helped in overcoming the limitations of predefined frequency bands by adapting to subject-specific brain oscillations in EEG analysis [44]. Nevertheless, the researcher in [45] used HHT to develop a full-spectrum periodic nonlinear Fourier transform-based communication system. HHT also benefits in diagnosing bearing fault modes by extracting features from the Marginal Hilbert Spectrum, which are then used in machine learning algorithms. The results show a high classification accuracy of 93.8% [46]. A three-dimensional entropy-based complexity evaluation method was developed in [47] to extract fault features in rolling bearings by analyzing time, amplitude-modulated, and frequency-modulated information. Despite these advances, few studies have applied these methods directly to 6G system-level simulations, where new technologies and frequencies are used. This gap motivates the present research.

II.3. Artificial Intelligence Applications in 6G Networks

Transfer Learning (TL) ML is considered a powerful tool enabling models to leverage knowledge from related tasks or domains to improve performance on a target task. Multi-layer TL allows more sophisticated knowledge to transfer across multiple layers of the neural networks. As said, a Long-Short Term Memory (LSTM) multilayer RNN was implemented to achieve high accuracy [48, 49] with different prediction models. To reduce the computational complexity and minimize the training

overhead that most of the ML suffers from, the researchers in [50] present an enhanced algorithm, learned-sparse Bayesian learning with generalized approximate message passing (L-SBL-GAMP) for designing hybrid precoders and combiners in mmWave massive MIMO systems. The simulation achieves a higher rate and improved accuracy in large-scale MIMO systems.

For achieving high accuracy, the researchers in [51,52,53] highly recommend using a pre-trained model for transfer learning, besides pre-processing using augmentation and segmentation in addition to a hybrid convolutional network. Recurrent NN exhibits excellent performance by using Bi-Directional Long-Short Term Memory (BiLSTM) [54]. This high level of accuracy proves the effectiveness of the used model in capturing forward and backward dependencies in sequential data. Artificial Neural Network (ANN) was used on real-world data collected through dive tests in [55], which examines the relationship between QoS parameters and user satisfaction for various multimedia services. The ANN model simulates the user experience, producing a quality of experience (QoE) score that informs network optimization, offering a practical framework for mobile network operators to improve service quality aligned with user satisfaction. The ANN was also used in another study [56] to estimate QoE scores from QoS metrics, enabling a self-tuning approach in long-term evolution (LTE) networks for optimizing resource block allocation. With a particle genetic efficiency algorithm (PGA) to adjust service priorities, this method improves user satisfaction and resource efficiency.

The authors in [57] propose a metric for evaluating the performance of a deep learning method known as DAWNBENCH using Time-To-Accuracy (TTA). This metric is designed to compare different DL techniques by measuring the learning time for reaching a specified accuracy level. Meanwhile, another research group [58] presents a framework for uncertainty quantification (UQ) in NNs validated through comparative studies on prototype problems. An open-source Python NeuralUQ is developed to facilitate UQ implementation in scientific machine learning, along with tutorials and computational experiments. In the field of DL, research was done [59] to explore its role in managing vast data generated by the IoT. With billions of devices

capturing diverse data, DL techniques enable anomaly detection, trend forecasting, and control for secure, efficient IoT operations.

For such a dynamic and complex environment comes the role of the powerful reinforcement learning AI method that optimizes decision-making, including wireless networks and queueing systems. Many existing research studies have proved the ability of Reinforcement Learning (RL) to enhance traffic management, resource allocation, and optimize network control policies, as was done in [60] for queueing networks, focusing on minimizing job delay and queue backlog. The simulations demonstrate their effectiveness in dynamic server allocation as well as the routing and switching scenarios. Similarly, RL has been used the RL for service-rate control in tandem queueing systems, making sure that the resources are managed efficiently while the end-to-end delay is guaranteed [61]. Advanced policy gradient methods like proximal policy optimization have improved queuing network control [62], which supports the work in adaptive queue management for 6G systems.

Furthermore, a combination of graph neural networks and deep RL helps in optimizing network automation and resource management [63], which supports intelligent control for the upcoming generation of networks. Another work [64] proposes a deep RL-based active queue management scheme for managing traffic in IoT networks using fog/edge architecture. The results show that it outperforms other active queue management schemes in terms of KPIs, demonstrating its efficiency in congestion management. Generative diffusion models (GSMs) are considered a powerful tool for network optimization when combined with deep RL, where the researcher in [65] highlights their application in various network domains. Additionally, [66] examined the use of learning techniques in optimizing queueing systems, discussing the connections between queueing theory and adversarial learning. Moreover, the researchers highlight the importance of service parameter estimation, decision estimation, and recent advances in RL. From the related research papers mentioned and even from others, we saw the effectiveness of RL and deep learning in optimizing network control and queueing management.

Most existing research papers evaluate AI models in the current wireless technology (5G) or IoT context. The extension to 6G data analysis remains underexplored, particularly using simulated datasets at THz frequencies and with directional antennas. This gap motivated us to integrate AI tools into the 6G environment for optimizations and classifications.

II.4. State of the Art in 6G Network Data Analysis

Based on the reviewed methodology above, it is evident that while Shannon entropy measures, signal decomposition, and AI techniques has been successfully applied in the telecommunication domains, their applications in the specific context of 6G and THz network data analysis remain uncovered. State-of-the-art efforts in this direction are still emerging. We could see that a unified framework that bridges simulation-driven data extraction, complexity analysis, and AI integration for 6G networks has not yet been developed. This dissertation contributes to this state of the art by:

i. Analyzing an existing MAC protocol designed for communicating in the THz frequencies.
ii. Extending complexity analysis methods (like Shannon entropy, and EMD) to 6G KPI datasets extracted from system-level simulations.
iii. Integrating AI methods (like transfer learning and generative AI) to optimize MAC mechanism and retrial queueing in 6G environment.
iv. Demonstrating how data analysis methods can give a meaningful insight into the performance trade-offs and dynamics behaviors for the future 6G applications.

CHAPTER III

RESEARCH METHODOLOGY

This chapter outlines the conceptual structure and foundation upon which the rest of the dissertation is built. The methodology followed is a sequence of integrated stages designed to enable a systematic understanding of 6G behavior through simulation, data processing, and AI-based modeling. Since the real-world 6G data are not available yet, the methodology emphasizes theoretical modeling, simulation-driven data extraction, and rigorous validation using state-of-the-art analytical and learning techniques. At its core, the methodology strategy answers the following research question: *"How can we simulate, analyze, and learn from 6G network behavior in the absence of real-world datasets, using abstract modeling, signal processing, and intelligent interference systems?".* The process is organized into four main conceptual stages, as shown in Figure III-1.

i. **KPI selection:** Such as throughput, delay, and collisions are identified as the primary metrics representing the system's dynamics. These are used as both observational variables and learning targets in later stages.
ii. **Processing tools and signal-based analysis:** Traditional mathematical processing tools are applied to extract meaningful features and quantify behavioral complexity from the raw simulation datasets.
iii. **AI integration strategy:** Depending on the type of extracted features and the modeling objective, different AI techniques are employed. This includes unsupervised learning for pattern discovery, supervised learning with wavelet-enhanced features for prediction tasks, multi-layer transfer learning, generative AI for data synthesis, and reinforcement learning for decision-making optimization.
iv. **AI output and interpretation:** The output of the AI models are diverse and context dependent. It could include clusters, classes, synthetic data or learned policies for optimization purposes.

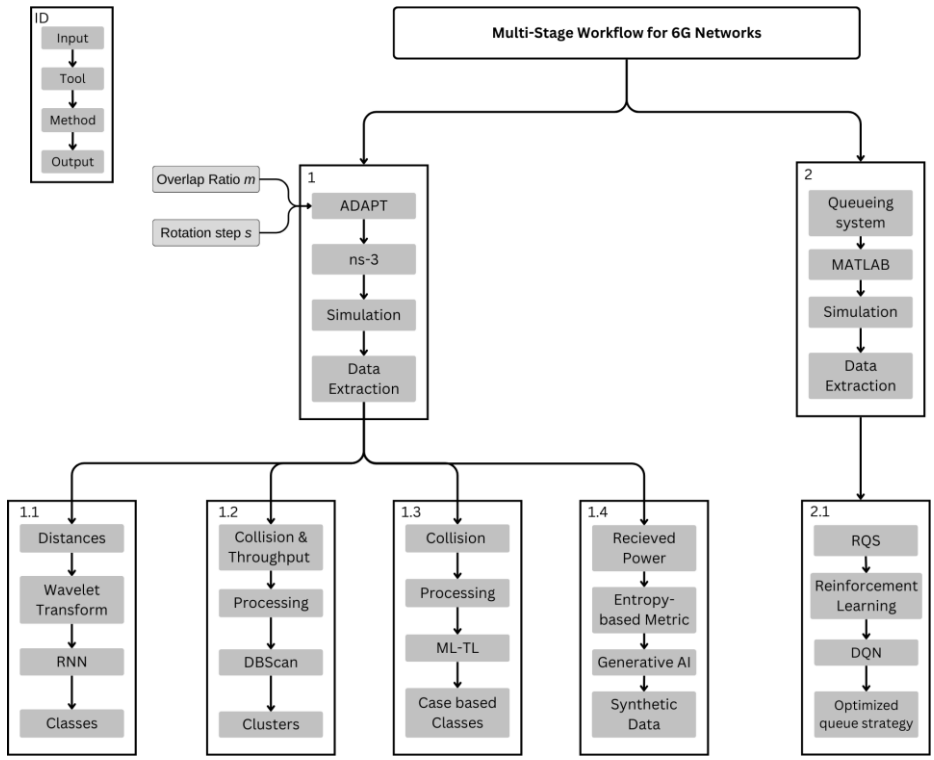

Figure III-1 Overview of the dissertation methodology.

Two modeling components are considered: the ADAPT MAC mechanism for directional 6G communication (block 1) and the RQS model for user access control (block 2). Each component feeds its simulation outputs into a unified processing and learning pipeline that includes processing tools, AI integration methods, and result interpretation.

Each of the following 4 methods represents a key component of this pipeline, beginning with the simulation environment used for the simulated data and ending with the validation techniques used to assess the reliability of the AI outputs in the absence of the empirical ground truth.

III.1. Conceptual System Design for 6G Network Modeling

Our research work strongly lies in the conceptual modeling of the upcoming generation wireless communication system aligned with the expected characteristics of 6G. We ensured that we investigate an environment that is designed to capture the behavior under 6G conditions, therefore, we chose to study a medium access control mechanism that operates under terahertz frequency bands, with an emphasis on

directional antenna communication. This setup aims to reflect the increasing importance of high-frequency, high-capacity, and low-latency communication paradigms expected in future wireless systems. Moreover, we chose to design a simple example for a queueing system under 6G conditions to investigate the fundamental behaviors and performance limitations. By reducing the complexity at the system level, we more clearly interpret and observe the impact of certain factors that are expected to play a critical role in the performance of future 6G architectures. Rather than delve into the technical implementation, we focus more in this part to underline the logic behind the methodology used, while the rest is explained in details in the next chapters.

The main goal of this method is to establish the framework for extracting high-fidelity performance metrics from a simulated 6G communication environment. Our focus was on the value and the role of the extracted key performance indicators in understanding and enhancing the next-generation wireless dynamics. The extracted analytical datasets; specifically the KPIs such as throughput, delay, packet drop rate, access collisions, and received power, serves as behavioral signatures of the network's performance under a realistic conditions and are analyzed and used extensively throughout the dissertation to: characterize directional MAC dynamics under terahertz frequencies, quantify queueing behavior and access information, and help in understanding more the system for future enhancement.

The Extracted KPIs serve to enhance and use multiple strategic roles across the research.

i. Throughput and delay: these indicators allow us to study communication efficiency and access scheduling over time. Throughput is computed as the following:

$$T = \frac{\sum_{i=1}^{N} S_i}{\Delta t} \quad (1)$$

Where S_i is the successfully received packets size (bits) during interval Δt. In the meanwhile, average delay is determined as the following:

$$D = \frac{1}{N}\sum_{i=1}^{N}(t_i^{recv} - t_i^{sent}) \quad (2)$$

Where t_i^{recv} and t_i^{sent} denote reception and transmission times of packet i.

ii. Collision: The temporal overlap and scheduling gaps can cause packet collisions or drops; however, monitoring these criteria helps in modeling reliability and fairness.

$$C = \begin{cases} 1, & packet\ i\ collides, \\ 0, & otherwise. \end{cases} \quad (3)$$

iii. Received power: We think that it is essential for understanding how spatial distribution and THz signal behavior impact communication quality; therefore, this metric is valuable for Shannon entropy analysis. Received power is determined using the following formula:

$$P_r(d) = P_t G_t G_r (\frac{\lambda}{4\pi d})^2 \quad (4)$$

based on Friis' equation, where P_r is transmitted power, G_t and G_r are antenna gains, λ is wavelength, and d is distance.

iv. Queue length and retry statistics: It provides insight into system saturation, congestion control, and user experience under different network conditions.

$$Q(t) = number\ of\ packets\ in\ buffer\ at\ time\ t \quad (5)$$

Meanwhile, the strength of these KPIs is a dynamic data series that evolves with time and context, this needs a suitable processing technique for a good interpretation. The selected KPIs are chosen not just for performance evaluation but for their analytical richness, supporting both signal-theoretic decomposition and AI-based modeling, which are applied in the subsequent chapters.

III.2. Feature Extraction and Complexity Analysis

To derive a meaningful insight from the extracted network data, we chose to use traditional processing techniques that transform the signal into structured representations suitable for further processing. We believe that using such techniques serves as a bridge between the simulation-extracted data and the advanced AI integration approaches. Traditional signal processing and statistical decomposition techniques tend to identify key patterns, remove noise, and extract informative features that describe the network's behavior over time and provide a more refined understanding of the upcoming wireless communication generation.

Feature extraction techniques are needed to make the extracted KPI signals more interpretable and useful for further analysis. These techniques can be: **i. Time-Domain**

Features: like mean, variance, and autocorrelation analysis techniques. **ii. Frequency-Domain Transform:** Like Fast Fourier Transform to analyze frequency components of network dynamics, or like wavelet transform for time-frequency analysis, this end is useful for capturing transient events. **iii. Statistical complexity measures:** like Shannon entropy for quantifying the unpredictability of system states, or fractal dimension analysis that helps characterize the self-similarity over different time scales. Beyond feature extraction, we conduct complexity analysis to understand the inherent structure and predictability of network performance variations, this includes: **i. Empirical mode decomposition and ensembled emperical mode decomposition:** this decomposition technique is often applied on non-stationary signals for decomposing it into intrinsic mode functions that isolate different timescale behaviors. The aim is to help distinguishing between short-term spikes and long-term trends. **ii. Marginal Hilbert spectrum analysis:** It is an energy-based representation of decomposed signals, revealing how communication performance evolves and frequency. **iii. Correlation and mutual information analysis,** which helps to uncover relationships between different system parameters.

Applying AI method directly on unprocessed data set can be inefficient, instead, applying traditional processing techniques before AI integration can help in many factors: reducing data dimensionality while preserving key information, isolating meaningful patterns and trends in network behavior, providing interpretable insights into system stability and dynamics, and enhancing the performance of machine learning models by supplying well-structured input features.

III.3. AI Strategy for Learning from Network Data

As the next-generation wireless communication networks are expected to operate under highly dynamic and context-aware conditions, the ability to intelligently learn from data becomes necessary for both performance optimization and system adaptation. For such complex systems, traditional rule-based systems often fail under such non-stationary and high-dimensional conditions. Artificial Intelligence, particularly data-driven learning, is well-suited to capture nonlinear relationships among variables like delay, throughput, and node distributions. Also suited to predict

network behavior under unseen conditions or topologies and generalize across similar environments without manual reconfiguration. To accommodate the varied nature of network data and problem definitions, we structured our learning strategy as follows:

i. **Pattern discovery:** clustering and unsupervised learning methods are applied to identify hidden structures in the data without labeled outputs.
ii. **Prediction of network performance: supervised learning models like recurrent neural networks combined with feature extraction methods (like wavelet transform), are deployed** for classification and predict outcomes. Transfer learning is also used to improve efficiency across related scenarios.
iii. **Data augmentation for rare events: generative AI s**ynthesizes new realistic data samples for rare-event modeling or simulating stress conditions that are not frequently observed in simulations.
iv. **Adaptive control and decision-making: Reinforcement learning is applied to derive dynamic policies for queue management,** control queuing decisions, or retry probabilities.

This method acts as the core intelligent layer in the dissertation's overall system design. It transforms complex data into adaptive control strategies and interpretable predictions, thus enabling the practical application of MAC optimization through learned policies, validating the utility of the simulation and processing layers for AI-readiness, and demonstrating how AI can be systematically embedded into early 6G system design.

III.4. Evaluation Strategy and Theoretical Validation

Since 6G network development is still in the early stages of development, the real-world deployment and data availability are limited, and the evaluation of AI-driven models and simulation-based mechanisms must rely on theoretical validation, simulation experiments, and comparative behavioral analysis rather than direct benchmarking with real-world data. We chose in this research to focus on the evaluation strategy adopted to ensure that the proposed approaches are logically consistent, credible, and grounded in sound performance metrics. Therefore, the

strategy is built upon KPIs expected in 6G networks, which serve as ground-truth metrics for AI models to predict, optimize, or explain.

To ensure trustworthiness, every AI component integrated into the modeling is validated against known behavioral baselines, such as random decision-making or fixed heuristic control (e.g., fixed retry probabilities). Moreover, we ensure that the modeling component is integrated and assessed under varying network densities, antenna configurations, and traffic conditions to validate generalization. No one can deny that the real-world datasets are ideal, however, since it does not exist yet, our research relies on strong approaches to strengthen the credibility of simulated data: **i. Physics-based simulation modeling (via ns-3 simulator):** where the data reflect realistic physical and protocol-level constraints, including directional propagation, THz band behavior, and adaptive MAC scheduling. **ii. Entropy-based complexity analysis:** This offers a rigorous, system-theoretic lens to assess whether simulated data captures meaningful randomness and structure like real-world systems. **iii. Generative models** are again evaluated for their ability to produce data distributions that mimic the observed simulation outputs and further reinforce the plausibility of the generated samples.

The dissertation emphasizes that the entire modeling and learning pipeline is designed to be data-compatible because we believe that once measurement campaigns or prototype 6G testbeds emerge, real data can seamlessly replace or complement the synthetic datasets. Nevertheless, the proposed architecture can serve as a reference framework for future experimental validation or testbed integration.

CHAPTER IV

6G MAC: DATA EXTRACTION

A detailed examination is presented in this chapter, outlining its key characteristics, source, and significance to the research. Moreover, the data extraction process is emphasized, with a focus on the measures taken to ensure data accuracy, reliability, and integrity. Next, a comprehensive analysis of the MAC evolving demands of the next-generation communication technologies.

IV.1. Ns-3 TeraSim Extension

For extracting the data, we used ns-3 to simulate the example 'macroscale scenario' provided in the TeraSim tool 67] version two. TeraSim is an ns-3 extension designed to model wireless communication in the THz frequency band. As the authors mentioned in [68], the unique properties of the THz band provide an enormous bandwidth ranging from tens of GHz to a few THz, which inspired them in the design. Besides its advantages, communication can be affected by spreading loss and molecular absorption, However, these effects become more pronounced over longer distances.

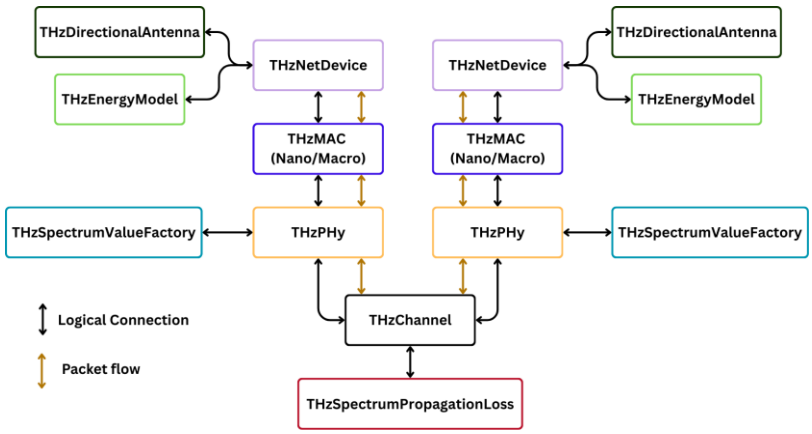

Figure IV-1TeraSim extension architecture including the integrated models.

Therefore, TeraSim provides two main examples: **i) The nanoscale scenario** covers shorter distances (under one meter), and the THz band can be treated as a single, wide transmission window (around 10 THz in width). **ii) Macroscale scenario:** mainly used for longer distances, and the THz band splits into multiple and narrower

transmission windows, each ten GHz wide, due to the molecular absorption. Also, to overcome the high path loss, this scenario uses directional or beamforming antennas, while energy harvesting is typically not necessary due to the larger power budget.

Both Nanoscale and Macroscale used a unified and modular architecture as shown in Figure IV-1. The THzNetDevice in TeraSim serves as the core component of each node, functioning as the Network Interface Card (NIC) to handle both the Physical (PHY) and MAC layers. The THzPhy uses the THzSpectrumValueFactory to generate pulses for nanoscale communication and continuous carrier waveforms for macroscale scenarios. Communication between nodes is done through the THzChannel that uses the THzSpectrumPropagationLoss to calculate the effect of spreading loss and absorption on different frequency bands. For the nanoscale scenarios, energy efficiency is critical. Therefore, the THzEnergyModel is integrated into each node to help nanodevices maintain long-term functionality. The THzNetDevice also manages the antenna system; for nanoscale applications, it operates omnidirectionally, while for macroscale applications, it switches to highly directional or beamforming antennas to overcome the increased path loss. TeraSim implements two well-known MAC protocols, ALOHA and Carrier Sense Multiple Access (CSMA), which are adapted to meet the specific needs of the physical layer of each scenario. The THzDirectionalAntenna and energy THzEnergyModel are specialized for nanoscale and macroscale communications, however, they can be adapted to work across both with minor tweaks to the MAC layer. This flexibility makes TeraSim a powerful extension for ns-3 for exploring the THz band communication networks.

IV.2. ADAPT MAC Mechanism & Scenarios

The proposed Adaptive Directional Antenna Protocol for Terahertz frequencies (ADAPT) protocol is designed to comply with IEEE 802.15.3d, the first standard for the Terahertz physical layer. ADAPT performs in a cell with a radius of tens of meters divided into equally sized sectors, as shown in the Figure. IV-2, with the Access Point (AP) in the center surrounded by the Mobile Terminals (MTs). We applied two distribution topology types: d1: centered distribution, having the MTs distributed randomly closer to the AP, and d2: uniform distribution, having the MTs distributed

randomly around the central point. The sector rotation-based retransmission mechanism of ADAPT is modeled with Poisson arrivals to reflect realistic traffic patterns.

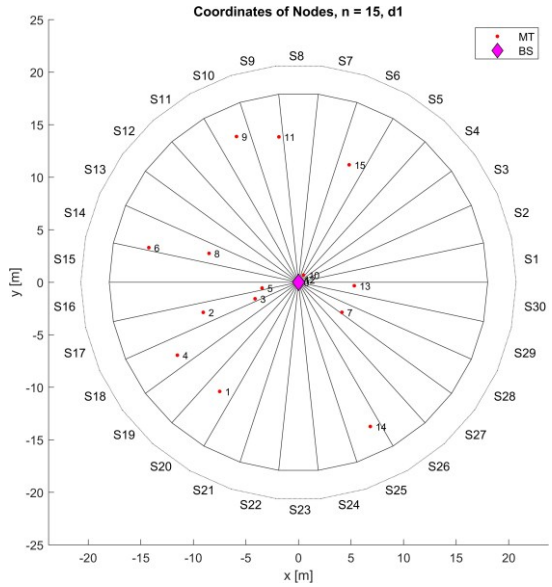

Figure IV-2 The spatial distribution of MTs (centered topology, n = 15).
AP is symbolized with a diamond in the center. There are 30 sectors around the AP, where the number of MTs per sector might be zero because of the low population density.

To manage the access control, the ADAPT protocol used the 3-way handshake to establish the connection between the AP and the MTs (see Figure. VI-3 and Figure VI-4). The AP starts to send a Call-To-Action (CTA) control frame to all MTs belonging to the current sector. The CTA frames serve as an invitation, signaling all the mobile terminals in the sector that they may prepare to communicate. By sending this frame, the AP effectively broadcasts its readiness to handle data from the MTs, encouraging those devices ready to transmit (Active MTs) to respond. The active MTs reply to CTA by sending a Request-To-Send (RTS) control frame back to the AP. The RTS frames are sent by each MT to inform the AP that they wish to start transmitting data. The exchange of CTA and RTS frames establishes a basic form of communication coordination. However, because more than one MT may respond with RTS frames at roughly the same time, the collision probability increases during this

stage. Collision probability refers to the chance that two or more MTs attempt to send their RTS frames simultaneously, causing their signals to interfere with each other.

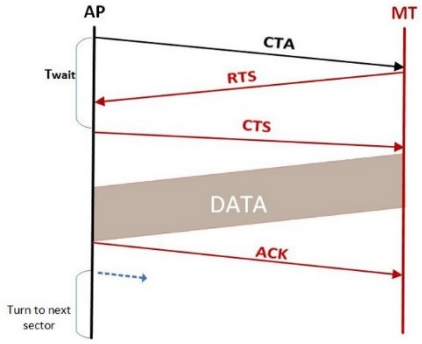

Figure IV-3 The MAC mechanism of the ADAPT protocol for one MT.

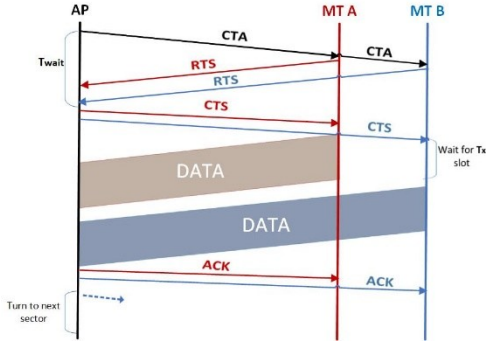

Figure IV-4 The MAC mechanism of the ADAPT protocol for more than one MT.

In each sector determined by an angle φ, specific signals are sent. CTA is launched by the AP at the beginning of the 3-way handshake protocol to call MTs to request access to the channel

After a certain time, the MTs receive a Clear-To-Send (CTS) control frame from the AP containing the exact time to send their data so they do not interfere with each other. This time slot allocation is key to avoid data collision, which occurs when multiple MTs attempt to send data simultaneously. Collision problems are common issues in wireless networks, as shared channels can become overloaded when multiple devices try to communicate at once. By using CTS frames, the network limits these collisions to the control frames stage. This way, collisions are minimized during the actual data-sending stage, where larger amounts of data are transmitted. Once all data is received from the MTs, the AP sends an Acknowledgement (ACK) frame back to each MT. The ACK serves as confirmation that the data was successfully received and processed. After the current batch of MTs has been handled, the AP shifts its focus to the next sector. The sector-based protocol is particularly useful in directional antenna systems, where the AP can focus its signals in specific directions to optimize communication with MTs in different areas. By repeating the same process in each sector, the access point can sequentially manage the MTs in various zones without overloading the communication channel, enhancing network efficiency, and reducing

wait time for each MT. Table IV-1 provides all the parameters that we used for our simulation.

Table IV-1 Parameters used by the simulation.

Parameter	Name	Parameter	Parameter Values
L	Packet size	Fixed	65,000 Bytes
$\boldsymbol{R_{Tx}}$	Transmission Rate	Fixed	69.12 Gbps
r	Cell Radius	Fixed	18 m
N	Number of Sectors	Fixed	30
$\boldsymbol{\varphi}$	Angle of the	Fixed	12°
$\boldsymbol{t_{sec}}$	Sector Time	Fixed	3,470 ns
$\boldsymbol{t_{sim}}$	Simulation Time	Fixed	10 ms
n	Number of MTs	Variable	{15, 30, 60, 120, 240, 480, 960}
d	Topology Type	Variable	{d1, d2}

The ADAPT MAC protocol enhances traditional IEEE MAC protocols by incorporating the CTA signal before RTS, which synchronizes the contention period for RTS transmission. This technique is akin to slotted ALOHA, but instead of longer data frames, ADAPT uses shorter RTS frames, reducing the likelihood of collisions. Conversely, IEEE MAC protocols without CTA frames lack this synchronization, leading to a higher probability of collisions during unsynchronized RTS transmission. ADAPT's approach enhances efficiency, especially in high-traffic conditions. By framing ADAPT alongside these baseline approaches, the categorizes it within a broader family of contention-based MAC strategies, clarifying its conceptual distinction rather than treating it in isolation.

IV.3. System Behavior, Different Aspects Analysis

As previously mentioned, the collision rate increases at the control frame stage, Figure. IV.5 and Figure. IV-6 represents the collision rate spatial distribution with the highest MT number (n = 960), using the two different topologies: centered and uniform, respectively [J2, C1]. The two figures contain the following information:

i. The diamond in the center symbolizes the AP.
ii. Black squares are the MT with no collisions.
iii. Bubbles represent the MTs experienced at least once during the control frame.

iv. Square and bubble size are proportional to the successfully transmitted data frames.

v. Grayscale shading of the bubbles indicates the collision rate value; a darker color signifies a lower collision rate.

In both figures, most small bubbles are lighter in color, indicating higher collision rates for these MTs and, correspondingly, a lower rate of successful transmission. This observation aligns with the expectation that MTs with higher collision rates tend to have reduced transmission success. Interestingly, the distribution of the collided MTs is random, having no connection with the topology type, and it is considered to be uniform in angular coordinates. This might happen because the closer MTs to the AP still belong to different sectors, causing them to collide at a similar rate as MTs in more distant regions. Moreover, the number of non-collided MTs is evenly distributed radially regardless of the topology type, which arises from the uniform angular distribution of the MTs.

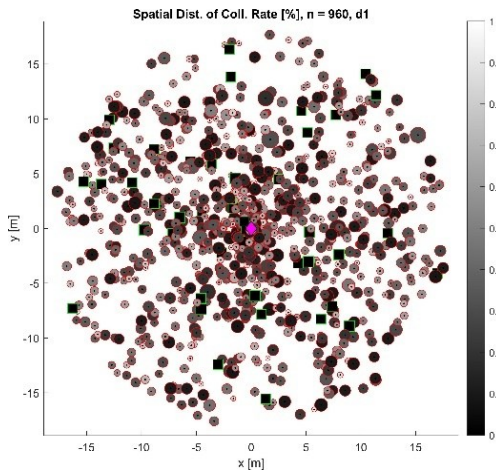

Figure IV-5 Spatial distribution of active MTs and its collision rates for centered topology (n = 960).

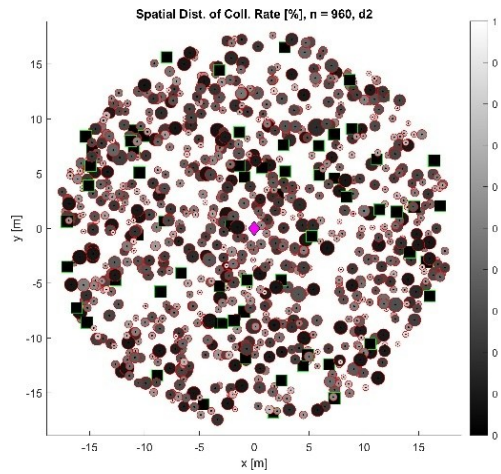

Figure IV-6 Spatial distribution of active MTs and its collision rates for uniform topology (n = 960).

This analysis highlights a key takeaway: the proximity of the MTs to the AP alone does not directly reduce the collision rate, as nearby MTs in different sectors still experience similar collision probabilities. Moreover, the even radial distribution of non-collided MTs across both topologies confirms that a

uniform angular spread of MTs can mitigate collision concentration in specific areas. These observations emphasize the need for strategies that address sector-based collisions specifically, rather than focusing solely on distance-based solutions. In all, the figures validate that the uniform distribution of MTs aids in balancing collision rates, making these insights valuable for optimizing future topologies and collision mitigation techniques.

Varying in the MTs number, it was necessary to calculate the population density parameter based on the area of the circle A ($\rho = n/A\ [m^2]$). Increasing the population density increases the collision rate linearly independent of the topology type, and that is what the Figure. IV-7 shows, however, the uniform distribution topology has a higher collision rate of 20% than the centered topology.

Moreover, ADAPT struggles with the compounded and progressively worsening effect of congestion in situations with large population densities, which is not usual with the traditional random MAC mechanisms used in practice (i.e., IEEE 802.11, IEEE 802.3…etc.).

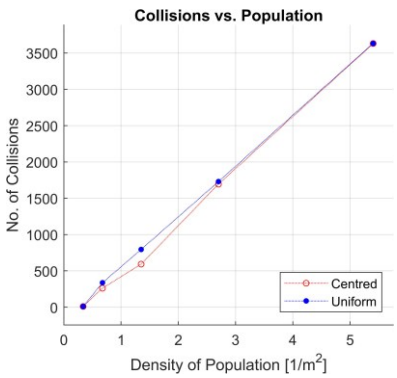

Figure IV-7 Impact of population density on collision rate.

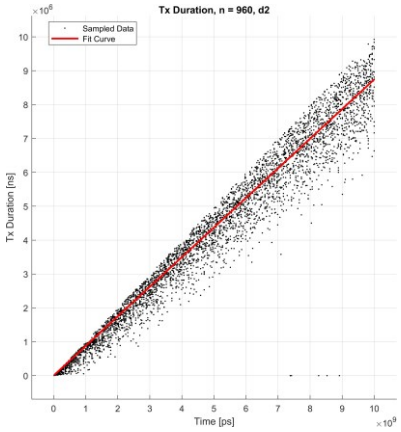

Figure IV-8 Effect of high population density on transmission duration.

Nevertheless, the transmission duration (the delay) of the successfully transmitted data frames in the case of high population density also increases linearly as time increases, having a slope $m_0 = 0.88$ (see Figure. IV-8).

Having a small number of MTs would cause no delay time in the transmission time (see Figure. IV-9), while increasing the MTs cause an increase in the slope (m_0) having a logarithmic dependency. Meanwhile, the topology type made no significant difference. Furthermore, analysing the received power by the MTs shows that it has fractal patterns (shown in Figure. IV-10), motivating us to study it in multiple resolutions as well as applying the wavelet transform.

These findings are crucial for improving the MAC protocol in high-density networks. Understanding how the MT density impacts collision rates, delay, and signal patterns can help design a protocol that minimizes congestion and improves efficiency.

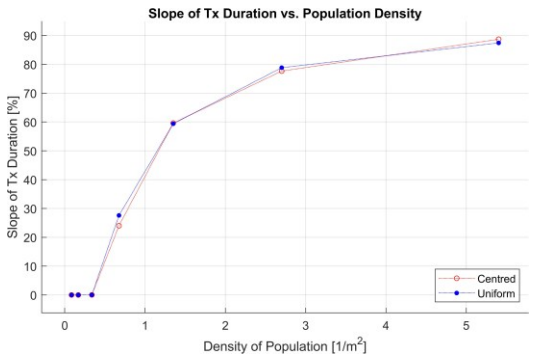

Figure IV-9 Impact of MTs number on the slope of transmission duration.

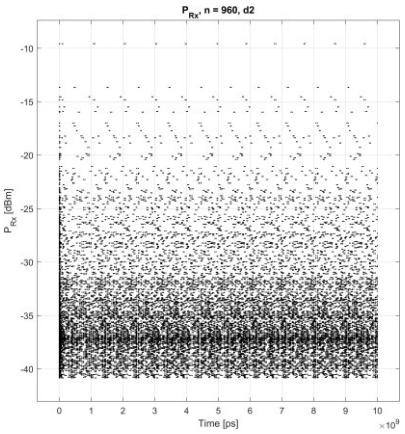

Figure IV-10 Fractal patterns in received power by MTs.

Insights into fractal patterns in received power suggest multi-resolution analysis that could enhance the protocol's adaptability and performance in dense environments, leading to more reliable and efficient wireless networks. Overall, this development supports diverse applications, enable scalability, and create a robust, efficient wireless communication ecosystem for the future.

IV.4. Dual-Parameter Integration-Based MAC Analysis

To enlarge the visibility of ADAPT properties and enhance the study, we suggested adding two different parameters to the macroscale code [J2, C2, C3]. In this subchapter, the primary system inputs are the overlapping ratio (m) and the rotation

step (s), which are varied systematically across simulation runs to observe their impact on throughput, fairness, and collision rate.

i. Overlapping ratio, m: It is introduced as a critical parameter to enhance the transmission opportunities for the MTs by allowing consecutive sectors to overlap. Every consecutive sector overlaps with a ratio m (Figure. IV-11 and Figure. IV-12) for increasing the transmission opportunities of the MTs:

$$m = \frac{A_{i+1}}{A_i} \tag{6}$$

A_i represents the area of the sector $i = 1, \dots, N$, where m takes the values $m \in \{0.1, 0.3, 0.5, 0.7, 0.9\}$. The essence of adding the overlapping ratio is because of its ability to create a more flexible and robust communication environment. By doing so, the MTs at the edge of one sector can still maintain a connection with the AP while transitioning to the adjacent sector, hence reducing the likelihood of dropped connections during movement or when initiating transmission. This strategy increases the spatial reuse of the communication medium, effectively multiplying the transmission opportunities for MTs by supporting them with a border coverage area. Meanwhile, it can also help mitigate the impact of interference by spreading transmission across overlapping sectors, which can be particularly beneficial in high-density environments where congestion is a concern. However, in highly congested areas, it might degrade the overall throughput. Additionally, managing the complexity of more active transmission may complicate resource allocation and scheduling, offsetting the intended benefits of improved coverage.

ii. Rotation step, s: represents the step that the AP takes in rotating between the sectors, defined with the following equation:

$$s = a(t_{i+1}) - a(t_i) (mod\ N) \tag{7}$$

Where $a(t_i)$ is the index of the sector at a certain moment t_i, and it takes the values $B = \{1,7,11,13,17,19,23,29\}$, choosing these values gives important properties for the set. One can observe that the elements of the set i are all prime except $s = 1$.

Set *B* has a twin relation, meaning that when you sum opposite position elements gives back always number of sectors N = 30 (1+29 = …= 13+17 = 30). Based on the algebraic Galois field, having an initial element a_i between 0 and N-1, we always get

back to the same element A_i after the N steps, the reason behind this property is the periodic rotation of the AP between the sectors.

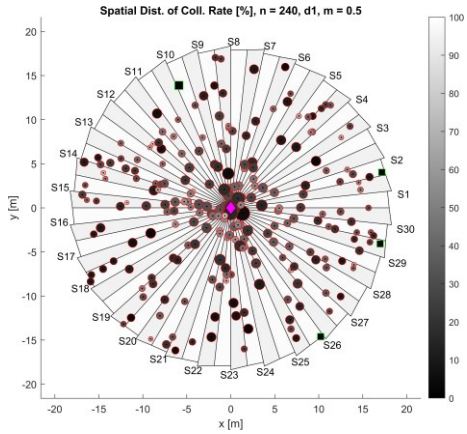

Figure IV-11 Collision rate spatial distribution for centered topology.

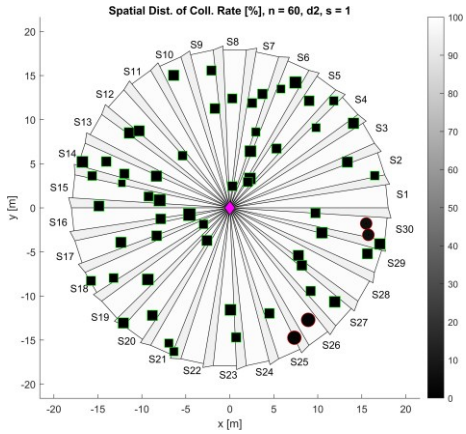

Figure IV-12 Collision rate spatial distribution for uniform topology.

The incorporation of the step parameter lies in its ability to facilitate periodic sector access, ensuring that the AP effectively covers all sectors without bias. By choosing values that are primarily prime, the rotation pattern minimizes collisions, enhancing transmission opportunities while maintaining a balanced load across sectors.

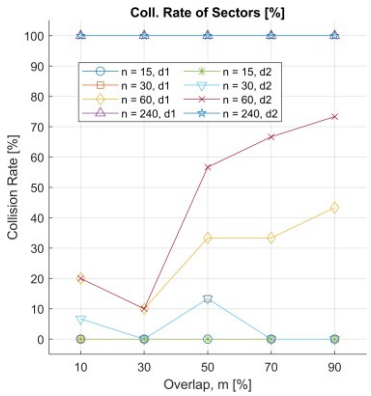

Figure IV-13 The dependence of the collision rate of sectors on the overlapping between consecutive sectors (s = 1).

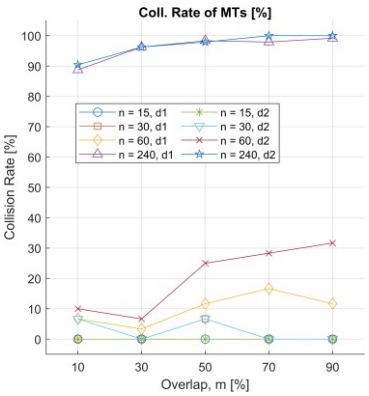

Figure IV-14 The dependence of the collision rate of MTs on the overlapping between consecutive sectors (s = 1).

Furthermore, the periodic nature of the rotation guarantees that starting from any initial sector index $a(t_i)$ (within the range of 0 to $N-1$ the AP cyclically returns to

the same sector after N step. This end ensures the consistency of the communication opportunities for the MTs as the AP systematically rotates, optimizing resource allocation and reducing latency by allowing time for MTs to prepare for transmission as the AP approaches their sector.

All in all, we could say that this rotation step improves coverage efficiency and enhances sector management while contributing to a more dynamic and responsive network architecture. Despite that, this parameter adds complexity to the system; its periodic nature limits flexibility, making it difficult to adapt to dynamic network conditions, which can be adapted based on real-time traffic demands. We plotted the dependency of the collision rate of the sectors and the MTs in Figure. IV-13 and Figure. IV-14, respectively, as it has been said earlier, as the MTs increase, the collision rate gets higher and higher, and when the cell contains a small number of MTs, no collision exists. However, the collision rate is dependent on the overlapping ratio parameter in cases when we have a medium population density. Understanding these dependencies is important for optimizing network performance, as it enables the design of strategies that mitigate collisions, ensuring smoother communication and improved reliability in high-density environments.

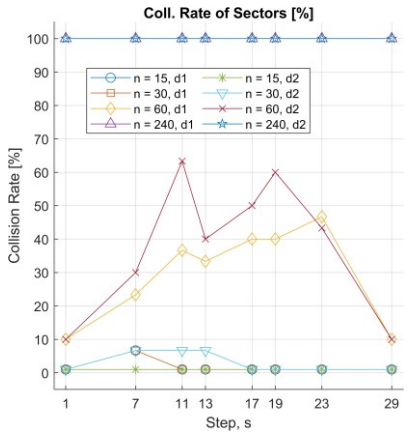

Figure IV-15 The dependence of the collision rate of sectors on step size, s.

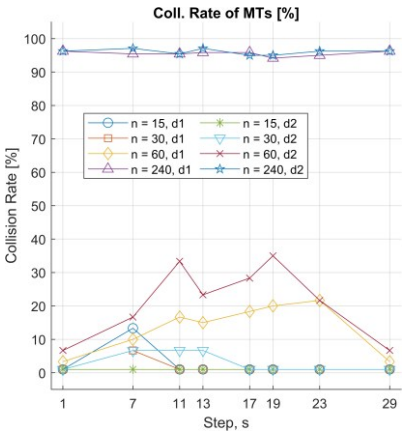

Figure IV-16The dependence of the collision rate of MTs on the step size, s.

Equivalently is happening in Figure. IV-15 and Figure. IV-16, which shows the dependence of the collision rate of the sectors and MTs on the rotation step s respectively, higher population leads to a higher collision rate, and low population

density has a small collision rate, but still collision rate behaves randomly as we increase the rotation step in medium population density, however, we can say that it is kind of symmetric to step $s = N/2$, where the reason is caused by the twin relation that exists in the step set. Recognizing these patterns is essential for refining sector rotation strategies and enhancing collision management, ultimately leading to improved network efficiency and performance.

The plotted figures demonstrate how varying these parameters impacts network performance, with the overlapping ratio enhancing the coverage and the rotation step ensuring systematic access to all sectors. As observed, a higher MT population leads to an increased collision rate, while lower densities reduce collisions significantly. Correspondingly, the interactions between these parameters reveal intricate dependencies that can be leveraged to refine network strategies.

CHAPTER V

DATA MULTIPROCESSING

Efficient processing and analysis of high-speed wireless networks simulated data are needed to understand the system behavior and optimize its performance. In this chapter we focus on applying various data processing methods on the network performance metrics to extract and study the 6G data properties. The main goal of the chapter is to evaluate these tools to characterize subsystem interactions, identify temporal and frequency-domain patterns with the aim of supporting the optimization of the MAC protocol and overall 6G system stability.

V.1. Shannon Entropy and Mutual Information Analysis

Shannon entropy and information theory offer valuable methods for analyzing subsystem interactions in the wireless networks field. It quantifies uncertainty, helping assess data transmission efficiency, while information theory uses mutual information to examine how changes in one subsystem impact the other. These metrics enable real-world benefits, such as adaptive protocols that respond to network load variation, reduce interference, and improve reliability. In this subchapter, we delve deeper into how Shannon entropy and mutual information can be applied to model and optimize the behavior of the overlapping ratio and the subsystems in communication systems, examining the effect on the received power, collisions, and network stability [J2, C5].

Calculating the Shannon entropy of the ADAPT mechanism helps in studying the efficiency of the MAC protocol, where it can be optimized to reduce collisions and idle times. Adding the overlapping ratio parameter to the ADAPT protocol divides the MTs into two different subsystems; Normal MTs (N) are the active mobile terminals that belong to only one sector having only one chance for communication per rotation, and Lucky MTs (L) are the active mobile terminals that locate on the overlapping area which make it belong to two different sectors, this property allows it to communicate with the AP two times per rotation. It should be mentioned that an active set of nodes is randomly elected at each rotation time. Two consecutive rotations have different active mobile terminals in the ADAPT cell around the AP. Analyzing the interdependence between these two subsystems using Shannon entropy could benefit in understanding how they would influence each other and aid in balancing the load

of the overall system. Therefore, we concentrate on evaluating the received power of the MTs by the AP during the communication period in each sector $e = 1, 2, \ldots, 2900$, The sector index e ranges from 1 to 2900, corresponding to the AP's rotation steps. Shannon entropy of the two subsystems (S_N, S_L) are given by the following formulae:

$$p_i^N[e] = \frac{P_i[e]}{\sum_{j=1}^{k} P_j[e]}, \quad i = 1,2, \ldots, k \tag{8}$$

$$S_N[e] = -\sum_{i=1}^{k} p_i^N[e] \cdot log\left(p_i^N[e]\right) \tag{9}$$

$$p_i^L[e] = \frac{P_i[e]}{\sum_{j=k+1}^{n} P_j[e]}, \quad i = k+1, k+2 \ldots, n \tag{10}$$

$$S_L[e] = -\sum_{i=k+1}^{n} p_i^L[e] \cdot log\left(p_i^L[e]\right) \tag{11}$$

Here, n denotes the total number of active MTs in the system, while k represents the number of normal MTs (the remaining $n - k$ correspond to the lucky MTs located in the overlapping areas). We note that any entropy (equations: (9) and (11)) is a non-negative number and a zero entropy may be in a situation when no active MT exists ($p[e] = 0$) or just one active MT exists ($p[e] = 1$) in the zone of overlapping sectors. By active MT, we mean a node wanting to send data to the AP, and its RTS control frame sent back to the AP is non-colliding. In these two cases $p[e] \cdot log(p[e]) = 0$. For the case $p[e] = 0$ the zero entropy value is an asymptotic limit. In the previous equations, the total entropy of the whole subsystem is as follows:

$$p_i[e] = \frac{P_i[e]}{\sum_{j=1}^{n} P_j[e]}, \quad i = 1,2, \ldots, n \tag{12}$$

$$S_{Tot}[e] = -\sum_{i=1}^{n} p_i[e] \cdot log(p_i[e]) \tag{13}$$

$P_i[e]$ is the received power of the MT i by the AP in each sector e. $S_N[e]$, $S_L[e]$ and $S_{Tot}[e]$ represents the entropy of the normal MTs, lucky MTs, and the total mobile terminals, respectively. p_i^N, p_i^L and p_i represents the probability variables of the normal MTs, lucky MTs, and overall system, respectively.

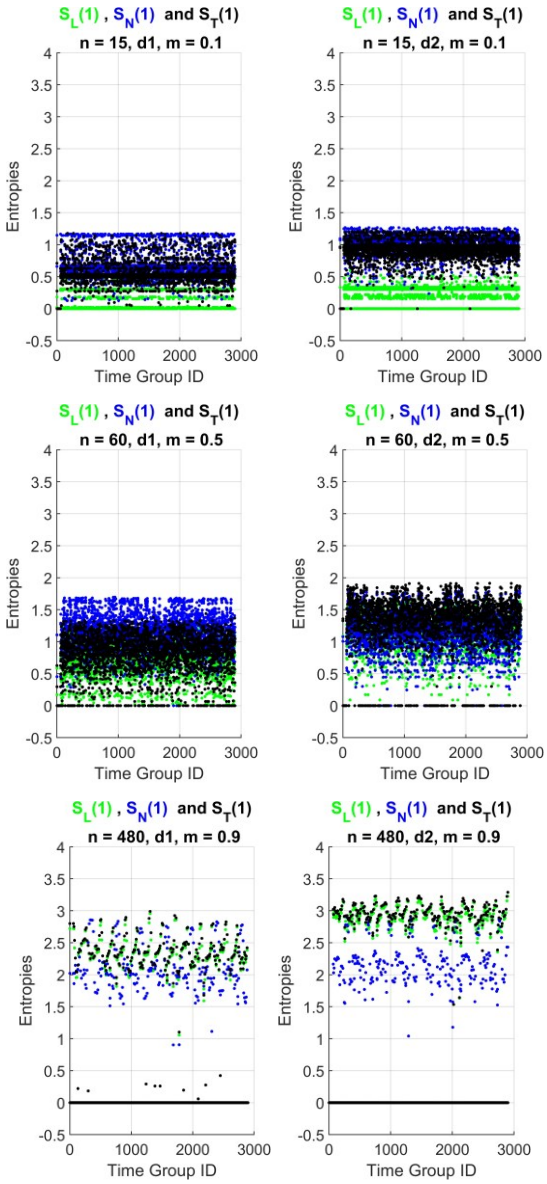

Figure V-1 Entropy analysis of subsystem interdependence for six simulation cases (Time Group ID refers to the index of the AP's rotation step during which entropy values are computed).

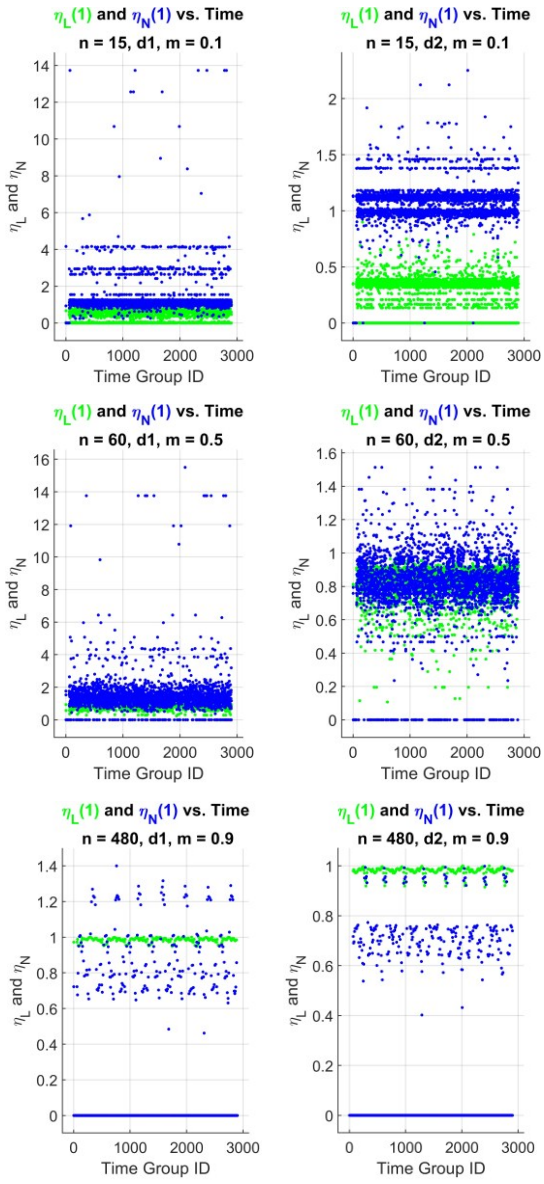

Figure V-2 Entropy ratios analysis of subsystem interdependence for six cases (Time Group ID refers to the index of the AP's rotation step during which entropy values are computed).

In each sector e, the probabilities have the following property:

$$\sum_{i=1}^{k} p_i^N[e] = \sum_{i=k+1}^{n} p_i^L[e] = \sum_{i=1}^{N} p_i[e] = 1 \qquad (14)$$

In the case of independence of the two subsystems, the validity of the following relation is considered:

$$S_{Tot}[e] = S_N[e] + S_L[e] \quad (15)$$

We quantitatively evaluate the interdependence of the separated subsystems by examining the entropy, as shown in the Figure. V-1, where we thought of studying different internal aspects like randomness, stationary, or the existence of any patterns.

Hence, using the Phillips-Perron test we calculated the stationarity of the entropies by a binary digit where 0 – non-stationary and 1- stationary, which are written inside the parentheses of in the following figures: Figure. V-1, Figure. V-2, Figure. V-4 and Figure. V-5, we have also noticed the presence of patterns during the complete rotation of the MAC protocol due to the periodicity spin that the AP makes. Zero entropies in Figures V-6, V-7 present zero or just one active MT in the sector zone corresponding to the time group. The order of dots plotting to represent entropies in Figure. V-1 is lucky MTs (green), normal MTs (blue), and then all MTs (black). If the total entropy is zero, then both lucky and normal entropies might be zero, and black dots hide other dots. When only lucky MTs have zero entropy, then total entropy is greater than zero and green gets are visible (n = 15 and n = 60 in Figure. V-1).

For larger population cases (n > 60 in Figure. V.1), rare green dots are hidden by the black dots. The reason is that population increase may cause collisions more frequently, and that leads to a higher number of zero total entropies. However, the entropy values increase with the population density. Also, the topology type has a global impact on the entropies: d2 has greater values, with 12% for d1. In the case of d1 (centered) topology, the density of MTs around the AP is greater than for d2, implying a higher probability of collisions in that region. The number of remaining active MTs becomes small, resulting lower number of positive terms in the formulae (9), (11), and (13).

The entropy difference approaches zero as the two subsystems' independence increases:

$$\Delta S[e] = S_N[e] + S_L[e] - S_{Tot}[e] \quad (16)$$

The Mutual Information (MI) measures the amount of information between two subsystems, quantifying their dependence. It helps identify how much knowing one

variable reduces uncertainty about the other. MI has a relationship with Shannon entropy based on equation (16), as it was mentioned in [69]:

$$I[e] = S_N[e] + S_L[e] - S_{Tot}[e] \tag{17}$$

In this equation (17), $I[e]$ denotes the MI that captures the overlap information between the N and L subsystems, reflecting their interdependence. A higher $I[e]$ implies a stronger connection, while a lower $I[e]$ suggests greater independence between subsystems.

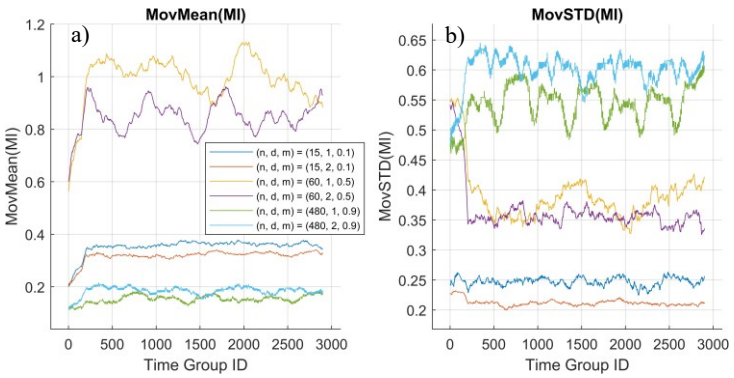

Figure V-3 Moving mean (a) and moving standard deviation (b) of Mutual information of L and N subsystems (Time Group ID refers to the index of the AP's rotation step during which entropy values are computed).

Figure. V-3 (a) and (b) depict the moving mean and moving standard deviation, respectively, of the MI between the two subsystems across six different cases. In Figure. V-3 (a), the moving mean of the MI decreases as the overlapping ratio increases. This trend indicates that greater overlap between the sectors reduces the interdependence, as more overlap creates redundancy, leading to less unique information shared between them. Conversely, Figure. V-3 (b) shows that the moving standard deviation behaves differently, it peaks at the highest overlapping ratio of $m = 0.9$, indicating greater variability in the MI due to the pronounced interactions and redundancy in highly overlapping scenarios. The overlapping ratio of $m = 0.1$ has intermediate variability, suggesting moderately dynamic interaction. Interestingly, the lowest variability occurs at an overlapping ratio of $m = 0.5$, implying that the middle-ground overlap stabilizes MI, balancing shared and unique information dynamics. Together, these two figures demonstrate how the extent of subsystem

overlap influences both the average interdependence and its variability, reflecting the complex interplay between redundancy and distinctiveness in MI. The interplay of overlapping ratios m offers valuable insights into system performance, which highlights how varying in this parameter impact the stability and variablity of MI.

Based on the calculated entropy of the two subsystems in equations (9) and (11), and the total entropy in equation (13) of the ADAPT system, we compute the entropy ratio as follows:

$$\eta_N[e] = \frac{S_N[e]}{S_{Tot}[e]} \tag{18}$$

$$\eta_L[e] = \frac{S_L[e]}{S_{Tot}[e]} \tag{19}$$

The entropy ratio is the entropy of the two calculated subsystems over the total entropy of the system. By dividing the combined entropy of the subsystems by the overall system's entropy, these ratios offer insight into the degree of interdependence or independence between the two subsystems. A high entropy ratio suggests that the subsystems are relatively independent, as their combined entropy approaches the total system entropy (see Figure. V-3), entropy ratios for the active normal MTs (blue dots) for low to medium population density (15 and 60). Conversely, a low entropy ratio indicates strong interdependence, meaning that information or changes in one subsystem significantly influence the other (see Figure. V-2), entropy ratios for the active lucky MTs (green dots) for most of the cases), the higher entropy ratio for the active normal MTs compared to the lucky MTs likely stems from the limited access opportunities active normal MTs have. Since active normal MTs can only communicate with the AP at most once per rotation, their chances are constrained, leading to higher uncertainty in the access success. In contrast, the active lucky MTs have a more predictable access pattern, reducing their entropy ratio. This difference suggests that access reliability is higher for the active lucky MTs, while the active MTs face more variability. In rare cases (like in Figure. V-2, the case having 480 MTs, overlapping ratio 0.9, and uniform topology) higher entropy ratio for active lucky MTs may occur due to increased congestion or interference in the overlapping area, causing more variability in their access attempts.

We calculated a metric called the Inter-Subsystem Mutual Effect (M) to evaluate the mutual effect between the two subsystems using the following formula:

$$M[e] = \eta_N[e] + \eta_L[e] - 1 \quad (20)$$

The inter-subsystem mutual effect metric evaluates the interdependence level between the two subsystems, M being closer to zero indicates a high level of interdependency (see Figure. V-4), conversely, further analysis needs to study the significance of nonzero M.

The inter-subsystems mutual effect quantifies the interaction strength between the two subsystems. M being 0 ($M = 0$) indicates minimal or no mutual influence, suggesting that the two subsystems function independently without affecting each other's entropy significantly. For $M = -1$, we have both entropy ratios of the subsystems N and L equal to zero, meaning no active MT exists or just one active MT exists in the N and L subsystems. Another important information is that the metric M is strongly related to the low-pass filter (LPF), as it aggregates the influence of both subsystems and smooths out rapid fluctuations in entropy ratios, reflecting a long-term mutual effect. This end aligns with LPF characteristics, which capture low-frequency trends over time. As the number of MTs increases, the M metric stabilizes between 0.5 and 1 for centered topology (shown in Figure. V-4). This observation indicates that with more MTs, the mutual influence between these subsystems becomes more pronounced, leading to consistent interaction patterns that enhance communication efficiency across different topologies. Also, this concentration reflects a system nearing equilibrium, where interactions among normal and lucky MTs become more predictable.

Moreover, the Relative Entropy Difference (R) calculates the balance of the system (see Figure. V-4). We calculated it based on the following formula:

$$R[e] = \eta_N[e] - \eta_L[e] \quad (21)$$

R being closer to 0 declares the equilibrium of the two subsystems, which suggests that both subsystems experience similar uncertainty and variability in accessing the AP, reflecting a balanced communication opportunity. Such equilibrium minimizes congestion and interference, promoting stable network performance and ensuring fair resource distribution among MTs. In contrast to the M metric, the R metric, calculated

as the difference between the entropy ratios of normal and lucky MTs, functions similarly to a high-pass filter (HPF). Case ($R = 0$) means the entropies of the N and L subsystems are the same, ($S_N = S_L$). Highlighting the variability and sharpening the contrasts between the subsystems' entropy levels, detecting high-frequency shifts that indicate immediate differences in access opportunities or congestion impact. In low population density scenarios, the R metric shows more negative values than positive ones, suggesting that the active normal MTs have more predictable access patterns compared to lucky MTs. Nevertheless, as population density rises, R approaches 0, indicating a more balanced communication opportunity for both subsystems. This shift occurs due to increased competition for resources, which leads to a more equitable distribution of access opportunities as the network becomes denser.

The stability can be proved by the metrics M and R as follows: the two metrics are bounded quantities ($-1 \leq M \leq 1, -1 \leq R \leq 1$) that converge over time. In particular, as the number of MTs increases, M stabilizes around a constant value M^*, while R approaches zero, indicating balance between the two subsystems. This convergence can be also expressed as the following: $\lim_{n\to\infty} M[e] = M^*$ and $\lim_{n\to\infty} R[e] = 0$.

It is so important to study the behavior of both introduced entropy ratio metrics, therefore, we tend to write both metrics in matrix form, and this is what the matrix equation presents:

$$\overline{D[e]} = \bar{T} \cdot \overline{H[e]} + \bar{C} \tag{22}$$

Having $\bar{D} = \begin{pmatrix} R \\ M \end{pmatrix}$ and $\bar{H} = \begin{pmatrix} \eta_N \\ \eta_L \end{pmatrix}$, both of them being time-dependent, while $\bar{T} = \begin{pmatrix} 1 & -1 \\ 1 & 1 \end{pmatrix}$ and $\bar{C} = \begin{pmatrix} 0 \\ -1 \end{pmatrix}$ being constant, the transformation is about making a rotation by $\pi/4$ firstly, then zoom in with $\sqrt{2}$ secondly, and shifting toward $-\infty$ in the dimension of M by one unit lastly. This transform magnifies and presents the entropy ratios' behavior in the new state space given by the {M, R} metric pair. By highlighting shifts and patterns, the {M, R} pair helps to discover dependencies and dynamic interactions between subsystems that can be leveraged to optimize communication protocols, reduce interference, and enhance overall network stability. The usefulness

is supported by the observed patterns in the plotted figures of M and R (Figure. V-4) that demonstrate system stability and equilibrium under varying conditions. These results confirm that the matrix transformation effectively highlights the balanced interaction between subsystems, making it an essential tool for optimizing system performance and stability.

Furthermore, studying the derivatives of the metric pair would emphasize more in its behavior (see Figure. V-5), therefore we have the following formulae:

$$M^1 = \Delta M = \Delta\eta_N + \Delta\eta_L \quad (23)$$

$$R^1 = \Delta R = \Delta\eta_N - \Delta\eta_L \quad (24)$$

One can notice, that by calculating the derivative, the scale got enlarged guarding the original pattern depending on the simulation scenario case and the parameters m, n, and d. This scale adjustment brings subtle variations into clearer focus, revealing periodic shifts and fluctuations that may otherwise be overlooked. This finding is crucial for tracking rapid changes in entropy ratios, enabling fine-tuning of parameters for enhanced adaptability and robustness in practical applications.

Since the metrics remain bounded and their derivatives (ΔM, ΔM) do not diverge, the system can be considered mathematically stable. Therefore, the proposed metrics not only provide an intuitive visualization but also satisfy analytical conditions of boundness and convergence that are commonly used in stability analysis.

The suggested Shannon entropy metrics are closely tied to the overlapping ratio in the 6G MAC mechanism, reflecting how various subsystems interact and share resources. These metrics offer quantitative means to evaluate the communication power and performance of the mobile terminals within the ADAPT system. The derivative of entropy ratios quantifies the divergence or difference in information flow between subsystems, making it crucial to understand how well the MTs can maintain robust communication under different transmission conditions. The relation between the entropy metrics {M, R} and {LPF, HPF} helps in analyzing the communication dynamics. The LPF emphasizes the steady-state behavior and tends to information flow, allowing for a clearer understanding of how subsystems stabilize over time. Meanwhile, LPF shows rapid changes and anomalies, providing insight into transient behaviors during peak loads.

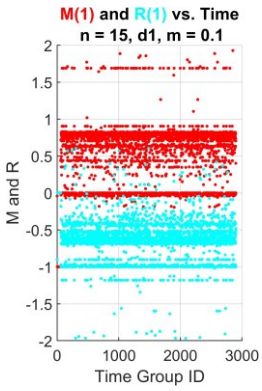

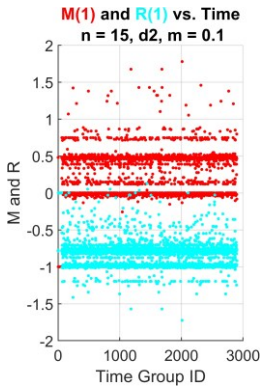

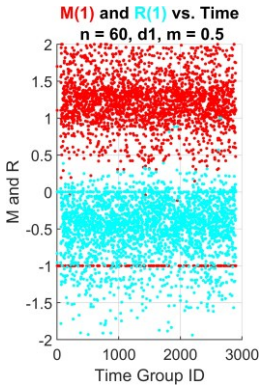

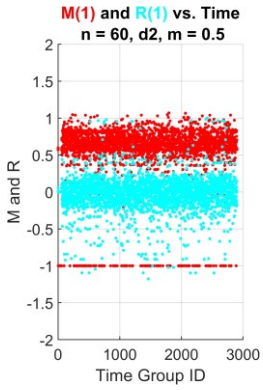

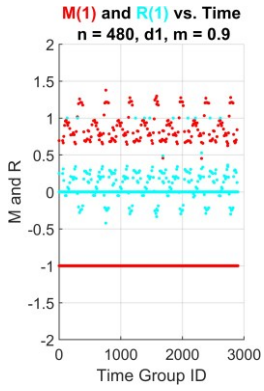

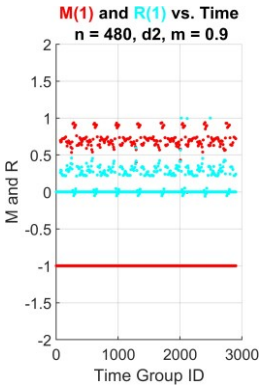

Figure V-4 Entropy ratios-based metrics behavior for six different simulation cases (Time Group ID refers to the index of the AP's rotation step during which entropy values are computed).

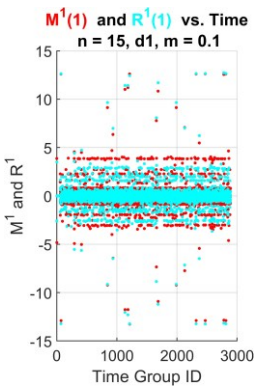

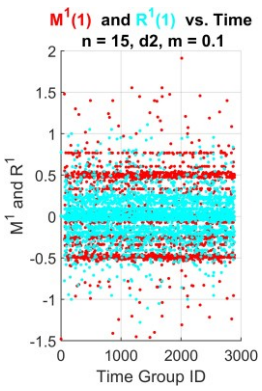

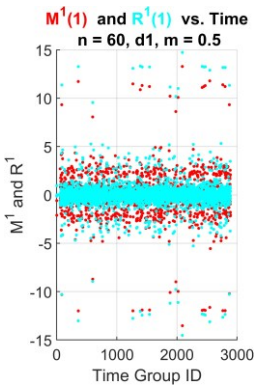

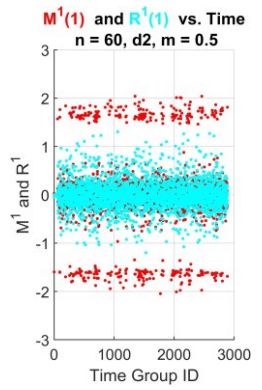

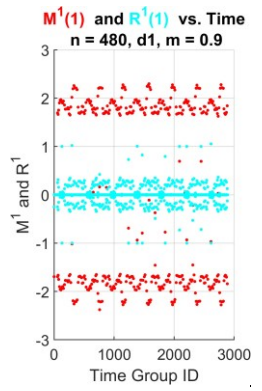

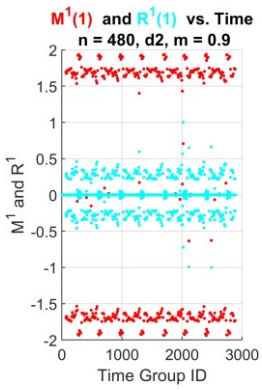

Figure V-5 The first derivative of entropy ratios-based metrics behavior for six different simulation cases (Time Group ID refers to the index of the AP's rotation step during which entropy values are computed).

Ultimately, these insights not only enhance our understanding of subsystem dynamics but also inform the development of adaptive strategies that can optimize resource allocation and improve overall network reliability and efficiency in future wireless communication systems.

V.2. EMD and EEMD-Based Decomposition for Temporal Behavior Analysis in 6G Networks

Empirical Mode Decomposition

EMD can be applied to a nonlinear and non-stationary signal. Although it is a sophisticated method for feature extraction. EMD decomposes the signal into a finite number of IMFs plus the residual. The decomposition process involves identifying all extrema of the signal *X(t)* and connecting them with the help of cubic splines to obtain an upper and a lower envelope [70]. It calculates the mean of the upper and lower envelope *m1*, then subtracts it from the original signal to obtain the first component *h1* (equation (25)). However, the resulting IMF most of the time is not the right IMF because it does not satisfy the necessary conditions. Therefore, the sifting process is used and repeated to refine the IMF by eliminating riding waves, making it more symmetric, and smoothing uneven amplitudes.

$$X(t) - m_1 = h \tag{25}$$

By doing so, the resulting IMF is then subtracted from the original signal to obtain a residue signal (equation (26)) where *c1* is the IMF after *j* sifting times.

$$X(t) - c_1 = r_1 \tag{26}$$

IMF1 is then decomposed into the second IMF using the same process. This process is repeated until the last residual. However, like any other processing method, EMD struggles with some limitations that should be considered, such as the end effect, where the first and the last points, most of the time are not the extreme values. Also, the mode mixing limitation occurs when the IMF components overlap and cannot be separated from each other. It can happen when the signal has multiple scales of variation, leading to a difficult interpretation of the IMF components [71].

Ensemble Empirical Mode Decomposition

EEMD is an advanced technique designed to enhance the traditional EMD method, specifically tailored for the analysis of non-stationary and nonlinear signals. One of the key challenges faced by EMD is the presence of the mode-mixing problem, which can result in inaccuracies during signal analysis. To overcome these limitations,

EEMD introduces a novel approach by incorporating an ensemble of white noise into the original signal before applying the EMD method. This addition of white noise ensures that each iteration of the EMD process produces slightly different results, effectively mitigating the mode-mixing problem.

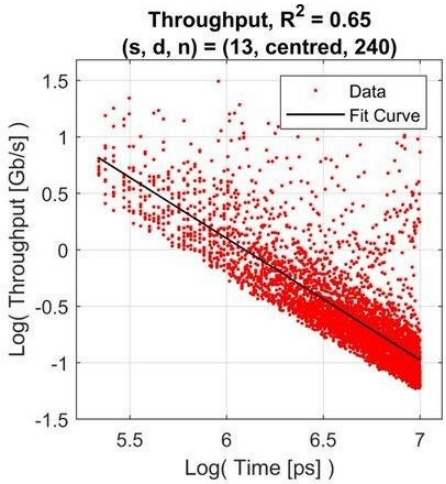

Figure V-6 Dependence of throughput on the time (n, d, s) = (240, 1,13).

EEMD process involves several steps: Firstly, the original signal is combined with white noise, leading to the generation of multiple noisy versions of the signal. The traditional EMD method is applied independently to each of these noisy signals, extracting a set of IMFs from every iteration. Finally, the IMFs obtained from all iterations are averaged, yielding the final IMFs. Through this ensemble approach, EEMD successfully overcomes the limitations of traditional EMD and improves the accuracy of the extracted IMFs, representing more faithfully the underlying components of the signal. This enhancement proves particularly valuable when dealing with intricate and non-stationary signals, enabling more dependable time-frequency analysis and extraction of signal characteristics.

Simulation and Analysis

We generated 42 different cases. The generated cases are based on the following varied inputs: 7 different number of steps having the properties mentioned previously and in [J1] (s = 1, 7, 11, 13, 17, 19, 23), two different topologies d1, and three different

numbers of MT ($n = 60, 240, 960$) having the overlapped ratio fixed $m = 0.3$. While the fixed inputs remain the same as mentioned in Table IV-1.

The behavior of the throughput is particularly intriguing, as its distribution exhibits a gradual decrease over time, as illustrated in Figure. V-6. This trend is further confirmed and supported by the fit curve, which aligns with the decreasing pattern of the throughput as time progresses. The representation declines the nature of the THz throughput, and the fit curve provides a mathematical model that captures and validates this diminishing trend. The combination of empirical evidence from the distribution plot and the fit curve's analytical support strengthens the significance of this observation.

Since non-stationary and nonlinear systems in high-speed wireless communication networks require special signal processing methods, EMD can be a suitable approach. Consequently, we have decided to use EMD to decompose the throughput data of ADAPT and analyze the obtained results. To observe the impact of applying the EMD on throughput analysis, we decided to apply EMD in a direct way from $time_{start}$ to $time_{end}$, and then inversely from $time_{end}$ to $time_{start}$. The results of this experiment show the resulting IMFs of the direct and inverse methods plotted versus the time (Figure. V-7 and Figure. V-8).

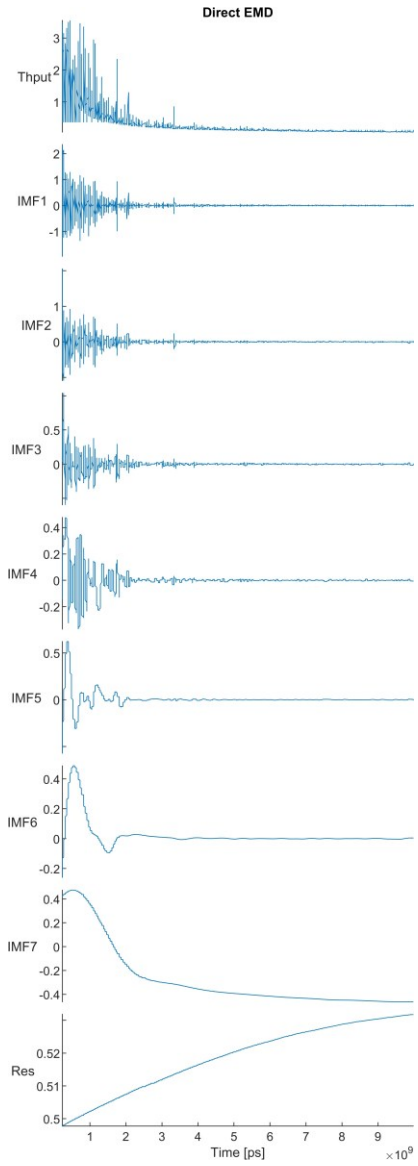

Figure V-7 Direct EMD on Throughput vs. time (n, d, s) = (960, 1, 7).

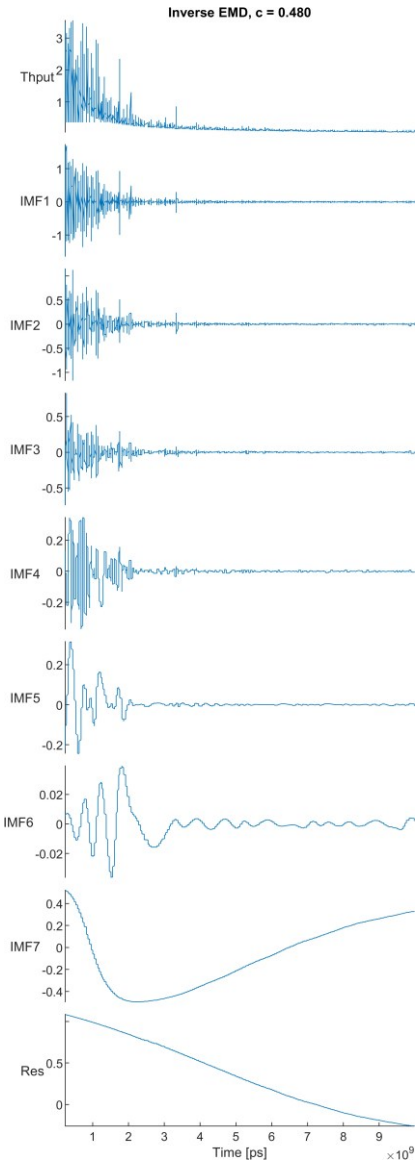

Figure V-8 Inverse EMD on Throughput vs. time (n, d, s) = (960, 1, 7), c = 0.48.

Our observation from the results was that the IMFs generated by the direct and inverse methods were significantly different, despite having different amplitudes for the same IMFs. This difference was further confirmed by a correlation coefficient of less than *0.5* ($c = 0.48$), which indicates that EMD is direction-dependent.

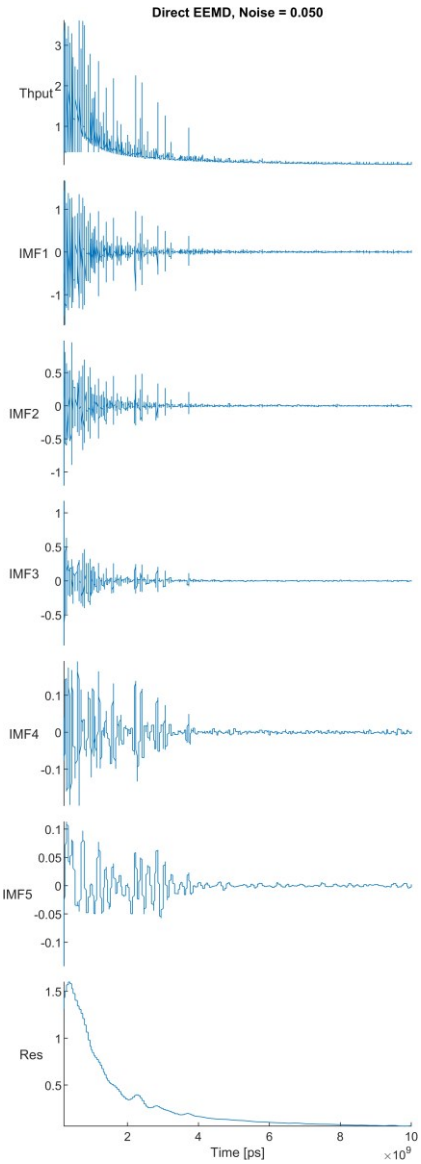

Figure V-9 Direct EEMD on Throughput vs. time (n, d, s) = (960, 1, 23), noise = 0.05.

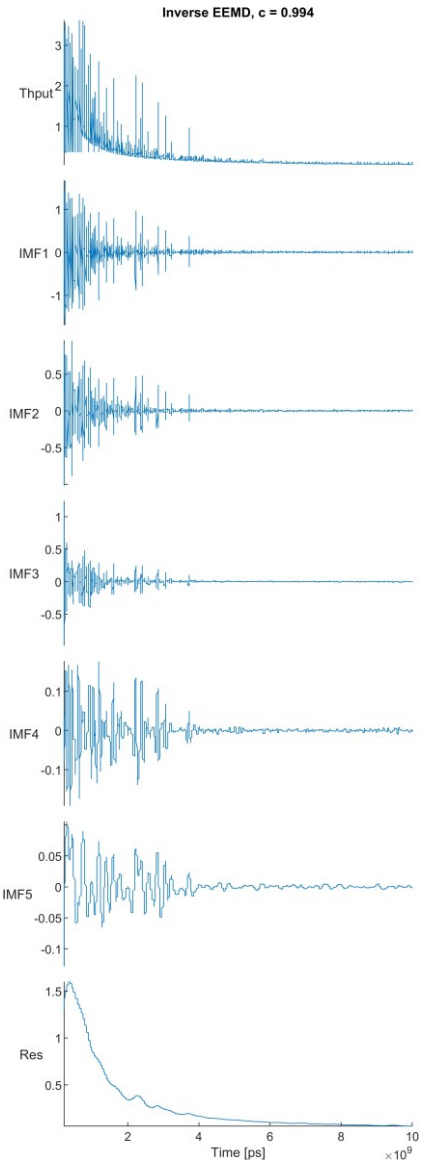

Figure V-10 Inverse EEMD on Throughput vs. time (n, d, s) = (960, 1, 23), c = 0.994.

The experiment was repeated using EEMD with 5 percent white noise. The IMFs generated by the direct and inverse methods were identical, despite having the same amplitude (Figure. V-9 and Figure. V-10).

This finding was confirmed by a high correlation coefficient c = 0.994, which indicates that EEMD is direction-independent.

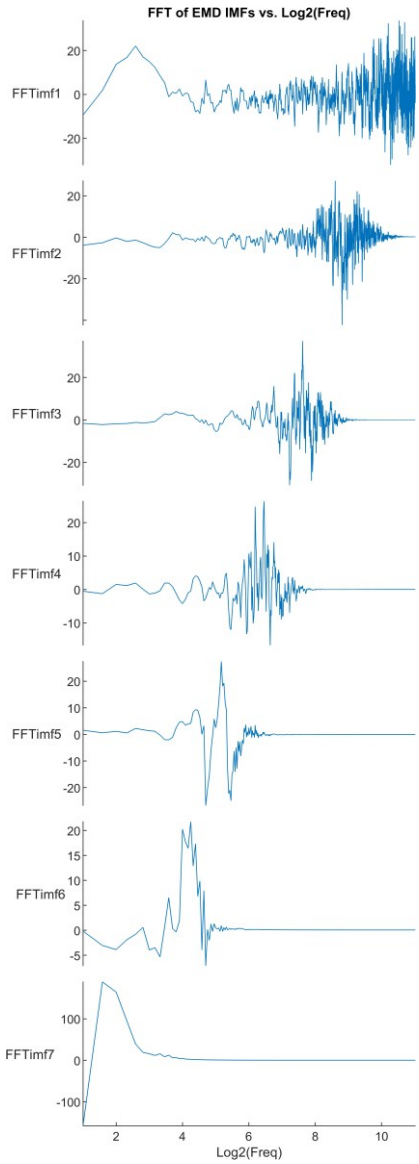

Figure V-11 FFT on the calculated IMFs vs. frequency, (n, d, s) = (960, 2, 11).

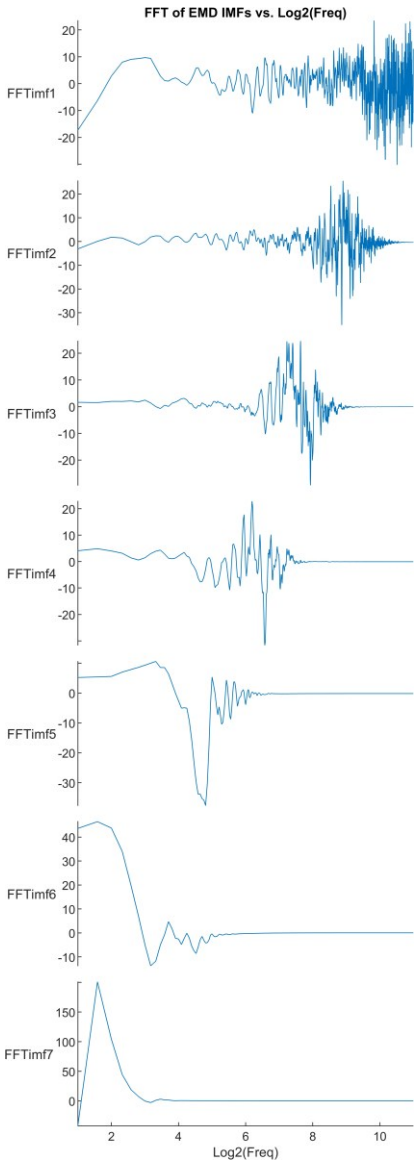

Figure V-12 FFT on the calculated IMFs vs. frequency, (n, d, s) = (960, 1, 7).

We came up with the idea of using the Fast Fourier transform on the IMFs resulting from EMD to extract the frequency information. The FFT gives adjacent sub-frequency bands in log2 of the frequency for adjacent IMFs, which is reminiscent of the dyadic filter bank (See Figure. V-11 and Figure. V-12).

For extracting the trend using the IMFs components, one approach is, to sum up, each k consecutive IMFs together with the residual components (as Figure. V-13

shows). It is obvious that if the number of IMFs included in each sum is precisely equal to k, then the resulting trend exactly matchs the original throughput signal.

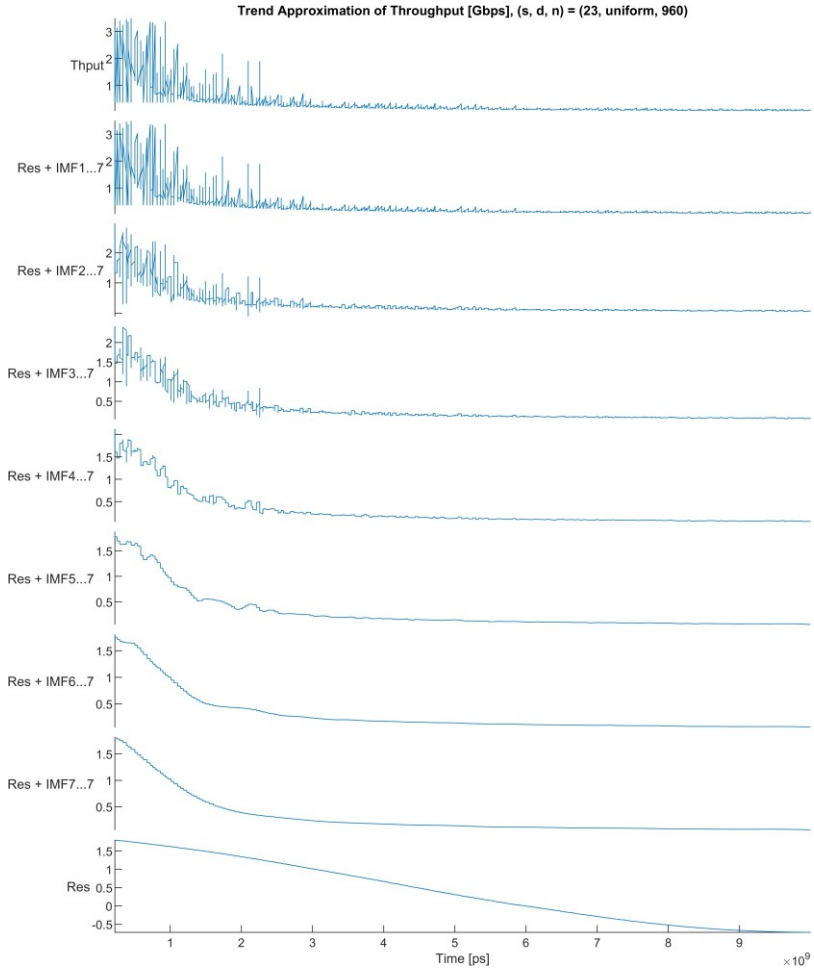

Figure V-13 IMFs-based trends vs. time (n, d, s) = (960, 2, 23).

To select the optimal trend among the potential options, we suggest employing a Root Mean Square Error (RMSE) calculation to compare each trend candidate against the original signal. The trend component with the smallest non-zero RMSE is chosen as the final trend. This approach ensures that the selected trend is as close as possible to the original signal. The RMSE values are plotted versus $trend_k$ in centered topology, $step = 23$, and $n = 960$ (Figure. V-14).

By analyzing this graph, it becomes possible to visually identify the trend component with the smallest non-zero RMSE and thus select the optimal trend for the given dataset.

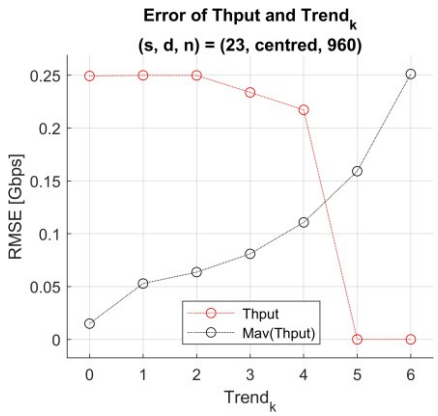

Figure V-14 The error of throughput and trend.

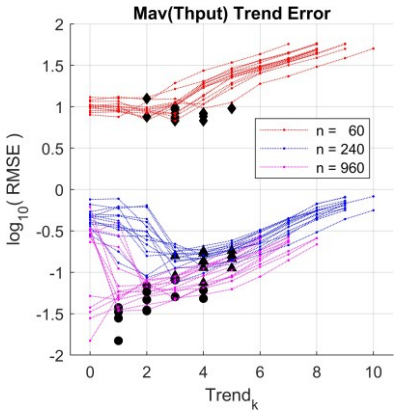

Figure V-15 RMSE of throughput and IMF-based trend.

The visualization of RMSE values versus $trend_k$ for all 42 cases simultaneously allows us to observe that the chosen $trend_k$ differs from case to case (Figure. V-15). By examining this graph, we can identify that there is no single trend component that performs optimally across all cases. Instead, the optimal trend varies depending on the specific dataset under consideration. Therefore, it is important to perform an individualized analysis for each dataset to determine the appropriate trend component. This approach ensures that the chosen trend is both accurate and effective for a given dataset, leading to more reliable results and better decision-making.

The ability to observe and understand the variability in RMSE and $trend_k$ across different cases highlights the importance of customizing analysis to specific datasets and avoiding generalizations. To enhance our analysis, we included a fit curve of the original throughput dataset in addition to the chosen trend and the original data. This fit curve provides a visual representation of the overall trend in the data and facilitates the comparison of the chosen trend with the original signal (Figure. V.16 presents a plot showing all 42 cases together). Upon examining this graph, it is apparent that the chosen trend and the fitting curve are quite similar in the majority of cases. This similarity indicates that the selected trend is an accurate representation of the

underlying trend in the data. However, there are some cases where the chosen trend deviates significantly from the fitting curve.

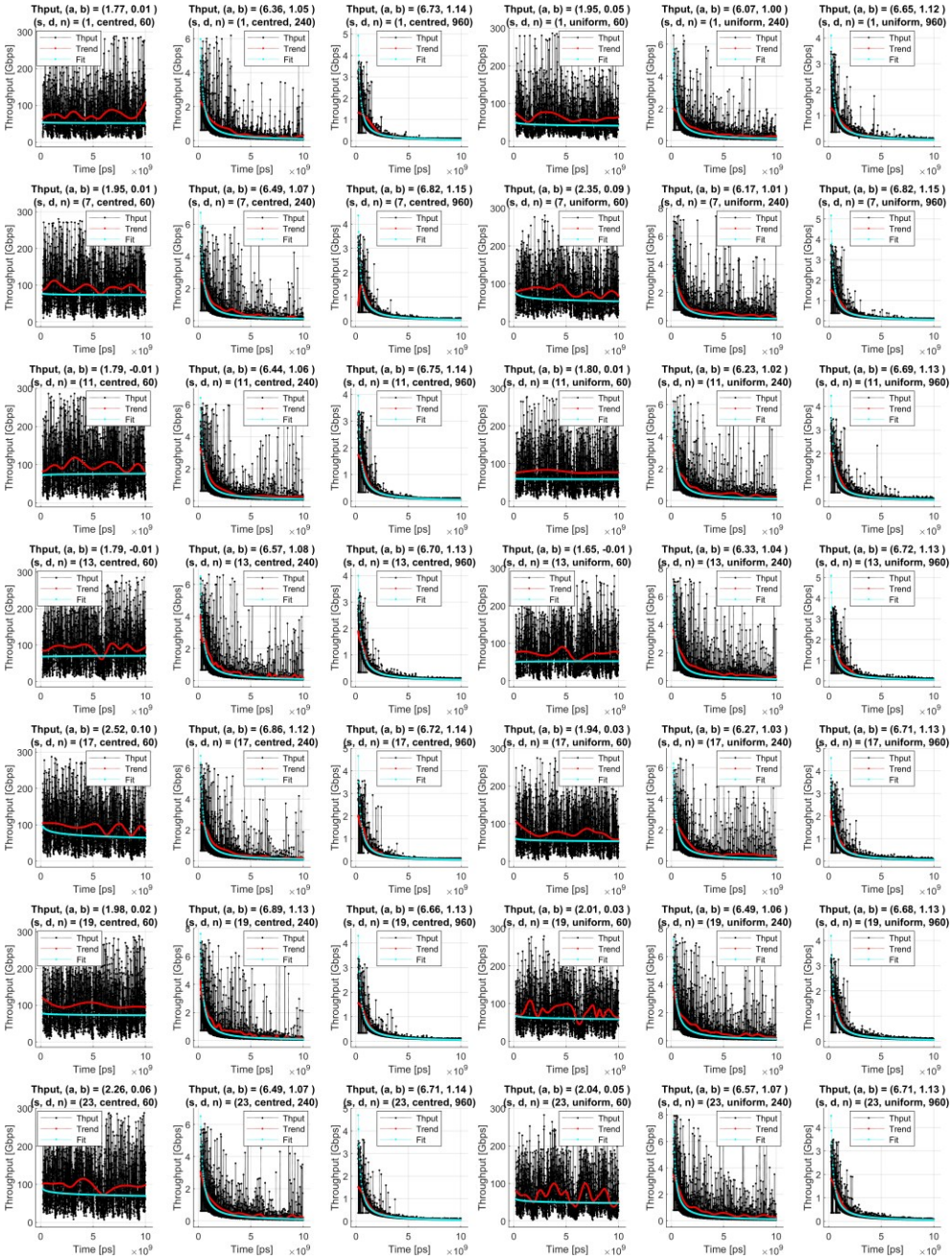

Figure V-16 Dependence of throughput, trend, and fir curve on time.

These deviations may be the result of outliers or other anomalies in the data. By comparing the chosen trend and the fitting curve in this manner, we can gain a more comprehensive understanding of the data and make more informed decisions based on the analysis results.

Upon applying the fitting curve to the original signal, we meticulously extracted the fitting parameters and subsequently generated a scatter plot to provide visual insight into the outcomes of parameters **a** and **b** (as depicted in Figure.V-17). Notably, the red-highlighted cluster is associated with instances of lower congestion levels, while the black cluster corresponds to more congested cases.

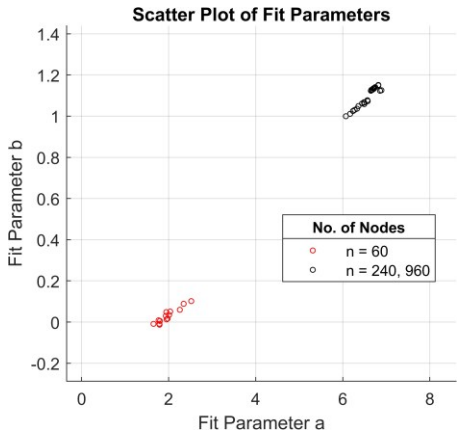

Figure V-17 Scatter plot of the fit parameters.

These findings strongly imply that the fitting parameters, specifically parameters **a** and **b**, hold promising potential as valuable indicators for discerning and characterizing network congestion states. Such observations signify the scientific relevance and significance of the proposed methodology in understanding and quantifying the complexities of network congestion in our study.

V.3. Marginal Hilbert Spectrum for Directional MAC Signal Analysis

The marginal Hilbert spectrum is a powerful tool that provides a time-frequency distribution of a signal by examining its instantaneous frequencies and amplitudes over time [J3]. This technique helps us understand how different frequency components of the signal evolve and contribute to its overall behavior, which is useful for signals in high-speed communication systems where the frequency can change

rapidly. MHS is related to the instantaneous frequency and amplitude of a signal. It is a 2D representation of the HHT, where the HHT of a signal *x(t)* is as follows:

$$H\{x(t)\} = y(t) = \frac{1}{\pi} P \int_{-\infty}^{\infty} \frac{x(\tau)}{t-\tau} d\tau \tag{27}$$

P is the Cauchy principal value, and based on *x(t)* and *y(t)* the analytic signal, $z(t) \in \mathbb{C}$ is as follows:

$$z(t) = x(t) + iy(t) \; = \; a(t)e^{i\theta(t)} \tag{28}$$

We have $a(t)$ is the amplitude and $\theta(t)$ represents the phase, and is defined as follows:

$$a(t) = [x^2(t) + y^2(t)]^{1/2}, \theta(t) = arctan(\frac{y(t)}{x(t)}) \tag{29}$$

$\omega(t)$ represents the instantaneous frequency of $x(t)$ and is given as follows:

$$\omega(t) = \frac{d\theta(t)}{dt} \tag{30}$$

resulting in the signal decomposition with the formula conforming to the equation (27). Moreover, the MHS is defined as follows:

$$h(\omega) = \frac{1}{T} \int_0^T H\,(\omega, t) dt \tag{31}$$

T is the length of the sampled input signal $x(t)$. For high-speed communication technologies, such as 5G or beyond, MHS is useful in analyzing rapidly changing signals where traditional methods might fall short. It allows engineers to track how the signal's frequency evolves, helping to detect interference, optimize performance, and ensure better signal quality in environments with a lot of noise or rapid changes.

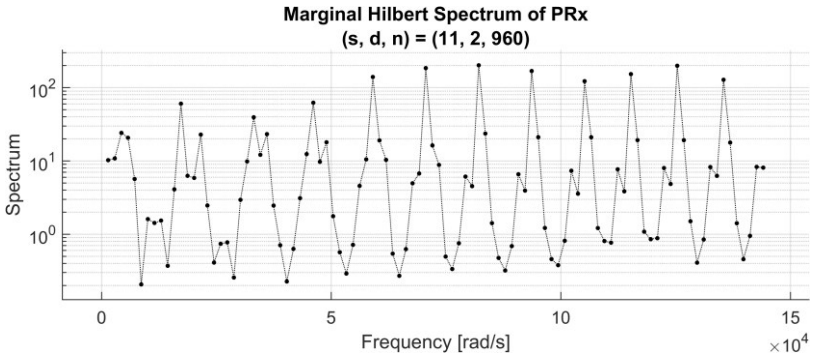

Figure V-18 Marginal Hilbert Spectrum of received power (n, d, s) = (960, 2, 11).

We applied the MHS to the received power signal to analyze its time-varying frequency characteristics more comprehensively (see Figure. V-18 and Figure. V-19).

By using the MHS, we were able to decompose the received power signal into its IMFs and then analyze the instantaneous frequencies of these components. The marginal spectrum, which is essentially the distribution of energy across frequencies over time, was obtained by integrating the instantaneous frequency across time. This allowed us to visualize the frequency content of the received power at every moment.

In practical terms, the MHS enabled us to track how the frequency of the received power signal fluctuated over time, revealing important insights into how the signal behaves in dynamic environments, such as during high-speed communications. This is particularly important for enhancing the THz communication networks, where the signal frequency can vary rapidly and unpredictably due to factors like interference, mobility, and environmental conditions.

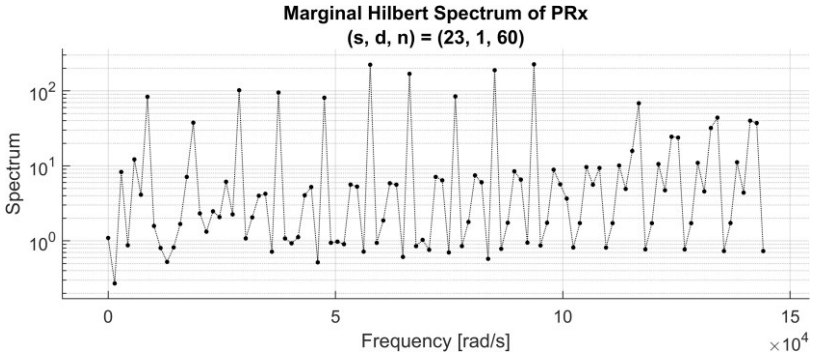

Figure V-19 Marginal Hilbert Spectrum of received power (n, d, s) = (60, 1, 23).

The MHS of the received power shows varying patterns depending on the scenario. These patterns reflect how the frequency components of the signal change over time. In some cases, the spectrum may appear stable, indicating consistent received power, while in others, it may fluctuate, pointing to factors like interference or environmental changes. These variations provide valuable insights into the system's behavior, helping to identify stable periods or potential issues like interference. By analyzing these patterns, we can better understand the performance of high-speed communication systems and make improvements for optimal operation.

Table V-1Used statistical methods.

Statistical Method	Explanation
Mean	Provides the average value of the data: $\mu = \frac{1}{N}\sum_{i=1}^{N} x_i$ N is the total number of data points. x_i are the individual data points.
Interquartile Range (IQR)	The IQR is the difference between the first quartile (25th percentile) and the third quartile (75th percentile): $IQR = Q_3 - Q_1$ Q_1 is the first quartile (25th percentile). Q_3 is the third quartile (75th percentile).
Variance	Variance measures the spread of the data around the mean. It is calculated as: $\sigma^2 = \frac{1}{N}\sum_{i=1}^{N}(x_i - \mu)^2$
Skewness	Skewness measures the asymmetry of the data distribution. $Skewness = \frac{1}{N}\sum_{i=1}^{N}(\frac{x_i - \mu}{\sigma})^3$

We decided to analyze the MHS spectrum using four statistical methods to gain a clearer understanding of the received power behavior.

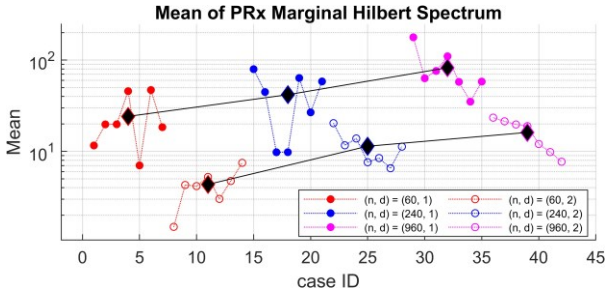

Figure V-20 Mean of received power marginal Hilbert spectrum vs. scenario case ID.

These methods allow us to summarize and interpret the different characteristics of the MHS in a more detailed and meaningful way. The chosen methods are described in Table V-1.

By applying these statistical methods, we gain a more comprehensive view of the MHS spectrum. This helps us better interpret the signal's dynamics and improve our understanding of the received power behavior in high-speed communication systems.

All four statistical methods (mean, IQR, variance, and skewness, see Figure. V-20, V-21, V-22, and V-23), have the following information: i) Colors red, blue, and magenta represent the number of MTs being 60, 240, and 960 respectively. ii) filled circles represent the centered topology, while the empty circles represent the uniform topology. iii) Each cluster has 7 circles, which conforms to the number of sector steps. vi) Diamonds are the mass point of the corresponding cluster.

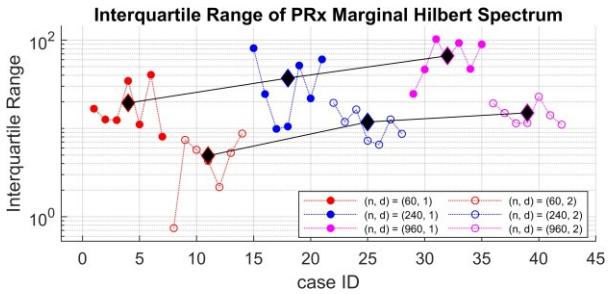

Figure V-21 Interquartile Range of received power marginal Hilbert spectrum vs. scenario case ID.

We consistently observed that the centered topology (d1) (where the MTs are located closer to the AP) exhibited higher clustering than the uniform topology across all three MT population cases. This behavior makes sense when we consider the dynamic nature of signal propagation systems in these topologies. In the centered topology, the MTs are positioned closer to the AP, which generally results in stronger received power and more consistent communication conditions. Proximity minimizes the effect of signal attenuation and interference, leading to more predictable and concentrated signal properties. The means are higher because the received power is stronger due to reduced path loss (see Figure. V-20). However, for uniform topology, the meaning is lower, causing the average received power to decrease with distance.

Moreover, IQR and variance are smaller for the centered topology, reflecting less variation in the received power because the MTs are similarly situated around the AP (see Figure. V-21, and Figure. V-22).

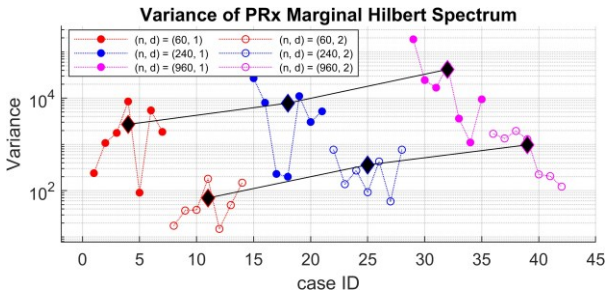

Figure V-22 Variance of received power marginal Hilbert spectrum vs. scenario case ID.

Based on the connection segments of the mass points of the clusters shown in Figure. V-20, V-21 and V-22, one can notice that for all means, IQR and variance of the MHS the higher the population density, the higher the mass point of the metric value. The distance between the two mass point trends is 50, which proves a 17 dB ratio between the variance of PRx MHS for centered and uniform topologies. This approximately exponential dependence property on the linear scale on the population density may be explained by the meaning of the MHS: the energy distribution of a received power signal across the frequency domain is larger for the higher number of MTs. The higher value-based time series have larger expected (mean), range, and variance values. The skewness indicates a more symmetrical distribution of the received power due to uniformity in the proximity of the AP (see Figure. V-23). This clustering behavior in the centered topology demonstrates the natural advantage of having MTs closer to the AP in terms of signal consistency and strength.

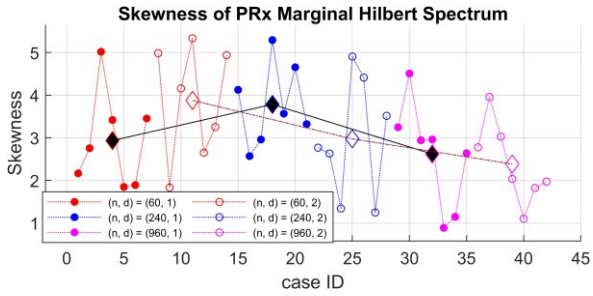

Figure V-23 Skewness of received power marginal Hilbert spectrum vs. scenario case ID.

The skewness behaves differently for the two topologies: the centered topology has a global maximum value of 240 MTs, while uniform topology has a continuous decreasing trend with the population density (see Figure. V-23). The MHS was key to

identifying the differences between the centered and uniform topologies. Through MHS, we observed the higher clustering of the centered topology and greater variability in the uniform topology.

MHS analysis proves how the energy is distributed across oscillatory modes of the received power by the MTs, thereby linking spectral content to temporal dynamics. The findings of this section reveals that high-fraquency components capture rapid fluctuations caused by the interference and fading, while low-frequency components reflect long-term variations associated with the AP periodic rotation. By comparing these distributions across scenarios, the analysis highlights differences in variability and stability providing direct understanding into the system's dynamic behavior.

Overall, the applied methods in this chapter give complementary views on the 6G network behavior. The Shannon entropy metrics (M and R) capture the stability and the fairness of the MTs subsystems. EMD/EEMD highlights temporal throughput variations, while the MHS extracts characteristic fluctuation patterns for scenario comparison. Together, these analyses link the studies parameters to concrete use cases such as protocol tuning, congestion detection, and deployment optimization, thus increasing the practical value of the study.

CHAPTER VI

AI INTEGRATION FOR 6G SYSTEMS OPTIMIZATION

Integrating AI into modern wireless technologies is highly recommended for enhancing network performance, where supervised and unsupervised ML can optimize various aspects. Hence, we applied different AI methods to different scenario cases for better analysis. By leveraging machine learning and data-driven approaches, we aim to gain deeper insights into network behavior, assess the effectiveness of entropy-based metrics, and identify potential strategies to enhance communication efficiency and reduce collision rate. It is important to mention that an increase in the number of MTs leads to a corresponding rise in computational overhead, therefore we vary the number of MTs in the following subsections based on the method employed to reduce computational demands. This variation allows us to assess the effects of MT scalability on overall system performance while optimizing resource utilization. This phenomenon is primarily attributed to the dependency of CPU instructions on the number of MTs. As the network scales and more MTs are introduced, we consider the number of MTs as a scaling parameter, which evaluates its impact on system performance. The processing requirements for managing communication and data transmission intensify, thereby escalating the overall processing demands on the system.

VI.1. Clustering-Based Analysis of Sector Efficiency in 6G Networks

Incorporating unsupervised machine learning into the ADAPT mechanism may enhance network efficiency in dynamic environments [72, 73]. By leveraging data-driven insights, unsupervised ML-based clustering can help identify underlying patterns in network traffic and MT behavior without labeling the data. These aspects motivate us to apply unsupervised ML on such complex data series to uncover hidden structures and correlations within the ADAPT protocol's communication patterns. The goal of applying clustering in this section is to group sector efficiency vectors into representative classes. This enables a deeper understanding of how the ADAPT mechanism behaves under varying conditions, ultimately supporting optimization of resource allocation and protocol adaptability. By doing so, we can enable the MAC system to self-tune its parameters in real-time, supporting more advanced techniques to address the challenges inherent in Terahertz communications. Studying the sector

behavior contributes to optimizing the ADAPT MAC mechanism and the THz radio channel. Within 50 simulation cases, having n ∈ {60, 120, 240, 480, 960}, d ∈{d1, d2} and $m \in \{0.1, 0.3, 0.5, 0.7, 0.9\}$, we calculated the sector efficiency considering both collisions and throughput. We define a sector efficiency vector that is calculated using both the collision rate and throughput of the MAC performance within a given sector, as shown in Figure. VI-1 and Figure. VI-2 for gaining more insight into the efficacy and effectiveness of sector vectors [J2, J4, C4].

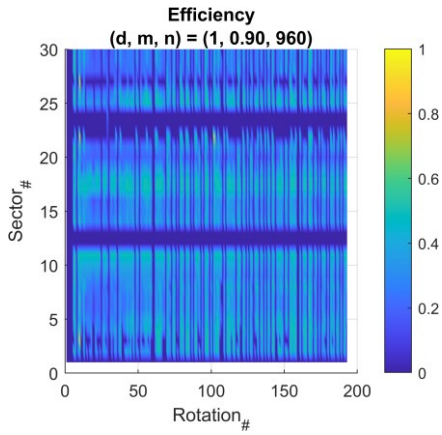

Figure VI-1 Sector efficiency vs. rotation ID.

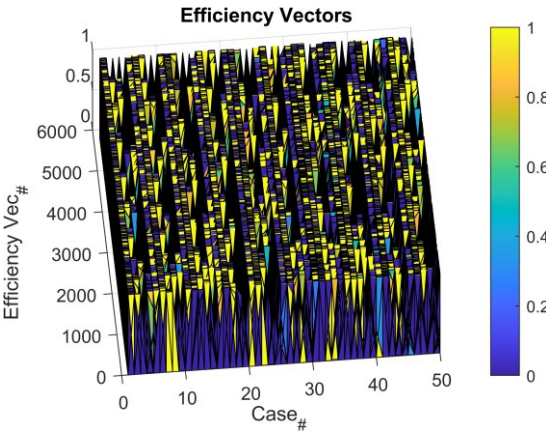

Figure VI-2 Efficiency vectors for all 50 simulation cases.

Among the machine learning types, we have unsupervised machine learning, where a given algorithm is trained on an unlabeled dataset, which can discover hidden patterns and the intrinsic structure of the trained data. Thus, we decided to use Density-Based Spatial clustering of applications with noise (DBScan) on the sector efficiency vectors for feature-based clusterization. DBScan clusters the dataset based on the density of data points without the interference of the noise. Mainly, DBScan is sensitive to two parameters: the radius that defines the distance between two points to be neighbors, and the minimum points required to form a dense region or a cluster.

Analyzing the sector efficiency vectors using DBScan shows the high influence of the mentioned DBScan parameters on the number of clusters and the number of outliers shown in Figure. VI-3 and Figure. VI-4, respectively. The results show the effectiveness of the unsupervised DBScan machine learning, underscoring how crucial parameter selection is for successful data clustering. As shown in Figure. VI-5, the

number of clusters strongly depends on the cluster radius, which requires a deep study and careful selection for accurate results.

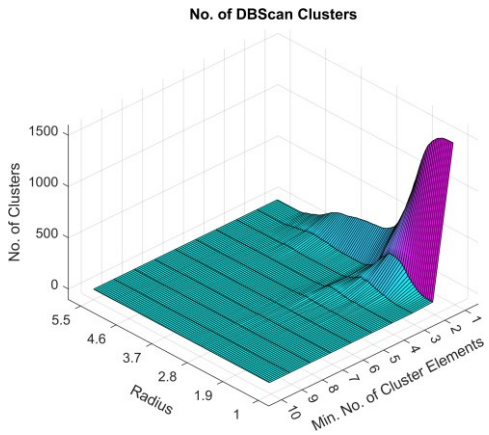

Figure VI-3 DBScan Clusters Number vs. Radius and Minimum Number of Cluster Elements.

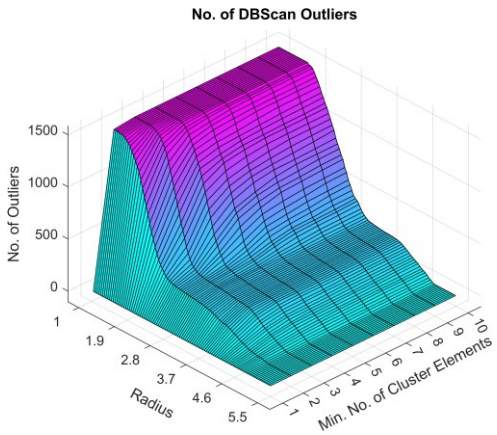

Figure VI-4 DBScan Outliers Number vs. Radius and Minimum Number of Cluster Elements.

Similarly shown in Figure. VI-6, where even the outliers got influenced, it is obvious that when selecting the minimum number of points equal to 1, the number of outliers will be 0. The reason after that is that every element becomes a cluster itself, and this is not logical; therefore this option must be excluded.

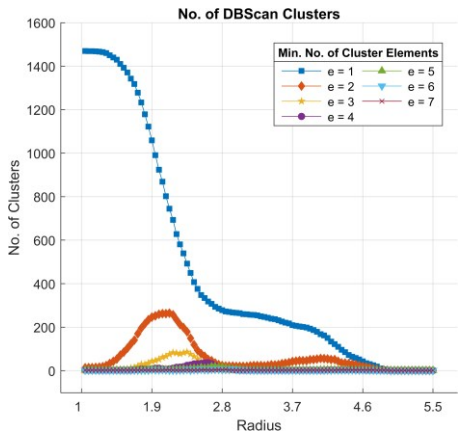

Figure VI-5 DBScan Clusters Number vs. Radius.

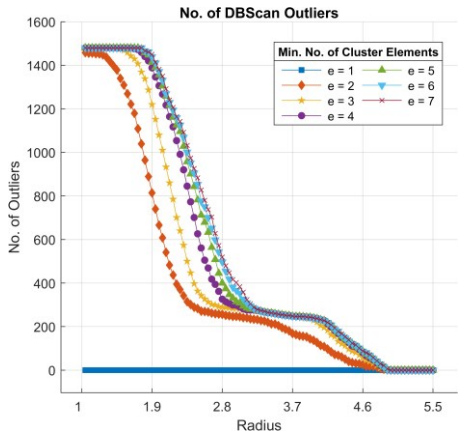

Figure VI-6 DBScan Outliers Number vs. Radius.

Moreover, the relation between increasing the cluster radius and its impact on the number of outliers is evident, where a clear reduction in both the number of clusters

and the presence of outliers occurs as the radius increases. This finding highlights the importance of balancing the cluster radius with the minimum number of elements required for best classification. For achieving accurate data clustering, adjusting these parameters is a necessity.

Hence, we explored how the number of outliers varies with changes in the minimum number of elements per cluster as presented in Figure. VI-7. The aim is to find the working point having the minimum number of outliers, As we exclude the number of elements being equal to 1 for the reason mentioned earlier, the working point is achieved by selecting 6 elements per cluster for sector efficiency vectors. Based on this, we define 7 different classes$(C_0, C_1, C_2, C_3, C_4, C_5, C_6)$ of the dataset, with outliers assigned to the class C_0. By doing so, the clustering process is enhanced offering valuable insights into the patterns of sector efficiency within the analyzed dataset.

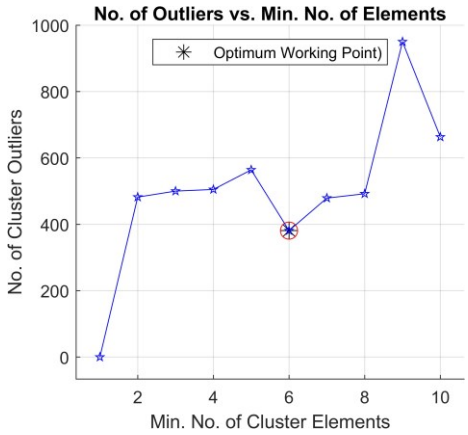

Figure VI-7 Dependence of Outliers Number on Minimum Number of Cluster Elements.

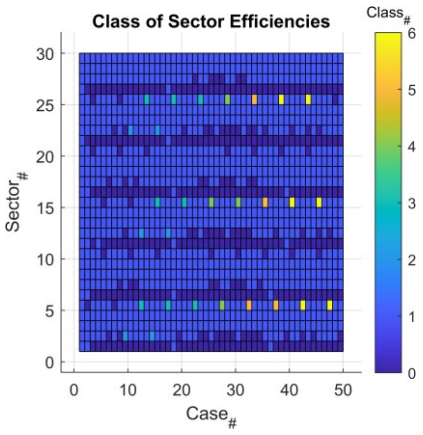

Figure VI-8 Classification of sector efficiency vectors at optimal working point.

The results of classifying the sector efficiency vectors using the working point are illustrated in Figure. VI-8, Given the substantial number of outliers which represents 25.5% of the data (383 out of 1500 elements) revealed with dark blue rectangles in class C_0. Meanwhile, It is intriguing that sector efficiency vectors having the IDs 5, 15, and 25 are enrolled within the clusters C_4, C_5, and C_6. This criterion invites further investigation to understand why these sectors are enrolled in these classes in this

manner, which could reveal unique characteristics or patterns specific to these cases and sectors.

The clustering results reveal distinct categories of sector behavior. High-efficiency clusters correspond to a sector with consistently high throughput with low collision rates, while lower-efficiency clusters represent a sector where performance degrades due to congestion. The computed outliers highlight the extreme or irregular behaviors. This clustering highlights which sectors contribute most to network stability and which require further adaptation. Thereby guiding parameter tuning in the ADAPT MAC mechanism. We could say that DBScan suffers with data sets of varying densities and high dimensionality, making it sensitive to parameter selection and less effective for complex or large datasets. Future enhancement could include employing adaptive clustering algorithms that dynamically adjust based on real-time data variability or incorporating anomaly detection methods like: isolating forest, local outlier factor density-based method, and more, for handling and interpreting the outliers' meaning, thereby improving the precision and reliability of the clustering process.

VI.2. Wavelet-based Feature Extraction for Throughput Prediction

The goal of this subchapter is to apply feature extraction method in combination with supervised neural networks to predict throughput in 6G scenarios. Wavelet transform method is for cases when shifting events in time does not affect the result which called invariance to translation, and also stability to deformation. Moreover, the wavelet transform offers localization in both time and scale, unlike the traditional focus on time and frequency. The wavelet transform relies on the convolution operation, and this let us convert certain signals into a more refined form where features become more prominent, therefore using such a method for feature extraction helps in simplifying the task for the supervised neural networks. This method enhances the clarity of the signal, making it easier for the network to recognize and process key patterns.

The wavelet transform WT of the signal $x(t)$ is a mathematical tool well-known in the signal processing field, signal compression, and time-frequency analysis. Unlike

the Fourier transform that analyses signals using sinusoidal functions, the wavelet transform uses a mother wavelet denoted as $\Psi(t)$, being an $L^2(\mathbb{R})$ function, as far as:

$$\int_{-\infty}^{\infty} |\Psi(t)|^2 dt < \infty \tag{32}$$

Wavelets $\psi_{a,b}(t)$ are specific subsets of the mother wavelet represented in equation (33):

$$\psi_{a,b}(t) = \frac{1}{\sqrt{a}} \Psi\left(\frac{t-b}{a}\right) \tag{33}$$

where pairs (a, b) are points in the half plane $\mathbb{R}_+ \times \mathbb{R}$. Parameter a and b are the scale and time shift, respectively. $\psi(t)$ in equation (33) satisfy the condition of mean zero and square norm one as represented in the following formulae:

$$\int_{-\infty}^{\infty} \psi(t) dt = 0 \tag{34}$$

$$\int_{-\infty}^{\infty} |\psi(t)|^2 dt = 1 \tag{35}$$

The signal $x(t)$ has a projection onto the subspace of scale a conform to the next formula:

$$x_a(t) = \int_{\mathbb{R}} WT_{\Psi}\{x\}(a, b) \cdot \psi_{a,b}(t) db \tag{36}$$

Where the wavelet transform of the signal $x(t)$ is the following:

$$WT_{\Psi}\{x\}(a, b) = \int_{\mathbb{R}} x(t) \psi_{a,b}(t) dt \tag{37}$$

The wavelet coefficients are $c_{jk} = WT_{\Psi}\{x\}(a, b)$, where $a = 2^{-j}, b = k2^{-j}$ are the binary dilation and binary position, respectively. Reshape of the c_{jk} into a single vector is considered a feature vector, which is a compression of the (a, b) points set.

There are a lot of existing transformation methods that can be used for extracting features, well-known ones are the Fourier transform and Short-Time Fourier Transform (STFT), so why are we using the wavelet transform? One has to note that the Fourier transform provides a global frequency representation but lacks temporal resolution, while STFT offers time-localized frequency information but struggles with the trade-off between time and frequency resolution. Conversely, wavelet transform effectively captures both transient and persistent features across varying time scales, making it superior for analyzing non-stationary signals and providing a nuanced representation of complex data.

As mentioned earlier, the fractal property motivated us to study the pattern of the transmission distance of the AP-MT pairs. For the scenario [J2, C1], we have 14 different simulation cases where we considered two parameters: the population number $n = 15, 30, 60, 120, 240, 480, 960$, and two topology types, the centered topology d1 and the uniform distribution topology d2. From the simulated cases, we chose the distances as an input to the wavelet transform for feature extraction. These extracted feature vectors are then used as an input to the RNN, which learn temporal dependencies in the data. We randomly select 300 compacted sequences from the overall distances data series, creating so-called feature vectors, represented as follows:

$$\delta^i = \left(\delta_1^i, \delta_2^i, \dots, \delta_{300}^i\right), i = 1, 2, \dots, 14 \quad (38)$$

Every sequence vector $\delta_j^i \in \mathbb{R}^{2000}, j = 1, \dots, 300$ has 2000 serial elements, where the vectors have been classified and mapped based on Table. VI-1 having in total 5 different classes $(C_1, \dots, C_5)$, the classes are carefully chosen based on the mobile terminals' densities.

Table VI-1Class mapping of the distance sequence.

Distribution (d)	**Number of MTs (n)**						
	15	*30*	*60*	*120*	*240*	*480*	*960*
1	C_1	C_1	C_1	C_2	C_3	C_4	C_5
2	C_1	C_1	C_1	C_2	C_3	C_4	C_5
Collision	0	0	~ 0	> 0	> 0	> 0	>> 0

For each vector δ_j^i, the applied wavelet transform creates a so-called feature vector $f_j^i \in \mathbb{R}^{238}$ having 238 instead of 2000, containing a more compressed manner of the feature characteristics.

Table VI-2 RNN neural network applied parameters.

Property	**Value**	**Property**	**Value**
SquaredGradientDecayFactor	0.99	Solver	ADAM
GradientDecayFactor	0.90	Mini Batch Size	2100
InitialLearnRate	0.02	MaxEpochs	100
No. Hidden units at L2	100	No. Classes at L3	100
GradientThreshold	1	No. Classes at L4	5

We taught the LSTM by selecting 50% randomly the distance feature vectors, using the third quarter for validation during the teaching, while the remaining part we used for testing the taught results. Table. VI-2 shows the used parameters for the LSTM neural network.

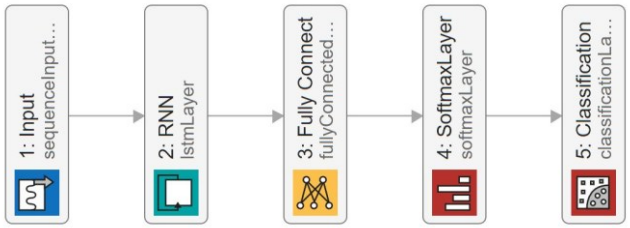

FigureVI-9 Recurrent neural network structure.

Since the features are already extracted using the wavelet transform, The architecture of the RNN network remains straightforward, as shown in the Figure. VI-9. The streamlined design facilitates efficient processing without the need for complex modifications or extra layers.

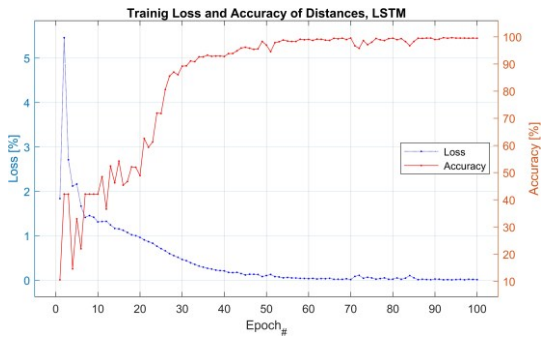

Figure VI-10 LSTM neural network learning and classification results.

Figure VI-11 LSTM confusion matrix.

Hence, the learning and classification results of the RNN types: LSTM, BiLSTM, and Gated Recurrent Units (GRU) neural network are shown in the next figures, notably the plot emphasizes the exponential speed at which convergence occurs and

the corresponding exponential decline in loss showcasing the efficiency of the learning method.

Figure VI-12 BiLSTM neural network learning and classification results.

Figure VI-13 BiLSTM confusion matrix.

The training of the LSTM RNN model shows a rapid increase in accuracy, demonstrating how effectively the extracted features were identified (Figure. VI-10).

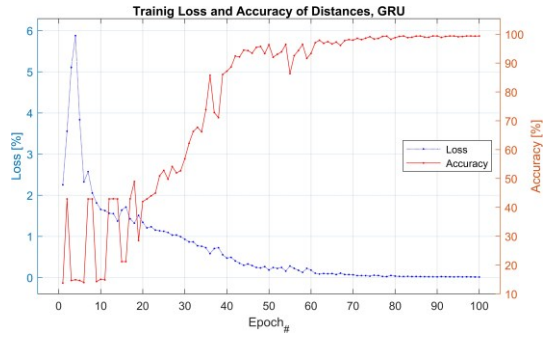

Figure VI-14 GRU neural network learning.

Figure VI-15 GRU confusion matrix.

This quick improvement suggests that the model quickly learned to recognize patterns in the data, making the training process efficient. The confusion matrix further illustrates the classification accuracy with 99.4% testing accuracy, where most of the classifications were correct, with minimal confusion observed. A slight confusion was noted between some classes (Figure. VI-11).

Moving to the BiLSTM model, the accuracy was good, but it faced some difficulties in learning the extracted features at the beginning, particularly until epoch 60.

During this initial phase, the model struggled to effectively capture the nuances of the data. However, after epoch 60, the performance significantly improved, and the learning accuracy surged to 99% (Figure. VI-12). This indicated that, despite early challenges, the model eventually adapted well to the features.

The confusion matrix for the BiLSTM (Figure. VI-13) also reflected strong performance, showing an overall testing accuracy of 94.4%. However, similar to the LSTM model, there was some confusion between certain classes, suggesting that while the BiLSTM achieved high accuracy, there remained small overlaps between specific categories that could be further refined. The learning accuracy for the GRU model followed a similar pattern to the BiLSTM, initially struggling but improving over time. Starting from epoch 70, accuracy increased to 99% (Figure. VI-14). The confusion matrix showed the best testing accuracy of 99.5% with only slight confusion between class C_4 and C_5 (Figure. VI-15).

Each model, when combined with wavelet transform for feature extraction, showed strong performance. The GRU model, for instance, achieved 99.5% accuracy and completed training and testing in a remarkably short time, highlighting its efficiency and ability to process complex data quickly. Similarly, the LSTM and BiLSTM models showed excellent accuracy, though with slight differences in training behavior. While all models demonstrated robustness in handling the given dataset, the wavelet transform required substantial computational resources. Additionally, class imbalance can affect model accuracy, especially for underrepresented classes. Although the GRU, LSTM, and BiLSTM models performed strongly, their complexity may not always be justified in scenarios where the data does not have sequential dependencies. In such cases, simpler models could offer comparable performance with lower computational cost.

VI.3. Transfer Learning for Collision Analysis and Performance Quantification

In this part, transfer learning is introduced to enhance collision analysis and performance quantification in dense 6G scenarios. By re-teaching knowledge from pre-trained RNN layers, the approach reduces training time while preserving or improving the accuracy of sector collision classification. This method helps in enabling the identification of optimal NN configuration for handling congestion, supporting more efficient resource allocation under high-load conditions.

Multi-layer transfer learning leverages pre-trained models to enhance the performance of complex systems by transferring knowledge from one domain to another [74, 75, 76]. By adding the rotation step $s = \{1,7,11,13,17,19,23,29\}$ [J2, C2], we took the most congested case having 960 MTs in 2 different topology types, d1 and d2 having all together 16 cases.

We considered having four different classes of sector collisions as an input for the different types of neural network models, in correlation with the step s. Every two twin pairs (based on the twin relation explained earlier) belong to the same class (see Table. VI-3). For evaluating the transfer learning efficiency of the ADAPT MAC mechanism on collision data series, we used three RNN types (LSTM, BiLSTM, and GRU). Each of these RNN types consists of one or more layers positioned directly after the input layer, enabling the network to capture sequential patterns in the data effectively. We added SoftMax to finalize the output of the network, followed by Classification layers, which translate the learned representations from the RNN layers into actionable class predictions. The applied configuration allows for robust handling of complex time series. The networks classify the inputs into collision categories defined in Table. VI-3, providing a clear interpretation of the network state.

Table VI-3 Class sector collisions.

Class ID	Step Size, s	Sectors	Distribution	MT Number
1	1, 29	n = 30	d1, d2	N = 960
2	7, 23	n = 30	d1, d2	N = 960
3	11, 19	n = 30	d1, d2	N = 960
4	13, 17	n = 30	d1, d2	N = 960

By taking advantage of the taught layers, we envisioned a novel approach to constructing both homogeneous and heterogeneous multilayer neural networks through the transfer learning process. Pre-trained RNN layers from initial training on a subset of collision scenarios are reused and fine-tuned for new network configurations. This innovation strategy not only broadens the scope of our neural network architecture but also enhances its adaptability to diverse datasets.

Table VI-4 Neural network types.

NN Code	Transf. Learn.	Homogeneous	Taught Layers	Untaught Layers	Max. Epochs
U1	No	Yes	0	1	150
U2	No	No	0	2	150
T0	Yes	Yes	k = 1, …, 5	0	150+200·k
T1	Yes	No	k = 1, …, 4	1	150+200·k
T4	No	Yes	0	k = 1, …, 5	150+200·k

To evaluate the effectiveness and goodness of the learning approach, we developed a comprehensive metric that quantifies the quality of the learning outcomes. The different types of RNNs employed in this endeavor are detailed in the Table. VI-4. In addition, ‘U’ and ‘T’ are Untaught and Taught RNN types, respectively; the value after ‘U’ denotes the number of the untaught layers, and the value after the character ‘T’ states the number of RNN layers. The last column represents maximum epochs, which increase with the increase of RNN layers.

After the training phase, we visualized the test accuracy by plotting the performance of both untaught single-layer and double-layer configurations of the different RNN types, coded in the Table. VI-5 as ‘U1’ and ‘U2’, respectively. Notably, one untaught layer of BiLSTM outperformed the other RNN types, achieving an impressive accuracy of 90.03%, In contrast, the LSTM model recorded the lowest performance with a learning accuracy of 85.04% (see Figure. VI-16). Moreover, adding another untaught layer to the neural network gave different results (see Figure. VI-17). Here, L1 and L2 refer to the first and second untaught layers of the RNN architecture. It is noteworthy that when LSTM is designated as L1, the testing accuracy is significantly influenced by the type of L2. In contrast, the type of L2 after BiLSTM

(as L1) exhibits minimal impact on the results, while after GRU (as L1), the type of the untaught RNN layer (L2) influences both accuracy and testing outcomes.

For quantifying the goodness of the used RNN layers and evaluating the internal performance of the chosen layers, we propose a metric to weigh the overall effectiveness of the method used. To the best of our knowledge, no similar metric exists in scientific literature to compare the performances.

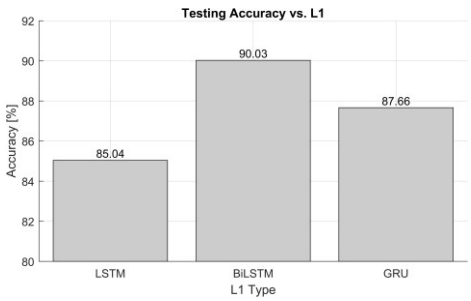

Figure VI-16 Test accuracy of sector collisions for different U1 RNN types

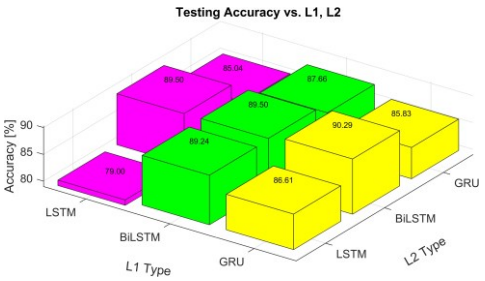

Figure VI-17 Test accuracy of sector collisions for different U2 RNN type pairs.

We decided to have a certain threshold constant $a = 0.90$ for validation purposes, which serves to calibrate our calculations and provide a consistent benchmark for evaluating the performance of the RNN layers utilized in our study, we calculate the Accuracy-to-Tima Ratio (ATR):

$$\mathrm{ATR}_{\mathrm{valid}}(a) = \frac{\mathrm{Acc}_{\mathrm{valid}}(a)}{\mathrm{Learn\ Time}(a)}\ [\mathrm{s}^{-1}] \tag{39}$$

$$\mathrm{ATR}_{\mathrm{test}} = \frac{\mathrm{Acc}_{\mathrm{test}}}{\mathrm{Learn\ Time}}\ [\mathrm{s}^{-1}] \tag{40}$$

We have $Acc_{valid}(a) = a$ and $Learn\ Time(a)$ represents the validation accuracy within a threshold a and learning time for the validation accuracy a, respectively. While Acc_{test} representing the testing accuracy after $Learn\ Time$ duration. The proposed metric so-called Weighted Accuracy-to-Time Ratio (WATR) is the weighted sum of the two calculated ATRs with a weight α:

$$\mathrm{WATR} = \alpha \cdot \mathrm{ATR}_{\mathrm{valid}} + (1 - \alpha) \cdot \mathrm{ATR}_{\mathrm{test}}\ [\mathrm{s}^{-1}] \tag{41}$$

The weight α It is an objective that reflects the relative importance of validation versus testing performance.

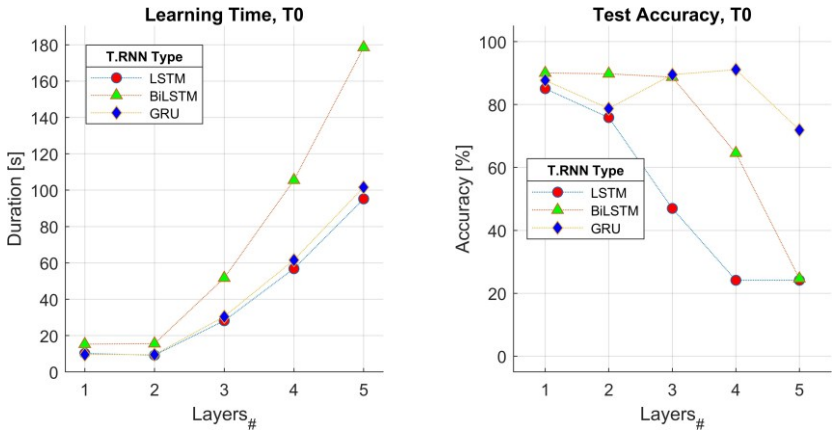

Figure VI-18 Learning time (Left) and test accuracy (Right) of sector collisions for different T0 RNN types.

Given the significant impact of these parameters, we define α as the ratio of the $\mathrm{ATR}_{\mathrm{valid}}$ and $\mathrm{ATR}_{\mathrm{test}}$ values, calculated using the following expression:

$$\alpha = \frac{\max(\mathrm{ATR}_{\mathrm{test}})}{\max(\mathrm{ATR}_{\mathrm{valid}})} \tag{42}$$

By doing so, the high value of WATR indicates the high performance of the neural network with good testing accuracy and fast learning time.

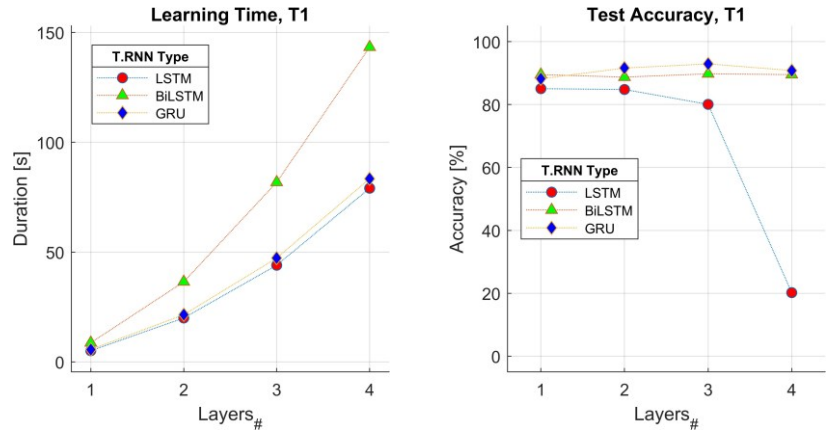

Figure VI-19 Learning time (Left) and test accuracy (Right) of sector collisions for different T1 RNN types.

This is precisely the outcome we aim to quantify, as it reflects the effectiveness, goodness, and responsiveness of our model in practical applications. To evaluate the

performance and effectiveness of the taught and untaught layers being homogeneous and heterogeneous, the following figures plot the performance of T0, T1, and T4.

One can notice, that in the case of the homogenous T0, increasing in the RNN layer despite the NN type, the learning time increases (see Figure. VI-18). However, the testing accuracy decreases with the increasing of the taught layers, especially LSTM and BiLSTM, however, GRU performed better having 4 layers.

A comparable pattern is noticeable for the learning time in the case of heterogeneous T1 as we saw in T0 (see Figure. VI-19) with a 30% reduced duration. Increasing the taught layers shows negligible accuracy impact in the case of BiLSTM and GRU, while the accuracy of LSTM becomes less as we increase the layers.

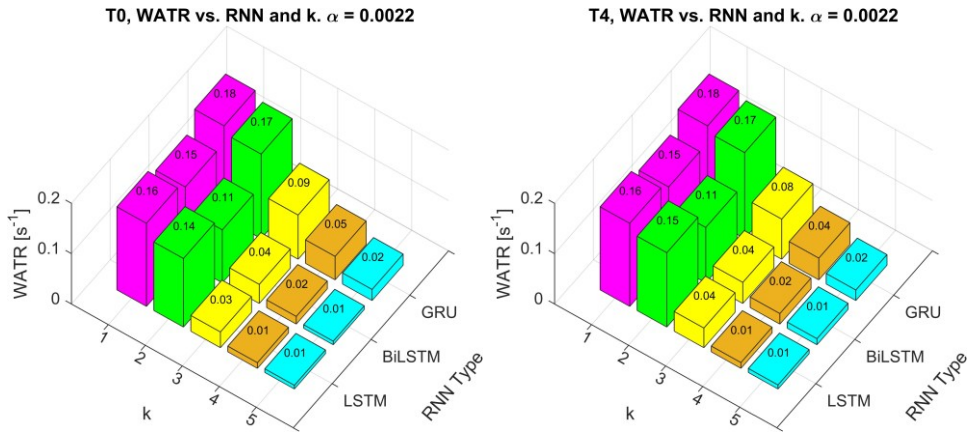

Figure VI-20 WATR for T0 (Left) and T4 (Right) homogeneous RNN types.

We evaluate the performance of both T0 and T4 by calculating the WATR metric, and the results are shown in the Figure. VI-20. For both cases, GRU performed better than the other NN types with a slight difference between having one and two layers, however, since the learning time increases with more layers', higher testing accuracy is indicated for $k = 2$. Moreover, the goodness metric for U2 NN demonstrates the best performance when GRU layers are used, the optimal configuration is achieved when both layers are GRU having WATR = 0.11 s^{-1} (shown in Figure. VI-21 left). For heterogeneous T1 NN, as the number of taught layers increases, the WATR value and the goodness metric value decrease (shown in Figure. VI-21 right). In all, this study revealed that increasing the number of RNN layers can lead to longer learning time.

The type of RNN significantly influences testing accuracy and WATR performance metrics. Notably, GRU outperformed other configurations, demonstrating superior efficiency and accuracy in both homogeneous and heterogeneous setups.

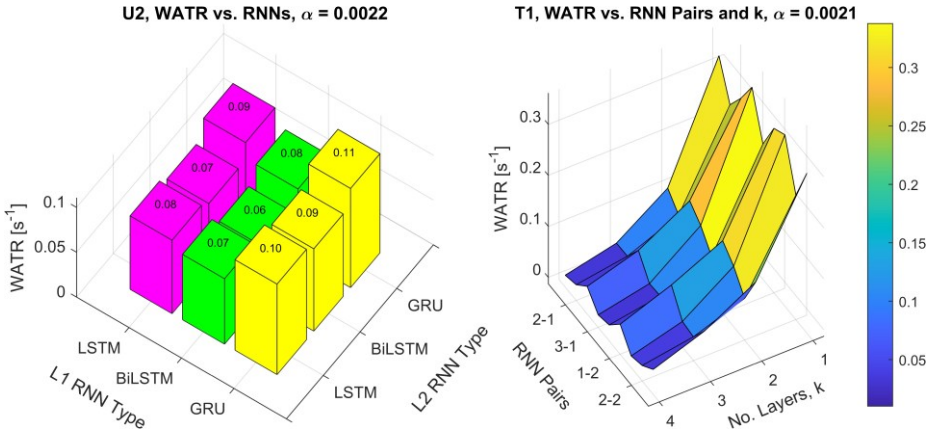

Figure VI-21 WATR for U2 (Left) and T1 (Right) heterogeneous RNN types.

The findings are particularly beneficial for the ADAPT mechanism and for future 6G applications, as they highlight optimal neural network configurations for effectively managing complex data series. Further analysis is planned to assess the impact of the weight α on the optimal WATR metric value, this investigation helps to refine our understanding of how the weight α influences the overall efficiency of the suggested neural network model.

VI.4. Generative Models for synthetic Data Augmentation in 6G Networks

This section examines how generative models, particularly Generative Adversarial Networks (GANs) can support the development of 6G networks by producing synthetic data that mirrors the complexity of real-world conditions. Generative AI has gained prominence for its capability in creating realistic synthetic data and models by training neural networks in a competitive setup. In the next cellular networks, generative AI promises to generate more realistic a significant synthetic network data and simulate complex scenarios. Generating realistic synthetic data is widely used for training machine learning models, where large, labeled data sets are essential but hard to obtain due to various limitations [77]. And because 6G is still now

in the theoretical and simulation phase, synthetic data may provide an essential resource for testing and developing models under realistic conditions without needing physical infrastructure. Due to the complexity of the ADAPT system, simulating for just $10\,ms$ incurs a significant computational load, especially for larger population densities. This short simulation period is not enough to capture the full system behavior, especially under varied network loads. To address this, we aim to analyze whether GAN methods can generate high-fidelity synthetic data that accurately represents the complex behavior within the ADAPT system. Evaluating the performance of these applied GAN methods involve using some similarity metrics to determine the performance of the generated synthetic data compared to the real one. This helps us to improve our understanding of the methods used and enable enhancements in efficiency and adaptability.

Generative AI uses various models and techniques for generating text, images, audio, and other types of data to create a new dataset that resembles existing patterns. GAN AI comprises two main neural networks: the generator and the discriminator, each has a different and important role in generating similar data. The generator neural network generates data from random noise, while the discriminator aims to differentiate between genuine data from the original dataset and the synthetic data generated by the generator. This aspect is represented in the Figure. VI-22.

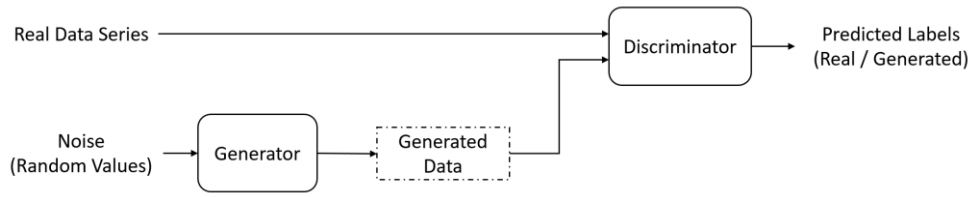

Figure VI-22 Architecture of the GAN system.

GAN has transformed the field of data generation and augmentation. Integration of this approach with the 6G wireless networks could significantly improve the performance of data augmentation, making it more representative of the real world [78]. We choose to use GAN and 4 from its method types (Adversarial Autoencoder (AAE), Deep Convolutional GAN (DCGAN), Least Squares GAN (LSGAN), and Wasserstein GAN (WGAN)) explained in the Table. VI-5 to generate synthetic data

for the Shannon entropy metrics M and R, to see the behavior of these types, and compare between [J2, C6, C7]. The GAN is trained on historical network metrics and generates synthetic sequences representing potential network states. By generating diverse entropy profiles, the GAN can simulate unseen network configurations while ensuring privacy, as no user-identifiable data is included and the generated metrics cannot be linked back to individual users.

Table VI-5 List of GAN methods.

Generative AI method	**Internal Layers**
1. AAE	**Encoder:** convolution layers/dense layers, batch normalization, and activation functions (ReLU). **Decoder:** transposed convolution layers/dense layers to reconstruct the input data. **Discriminator:** convolution/dense layers.
2. DCGAN	**Generator:** Transposed convolution layers, batch normalization, and ReLU activations **Discriminator:** Convolution layers, batch normalization, and Leaky ReLU activations.
3. GAN	**Generator:** fully connected layers, transposed convolution layers **Discriminator:** convolution layers and dense layers to classify real or fake.
4. LSGAN	**Generator:** Dense layer, transposed convolution layers, batch normalization, and ReLU activation. **Discriminator:** Convolution layers, Leaky ReLU, and dense layers.
5. WGAN	**Generator:** Dense layer, batch normalization, ReLU activation, and transposed convolutional layer with Tanh activation. **Discriminator:** Convolutional layers, leaky ReLU activation, and dense layers.

We decided to start with these well-known GAN methods to see their performance on our datasets and decide how to improve the existing algorithms based on the quality of the results obtained. With every GAN method, we generate twenty synthetic pairs M and R, having a total of 1400 per GAN method (having 20 from $n \in \mathrm{V}$, where set V is the number of MTs, $n \in \{15, 30, 60, 120, 240, 480, 960\}$, $d \in \{\mathrm{d1}, \mathrm{d2}\}$ and the overlapping ratio $m \in \{0.1, 0.3, 0.5, 0.7, 0.9\}$).

However, an important consideration is assessing the degree of similarity between the original par {M, R} and the generated one using GAN methods. To achieve this,

different similarity metrics may be employed to quantify the effectiveness of the GAN type used. This leads us to select six well-known metrics to gauge how closely the generated pair {M, R} matches the original pair of data sets, which can provide insights into the reliability of the outputs.

Table VI-6 List of Similarity Metrics.

Metric	Formula
CORR	$CORR(x,y) = \frac{\sum_{i=1}^{n}(x[i] - \bar{x})(y[i] - \bar{y})}{\sqrt{\sum_{i=1}^{n}(x[i] - \bar{x})^2 \sum_{i=1}^{n}(y[i] - \bar{y})^2}}$
COS	$COSI(x,y) = \frac{\sum_{i=1}^{n} x[i]y[i]}{\sqrt{(\sum_{i=1}^{n} x[i]^2)(\sum_{i=1}^{n} y[i]^2)}}$
DTW	$D[i,j] = (x_i - y_j)^2 + \min(D[i-1,j], D[i,j-1], D[i-1,j-1])$, $D[1,1] = (x_1 - y_1)^2$ $DTW(x,y) = D[n_x, n_y]$ Where $n_x = len(x) - 1$, and $n_y = len(y) - 1$.
FID	$COV(x), COV(y)$ *% Covariance of x and y* $FID(x,y) = (\bar{x} - \bar{y})^2 + Trace\left(\left(\sqrt{COV(x)} - \sqrt{COV(y)}\right)^2\right)$
PSNR	$MSE(x,y) = \frac{1}{n}\sum_{i=1}^{n}(x[i] - y[i])^2$ *% Mean Squared Error* $\max(x)$ *% Maximum of x* $PSNR(x,y) = 20log_{10}(\max(x)) - 10log_{10}(MSE(x,y))$
RMSE	$RMSE(x,y) = \sqrt{\frac{1}{n}\sum_{i=1}^{n}(x[i] - y[i])^2}$

The chosen similarity metrics for this evaluation are shown in the Table. VI-6, includes: Correlation similarity, Cosine similarity, Dynamic Time Warping (DTW), Fréchet Inception Distance (FID), Peak Signal-to-Noise Ratio (PSNR), and RMSE. These similarity methods have proven its usability as it was mentioned in the studies referenced in [79, 80, 81, 82]. Therefore, we got inspired to evaluate the GAN methods' similarity using it.

We analyze the evaluations of the generated Shannon entropy metrics {M, R} through various visual representations, including scatter plots and 3D histograms. The

following discussion focuses on interpreting the results and their significance for future research and applications.

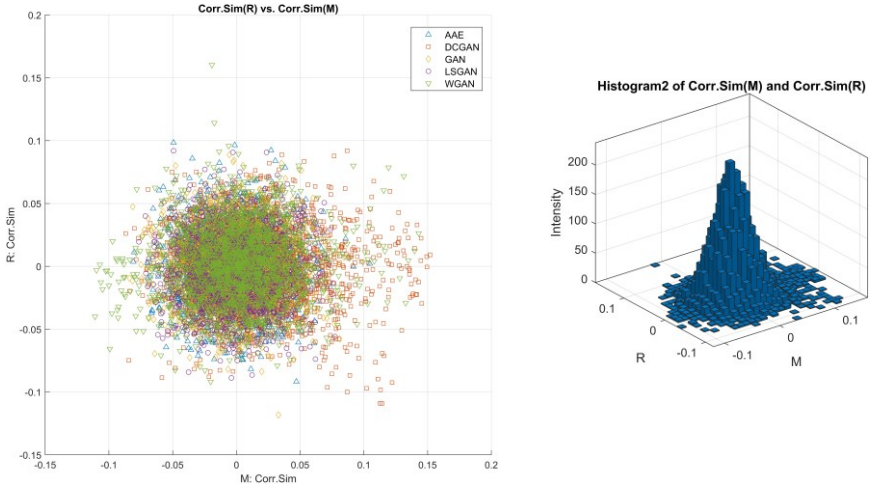

Figure VI-23 Correlation similarity, Scatter plot (Left), and 3D histogram (Right).

The correlation similarity between the original Shannon entropy metric pair and the generated ones using all the GAN methods shows no similarity between (concentrated around 0), meaning zero correlation in between and this is seen in the Figure. VI-23 (Left).

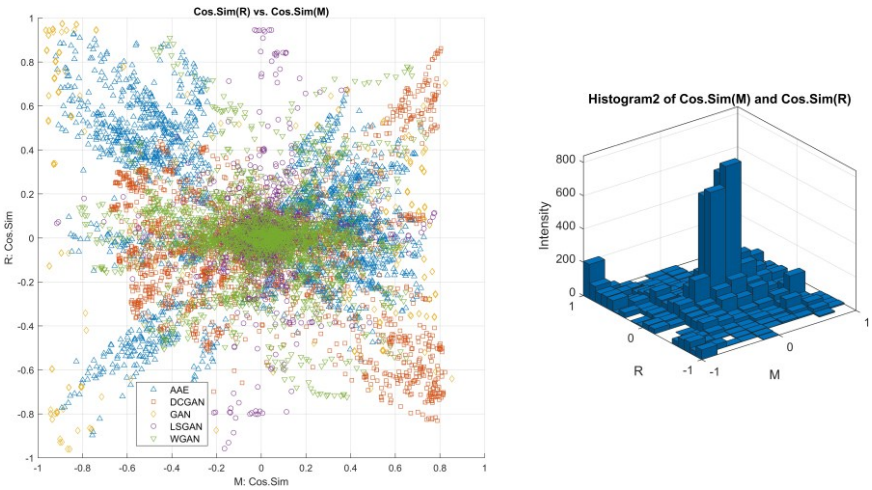

Figure VI-24 Cosine similarity, scatter plot (Left) and 3D histogram (Right).

The 3D histogram shows the high concentration of the boxes in the center of Figure. VI-23 (Right). This finding could present the limitation of correlation

similarity in detecting the similarity level between the synthetic and real data. Correlation metric only captures linear relationships and may miss non-linear dependencies, which are important in understanding complex data behavior. One must note that the correlation metric is sensitive to outliers that can destroy the results, leading to an incomplete representation of the similarity between the original and generated datasets.

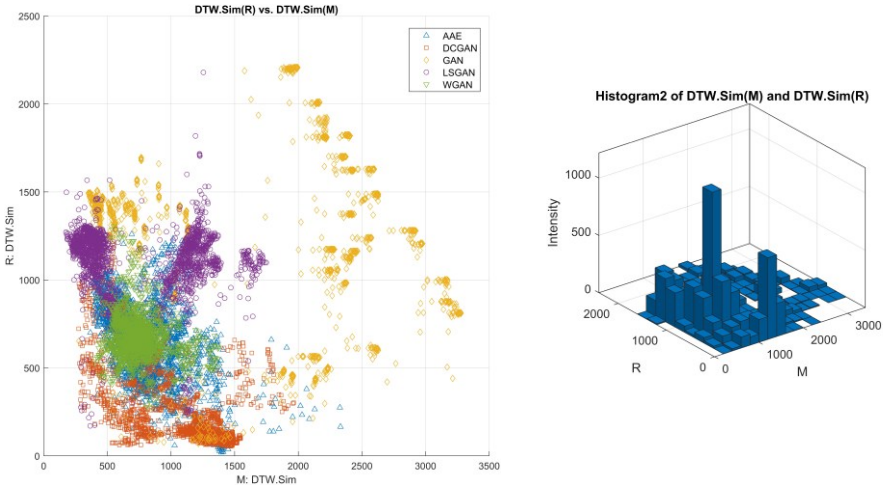

Figure VI-25 DTW, scatter plot (Left) and 3D histogram (Right).

Evaluating the similarity using cosine shows dispersed dots ranging from -1 to 1, cosine being -1 means that the data sets are opposed, while cosine 0 indicates that the vectors are orthogonal to each other and not similar and cosine 1 illustrates that the generated synthetic data are identical with the real data set (Figure. VI-45 (Left)). While the 3D histogram shows the dense boxes around 0 cosine (Figure. VI-45 (Right)). This diversity could provide a more sophisticated perspective on how the vectors relate to one another. The cosine similarity metric focuses on the orientation of the vectors and ignores their magnitudes. Therefore, two datasets with similar directions but differing scales could result in a high cosine similarity score. This limitation masks the essential differences in their distribution and overall characteristics.

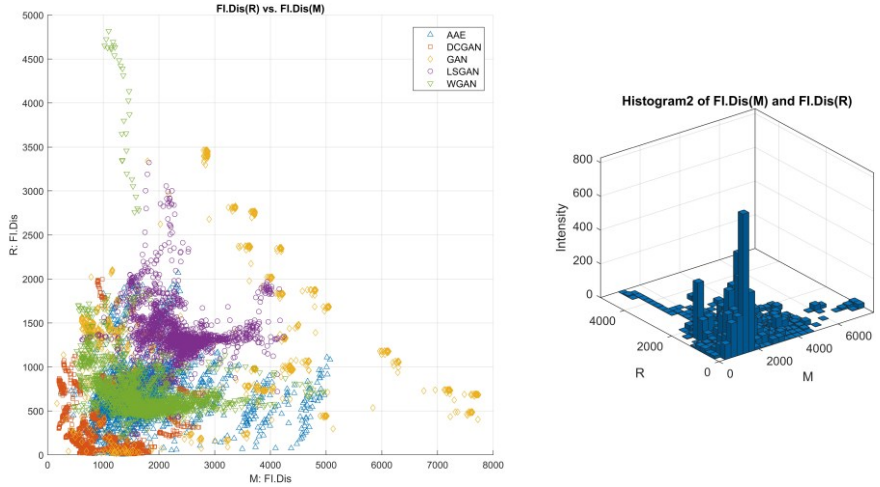

Figure VI-26 FID, scatter plot (Left) and 3D histogram (Right).

Dynamic time warping illustrates how all 5 GAN methods generate different data sets from a similar point of view with different intensities (see Figure. VI-25 (Right)).

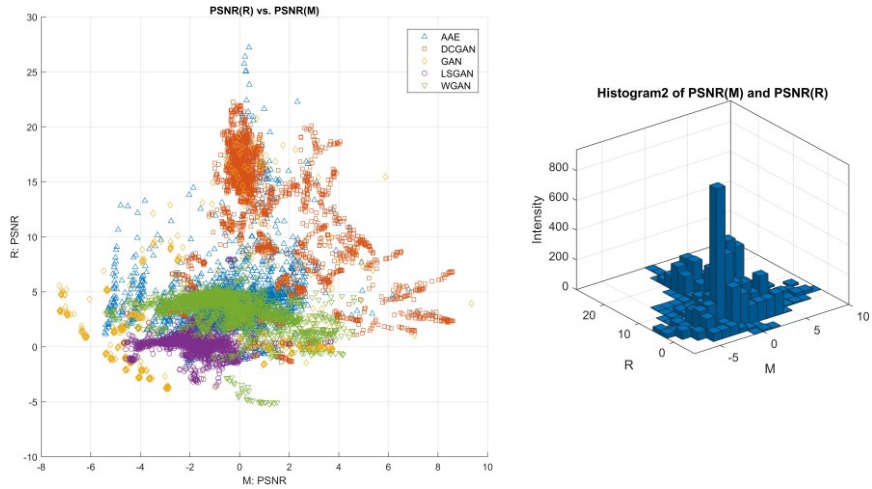

Figure VI-27 PSNR, scatter plot (Left) and 3D histogram (Right).

Figure. VI-25 (left) shows that the yellow diamonds (GAN) dispersed far from each other are wrong, meanwhile, the red squares (DCGAN) performed better than the others. The good performance of the DCGAN, indicated by its closer clustering, may imply that it captures the underlying structure of the data more effectively compared to other GAN methods. DCGAN proves its high performance with Fréchet Inception distance as well, having lower values. This finding suggests that DCGAN excels in

generating high-fidelity synthetic data. Conversely, the traditional GAN method has a bad generation with high FID values (see Figure. VI-26 (Left)).

The intensive boxes in the lower corner represent the rest of the GAN types: AAE, LSGAN, and WGAN, where they show comparable performances (Figure. VI-26 (Right)), which indicates that they might generate more realistic synthetic data than the traditional GAN but still not reach the performance level of DCGAN. Furthermore, we can say that the FID metric could capture the similarity level of the synthetic data and could cluster the applied GAN methods based on their performance. One has to notice, a high PSNR indicates the high performance of the used method. Hence, the GAN method clustered lower than the rest with poor quality, DCGAN shows the best performance, approximately 20 for the metric R and around 8 for the metric M, producing a high-quality of generated dataset (Figure. VI-27(Left)).

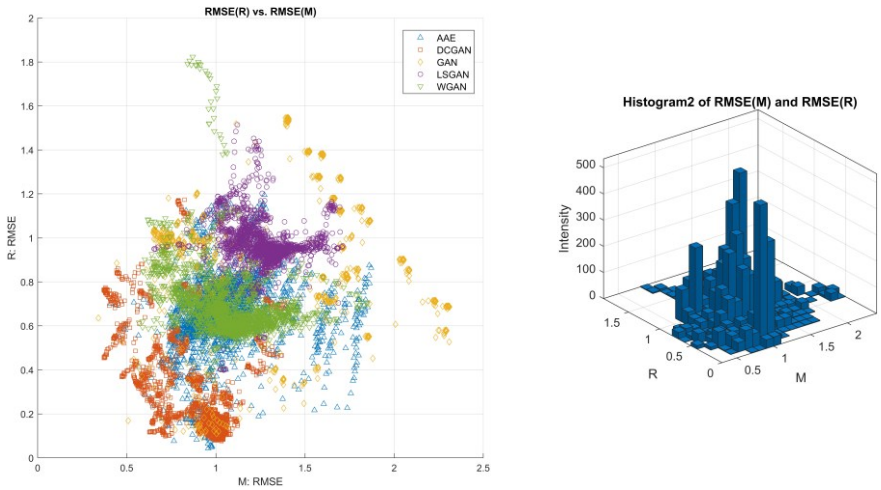

Figure VI-28 RMSE, Scatter plot (Left) and 3D histogram (Right).

While the rest of the GAN methods clustered closer to each other, and this is clear in the 3D histogram (Figure. VI-27 (Right)). PSNR highlighted the superiority of DCGAN in generating synthetic data with better fidelity. While it clusters the rest of the GAN methods close to each other, it indicates that they might share similar limitations in data quality, which could affect their applicability in critical use cases. Nevertheless, Similar findings were observed when calculating the RMSE metric for the synthetic and the original Shannon entropy metric pair {M, R} using the five

different methods. For DCGAN, the metric R was closer to 0, having minimal error, while metric M ranged between 0.4 and 1, still indicating relatively good performance (Figure. VI-28 Left). In contrast, the standard GAN method exhibited an RMSE closer to 2, reflecting higher errors and lower data quality compared to the other methods used. 3D histogram in Figure. VI-28 right shows a high intensity concentrated around 1, representing the comparable dataset produced by the three GAN types: AAE, LSGAN, and WGAN.

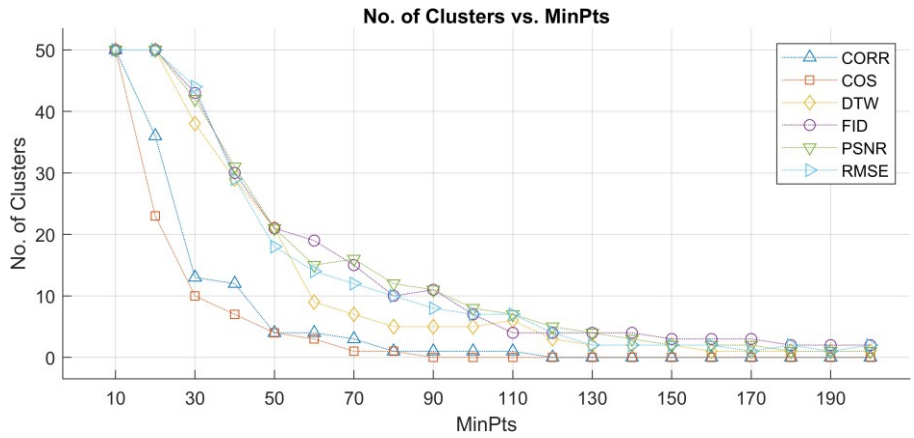

Figure VI-29 Dependence of the number of the clusters on the parameter MinPts of the OPTICS.

OPTICS (Ordering Points To Identify the Clustering Structure) is a density-based clustering algorithm, it is designed to identify clusters of varying densities and shapes by creating an ordering of the data points based on their reachability distances. While it forms a dense region or cluster based on the MinPts parameter (refers to the minimum number of points within a cluster). By using the OPTICS algorithm, we aim to compare the similarity metrics used in evaluating the GAN Methods. The analysis revealed an exponential decay relationship between the number of clusters and the minimum number of points required to form a cluster as illustrated in the Figure. VI-29. Notably, the six-similarity metrics demonstrated distinct results in this context. These metrics are categorized into three main groups based on their clustering characteristics relative to the MinPts:

Group 1: {FID, PSNR, RMSE},

Group 2: {DTW},

Group 3: {CORR, COS}.

The DTW metric exhibited a medium number of clusters compared to others within the MinPts parameter range of {60, 70, …,100}. These findings emphasize the importance of selecting the appropriate similarity metrics for effective analysis of complex data structures, as they could easily evaluate the performance of the method used in the wrong way.

Table VI-7 Comparison of the Used Metrics for Generative AI.

Metric Name	**Feature Capture**	**Evaluation**	**Cost/Complexity**
Cosine Similarity	**(-)**	Poor at capturing subtle differences and temporal patterns.	Low computational cost.
Correlation Similarity	**(-)**	Fails to capture non-linear relationships or temporal variations.	Low computational cost.
Dynamic Time Warping	**(+)**	Excellent for capturing similarity levels, aligning sequences even if they are out of sync.	High computational cost.
Fréchet Inception Distance	**(+)**	Effective for feature selection, it captures relevant features based on their importance.	Moderate to high computational cost.
Pick Signal to Time Ratio	**(+)**	Common in image processing, captures feature similarity by comparing signal quality.	Low to moderate computational cost.
Root Mean Square Error	**(+)**	Captures errors, good for regression tasks where small differences matter.	Low computational cost.

Evaluating the similarity level between the original Shannon entropy metric pair {M, R} and the generated ones using various similarity metrics across five generative AI types (AAE, DCGAN, GAN, LSGAN, and WGAN), it was evident that the GAN type called DCGAN outperformed the others, proving superior synthetic data quality and better alignment with the original data. On the other hand, the traditional GAN type showed the worst performance among all methods, indicating lower quality and higher error rates. These findings highlight the importance of selecting the appropriate GAN model for specific applications. Moreover, the evaluation results

proved the limitations of both correlation and cosine similarities (see Table. VI-7, Figure. VI-29) in capturing the resemblance and quantifying the similarity level between the original entropy pair {M, R} vectors and the generated vectors in contrast to other used similarity metrics (DTW, FID, PSNR, and RMSE).

The synthetic data generated by the GANs can present both risks and opportunities for the next cellular communication generation and future technology. One major concern is the vulnerability of data generated to manipulations, if happen that the attackers could access or influence the GAN model, then it is easy for them to introduce subtle biases or inaccuracies that affect the reliability and security of network applications. The inherent limitations of GANs in capturing highly complex or rare patterns might lead to data inaccuracies and lower model performance in real-world scenarios. Also, generative AI methods demand high computational power while their training process is often unstable, making it unsuitable for high-stakes applications. Nevertheless, we cannot deny that the synthetic data carries some privacy risks, like unintentional retention and recreation of some sensitive patterns from the original datasets, leading to exposing sensitive information. Especially where high-fidelity, individual-like synthetic data is generated, making it possible to trace back to real-world users. Meanwhile, some strategies can be employed where the privacy of the user is a priority, like *differential privacy* [83] techniques, where white noise is added to the original data to reduce the recreation of sensitive information. Also, *privacy-preserving machine learning* [84] methods like federated learning can be leveraged, allowing the GAN model to learn from the distributed data source without getting close to the sensitive information. Other strategies are used in practice to keep the user's privacy while enabling GANs to generate valuable synthetic data. Generative AI remains a potential way for generating large, realistic datasets that can augment the limited real-world data, enhance model robustness, and facilitate simulations for scenarios that are challenging to replicate in real-world conditions. These benefits highlight GANs' value for the 6G, though careful management of their limitations and security risks is essential for safe and effective applications.

VI.5. Reinforcement Learning for Queueing-Based Resource Optimization

The aim of this subchapter is to explore how reinforcement learning can be integrated with queueing system models to optimize packet scheduling and resource allocation in the upcoming cellular networks. Many existing studies focus on packet scheduling and traffic prediction rather than adapting queue management in highly dynamic wireless environment scenarios. Traditional queueing systems often rely on fixed threshold-based loads, where limited attention has been given to the idea of integrating RL within queueing systems, specifically for 6G and THz scenarios, where further complexity is added due to many factors, such as reattempted transmissions, beam misalignment, and intermittent connectivity. Thus, a significant gap in research appears regarding the role of RL in optimizing the queue management for 6G-based queueing systems under dynamic traffic conditions, also the impact of retrial mechanisms on learning-based queueing strategies, and the fairness-energy-latency tradeoff after integration RL for queue optimization, especially for ultra-reliable and low-latency (URLLC) applications.

Retrial Queueing Systems M/M/1/K

We used the queueing system Kendall's notation, a standardized way to describe queueing models. It provides a concise representation of their key characteristics. Kendall's notation follows the format A/B/C/K/m/Z, **A** is the arrival process (e.g., M for Markovian or Poisson arrivals), we have **B** that denotes the service time distribution (e.g., M for exponential service times), and **C** is the number of servers. The parameter **K** indicates the system capacity, including both customers in service and the queue, and **m** represents the size of the calling population (often assumed infinite if omitted). Finally, **Z** is the service discipline, such as first-come-first-served (FCFS). By following this notation, the retrial M/M/1/K model describes a system with Poisson arrivals. Exponential service times, a single server, and a finite buffer size, make it well-suited for analyzing many KPI factors in the 6G networks such as the congestion and resource allocation [J5].

Among all the queueing types that exist, we use a simple example of an M/M/1/K retrial queue as shown in Figure VI-30. M/M/1/K is considered a fundamental model that extends classical queueing systems by using the concept of orbiting customers. This concept allows the clients who find the server busy to retry again after a random delay instead of leaving the system or being a lost client. The model used is relevant for such systems where blocked clients do not immediately depart but make future attempts to be served. State 'Free' of the queue means that there is at least one free location in the queue buffer. We chose this model to study the 6G networks because it effectively captures the impact of blocked mobile terminal requests that reattempt service after a delay, which reflects the real-world scenarios where under dynamic network conditions, the users experience temporary unavailability. As for our simple example, the arrivals follow a Poisson process with rate λ, where the interarrival times are independent and exponentially distributed. Moreover, the service time follows an exponential distribution with mean $1/\mu$, while we implement a single server and a finite queue size K. As we mentioned earlier, the blocked clients enter an orbit and retrieve at an exponential rate θ rather than leaving the system and being immediately lost.

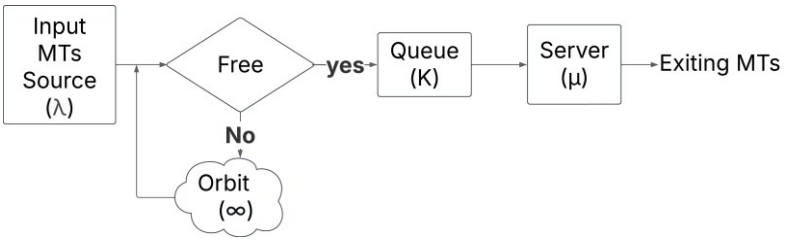

Figure VI-30 Retrial queueing system model.

This retrial queueing model is useful in the upcoming 6G cellular networks, where many unique challenges are introduced in resource allocation and connectivity due to ultra-high frequencies and directional communication. The validity of assuming Poisson process arrival as a simplified example in such complex networks has been supported by multiple studies [85, 86, 87], where it was employed in IEEE 802.15.3c, IEEE 802.11ad, and IEEE 802.11ay / MiWEBA models. Even other types like the Poisson Point Processes (PPP) [88,89] and Switched Poisson Process (SPP) [90] have

proven their applicability in high network scenarios. Given this, our assumption that arrival in the queueing model follows a Poisson process is aligned with existing 6G cellular network models that perform on the THz frequencies, particularly in random access mechanisms, contention-based service requests, and user mobility scenarios. Since we can model the MTs arrivals, AP deployments, and interference sources as Poisson processes in such systems, then the Retrial Queueing System (RQS) is a natural fit for capturing the dynamics of blocked clients' retrials, intermittent connectivity, and access contention in 6G THz networks.

Moreover, one of the scenarios that Poisson arrival is ADAPT MAC mechanism [67]. Since MTs attempt to access the AP dynamically, their arrivals can be effectively modeled as a Poisson process. This assumption aligns with the previously mentioned studies, the Poisson process assumption is relevant in scenarios where MTs independently transmit data whenever they enter an active sector, being random but statistically predictable patterns of arrivals at the AP. However, when the MTs miss their opportunity to access the AP, they may need to retry access in a later sector rotation, introducing a retrial-based queueing dynamic. This end fits naturally into an M/M/1/K retrial queueing model, where the blocked clients enter an orbit and attempt retransmission after a random delay. In ADAPT, missed transmission opportunities do not necessarily result in permanent loss but rather it retries to transmit in the next AP's rotation.

From what has been proven, we consider our RQS within a 6G network scenario, where high-frequency, directional, and intermittent access characteristics of THz communication networks require a retrial-based approach. Our queueing framework aligns with the characteristics of 6G scenarios involving stochastic MT distributions and dynamic access attempts. The beam misalignment, sectorized transmissions, and intermittent connectivity of the 6G networks that can lead to delayed but eventual access opportunities are relevant with the assumption that blocked MTs enter an orbit and retry to access the AP at a later time. By leveraging the RQS model, we capture these fundamental dynamics, ensuring that the presented approach remains scientifically grounded and applicable to the upcoming cellular networks.

For our network scenario, the interarrival time between MTs has an exponential distribution with a parameter. λ. Shows that the arrival process is memoryless, the probability of a new client occurring in a small time interval dt is approximately:

$$P_{arrival} \approx \lambda dt \tag{43}$$

Equivalently, the AP answering time has an exponential distribution with a mean. $1/\mu$, where the probability that a service completion occurs in dt is:

$$P_{service} \approx \mu dt \tag{44}$$

one has to note that these exponential distributions lead the model to be designed as a Continuous-Time Markov Chain (CTMC), having transitions between states occur with rates dependent on the set parameters. $\lambda, \mu,$ and θ.

In the retrial queueing systems, MTs who find the queue full do not leave the system and are not considered lost MT, in contrast, they enter a so-called orbit, as was mentioned previously, and retry to enter the system once again after an exponentially distributed delay with mean $1/\theta$. The probability of MT retrying with a time interval dt is:

$$P_{retry} \approx \theta dt \tag{45}$$

Therefore, we can say that the retrial process follows a memoryless property. The steady-state behavior of the system is analyzed by taking into consideration the number of MTs in the queue and the orbit as well, where the number of MTs in the queue at the time t is noted as $Q(t)$, number of MTs in orbit at the time t is noted as $O(t)$, and $S(t)$ is the number of served MTs at the time t.

The model state transitions follow a so-called balance equation, that describes the probability of each state over time t:

$$dP_n/dt = \lambda P_{n-1} - (\lambda + \mu)P_n + \mu P_{n+1} \text{ , for } 1 \leq n < K \tag{46}$$

In case the system is full ($n = K$), the balance equation incorporates retrial MTs as follows:

$$\mu P_K = \lambda P_{K-1} + \theta P_{orbit} \tag{47}$$

in formulae (47), P_{orbit} represents the probability of an MT being in the retrial state:

$$P_{orbit} = \lambda P_k/\theta \tag{48}$$

formulae (48), guarantees that the system stays ergodic under the stability condition represented as the following:

$$\rho = \lambda/\mu < 1 \tag{49}$$

this requires that the effective arrival rate of the MTs does not exceed the service rate, this testify that the system do not grow indefinitely.

To evaluate the efficiency of the RQS model, we define some key performance metrics, starting with the average queue length (L_q) defined as follows:

$$L_q = \sum_{n=0}^{K} nP_n \tag{50}$$

having P_n represents the probability of having n MTs in the queue. Moving on to the expected number of orbited MTs (L_0):

$$L_0 = \lambda P_K/\theta \tag{51}$$

which defines the average number of MTs in the orbit, the ones who have a chance to retry for service. Nevertheless, we have mean system time noted as W is the average time an MT spends in the system, taking into consideration the waiting time and the service time, and it is calculated as follows:

$$W = L/\lambda_{eff}, \quad L = L_q + L_0 \tag{52}$$

L is the total number of MTs in the system. Last but not least, we have the AP utilization factor ρ that represents the fraction of time the AP is busy:

$$\rho = \lambda/\mu \tag{53}$$

as we saw in the stability condition, equation (49), the system stays stable as long we keep $\rho < 1$, meaning that the arrival rate of the MTs to the system is always less than the effective service capacity. We evaluate the performance of the retrial queueing model as first we implemented it as the pseudocode shows in Algorithm. VI-1.

The model dynamics, including the explained terms: MT arrival, queueing service, and retrial processes, were implemented based on the described mathematical framework. In our simulation scenario, all the used parameters are presented in Table VI-8, where the key values like the MT's arrival rate (λ), the service rate (μ), queue capacity (K), and the retrial rate (θ) are all specified. For the aim of better understanding the dynamics of the retrial queueing systems, and with the help of

MATLAB R2024b, we plotted the evolution of served MTs (with red color), queued MTs (with green color), and orbited MTs (with blue color) (Figure. VI-31).

Algorithm. VI-1. Retrial queueing system pseudocode.

```
// Input
λ: Arrival rate, μ: Service rate, θ: Retry rate, time_sim: Total simulation time, k = Maximum queue length

// Initialize the Simulation
Initialize to zero:
  MTs_in_queue , MTs_served
  MTs_in_orbit, AP_busy

for t = 1 to time_sim
  // MTs arrival based on Poisson process
  if rand() < (λ/time_sim)
    if AP_busy = False
      // AP is free, serve the MT
       AP_busy = True
      MTs_served = MTs_served + 1
    elseif MTs_in_queue < k
      // AP is busy, add MT to the queue
      MTs_in_queue = MTs_in_queue + 1
    else
      // Queue is full, MT go to the orbit
      MTs_in_orbit = MTs_in_orbit + 1

  // Service completion
  if AP_busy = True and rand() < (μ/time_sim)
    AP_busy = False
    if MTs_in_queue > 0
      // Serve an MT from the queue
      MTs_in_queue = MTs_in_queue - 1
      AP_busy = True
      MTs_served = MTs_served + 1

  // MTs retry from orbit
```

```
    if rand() < (θ/time_sim) & MTs_in_orbit > 0
        if AP_busy = False
            AP_busy = True
            MTs_served = MTs_served + 1
            MTs_in_orbit = MTs_in_orbit – 1
        elseif MTs_in_queue < k
            // Move MT from orbit to queue
            MTs_in_queue = MTs_inqueue + 1
            MTs_in_orbit = MTs_in_orbit – 1
        else
            // MTs remain in orbit (queue is full)
    end for
```

The visualization illustrates how the MTs move through the system from the arrival point to the service point, and how the queue and orbit states evolve. As shown in Figure. VI-31, the served MTs reveal a gradual increase over the simulation time, demonstrating the ability of the AP to serve at a steady but limited rate.

Table VI-8 Retrial queueing system model used parameters.

Parameter	**Value**
Arrival rate (λ)	45
Service rate (μ)	40
Retry rate (θ)	20
Queue size (K)	5
Simulation time (T)	1000

In the beginning the system serves a few requests, but as time progresses, the service rate adjusts to serve more requests. Despite that, the serving was not instantaneous, however, it follows a stepwise pattern, denoting that the used model operates under constraints that limit the client processing.

Concerning the queued MTs, we can say that they fluctuate over time, increasing with the increasing number of MT requests and decreasing as they get served. Some periods of stability are observed, meaning that the queue length remains unchanged, indicating that the arrival rate of the MTs and the service rate are momentarily balanced. But there are instances where the queue state grows due to an influx of new

arrivals, as shown in the figure, which can lead to delays and congestion if the service rate does not compensate for the augmented load.

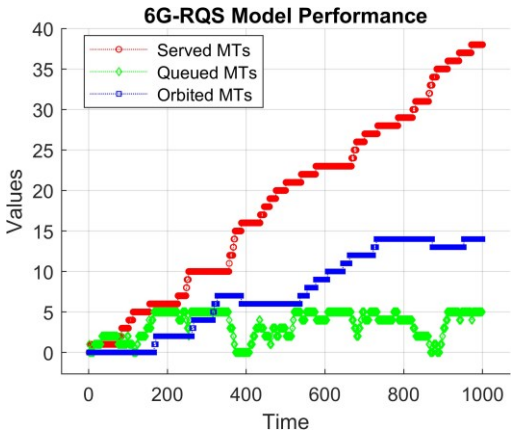

Figure VI-31 6G retrial queueing system model performance.

The orbited MTs in the figure remain at a low level at the beginning of the simulation, as soon as the time progresses it increases when the queue reaches its capacity. This denotes that once the system becomes saturated, the newly arrived MTs are forced into the orbit, waiting for their chance to join the queue. Over time, it grows reflecting the challenges of integrating orbited MTs into the queue in an efficient manner.

By the end of the simulation time, it had successfully served 38 MTs in total, 5 MTs remained in the queue waiting to be served, and 14 MTs were still in the orbit, unable to rejoin the queue. The results show the challenges and limitations of the simulated RQS model in a 6G framework context. The fact of remaining MTs waiting to be served in both queue and orbit shows that the RQS simulated model under the given configuration cannot fully serve all received requests within the simulated time frame. The findings align with the real-world 6G scenarios, where high-frequency communication is susceptible to sectorized transmissions, blockages, and intermittent access, resulting in retransmission delays and service inefficiencies.

To optimize the performance of the system model used, we propose to integrate Reinforcement Learning to improve decision-making, reduce congestion, improve service rate, and minimize overall waiting times. By doing so, the system can

proactively adjust to network conditions, traffic variations, and user mobility, making it more robust for the upcoming 6G and enhancing its KPIs.

Integration of Reinforcement Learning in the Retrial Queueing Systems M/M/1/K for Efficient Queue Management

One of the most famous powerful AI frameworks for decision-making in dynamic systems is reinforcement learning, thanks to the role of its key element, the agent, which interacts with the environment to learn and maximize a cumulative reward. Integrating RL has been widely adopted in dynamic wireless networks for optimizing many factors like traffic scheduling, adaptive access control, and resource allocation, making it a promising technology for the next generation of 6G networks. We believe that by integrating such a powerful tool into the 6G network-based RQS model, we can improve its key performance indicators such as system efficiency, overall balance, and fairness.

Among the most widely used RL techniques are Q-learning and Deep Q-Networks (DQNs). Q-learning is a value-based RL method that enhances the agent's performance and enables it to learn an optimal policy for managing the overall system by influencing the AP. The Q-learning method relies on one of the most effective decision-making equations, the Bellman equation. It formulates the relation between the value of a state-action pair and the expected future rewards, which makes it a unique way. The Q-value update rule is as follows:

$$Q(s,a) \leftarrow Q(s,a) + \alpha[r + \gamma \max_{a'} Q(s',a') - Q(s,a)] \tag{54}$$

in formula (49), $Q(s,a)$ represents the current value of taking action a in a state s, α is the learning rate, meaning the controls how much new information overrides the past knowledge. We have the r and γ that represent the reward received for the action and the discount factor, respectively. The discount factor determines the importance of future rewards. And lastly, the $\max_{a'} Q(s',a')$ is the highest estimated value of the next state s'. This repetitive process allows the agent to stabilize its decision-making over time, improving the efficiency of the system by maximizing the total rewards.

The learned state-action pair of Q-learning is stored in a so-called Q-table. This end is a matrix where each row represents a state s In the system, each column

represents an action a that the agent can take, formulating a cell $Q(s, a)$ that represents the expected reward for taking the action a in the state s based on past learning. During the learning, the Q-table is updated based on the Bellman equation. Over multiple iterations, the Q-values gradually stabilize as the agent refines its knowledge, and the table converges to optimal values, enabling the agent to make the best decisions based on each state. Despite the Q-learning benefits, it suffers from inherent limitations, especially for complex problems. The curse of dimensionality is one of its primary drawbacks. Q-learning relies on tabular Q-value representations, where the number of state-action pairs grows exponentially with the size of the state and action spaces. This aspect makes Q-learning impractical for large or continuous state spaces.

Q-learning method suffers from limitations, as was mentioned, especially for dynamic systems, and here comes the deep Q-network method to overcome it by integrating deep neural networks as function approximators. Instead of following the Q-table that grows exponentially with the state-action space, DQN utilizes a neural network to approximate the Q-values for each state. The method used helps the agent to handle complex systems with large and continuous state spaces effectively. Deep Q-network uses experience replay, where past experiences like the state, action, reward, and next state are stored in a buffer and randomly sampled during training, which improves the stability of learning. Besides what has been said, DQN employs a target network that updates copies of the main Q-network periodically and stabilizes learning.

One of the methods that belongs to the border class of policy-based reinforcement learning is the critic-based methods, which learn the explicit policy rather than a value function. The agent in these methods consists of two components: the actor and the critic. The actor determines the policy by mapping states to actions, and the critic evaluates the actions taken by estimating the value function. Critic-based methods have several benefits; they are more stable in continuous action spaces, and they can adapt better to non-stationary environments, as they do not require discretization.

In our design, we chose RL to act as an upper-layer controller that dynamically enhances the performance of the AP based on real-time observation from the

environment. The integration of RL in the RQS is shown in the Figure. VI-32 and in Algorithm. VI-2, which has the following structure: the *environment* consists of the input source (λ), the queue (K) and the orbit (∞). The *agent* observes the system state, including queue size and AP availability, and based on the observation, the agent selects an *action*:

Action = 0: Do nothing, let the system operate normally.

Action = 1: Force the AP to serve one MT.

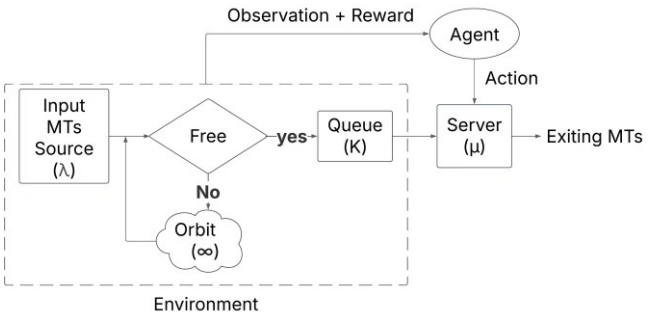

Figure VI-32 reinforcement learning integration in the retrial queueing system model.

The AP must execute the action, impacting the environment state, where the reward is assigned based on the performance, encouraging actions that improve one of the KVIs, the system efficiency. The high-dimensional state space features consist of the current queue lengths, sector occupancy levels, and packet arrival rates for all sectors in the cell, which serve as inputs to the reinforcement learning agent.

We define the reward function as it is shown in algorithm.2 and as follows:

$$\text{Reward} = \alpha \cdot \Delta(\text{served MTs}) - \beta \cdot \Delta(\text{queued MTs}) \quad (55)$$

formula (55) is designed to balance the trade-off between serving more mobile terminals and preventing excessive queue build-up. α is considered a scaling factor to encourage serving more MTs during the simulation time, reinforcing actions that improve the throughput and decrease congestion. $\Delta(served\ MTs)$ is the change in the number of successfully served MTs after taking an action. A higher value of $\Delta(served\ MTs)$ increases the reward, influencing the agent to prioritize service efficiency.

Algorithm. VI-2. Reinforcement learning integration pseudocode.

```
// Define Environment
  // contains the RQS simulation-based inputs, state, and reward
// 1. Simulation-based Input
λ: Arrival rate, μ: Service rate, θ: Retry rate, time_sim: Total simulation time,
 k = Maximum queue length

// 2. State (2D vector)
Number of MTs in the queue, AP status (busy/free)

// 3. Reward
R = α · (Δserved MTs) − β · (ΔMTs in queue)

// Define observation
Number of MTs in the queue, AP status (busy/free)

// Define Action
if Action = 0
   Agent does nothing;
else
   Agent forces AP to serve one MT
```

On the other hand of equation (55), β represents a weight that regulates the penalty for increasing queue length. While $\Delta(queued\ MTs)$ is queue size changes due to the action taken. A higher queue length increases the penalty, and decreases the reward, discouraging actions that might lead to network congestion and inefficiencies.

By adjusting the scaling factor α and the weight β, we control the agent's decision-making, ensuring the balance between maximizing throughput and preventing service bottlenecks. The used mechanism allows the reinforcement learning agent to dynamically adapt its policy based on real-time network conditions and optimize the 6G-RQS model for reaching higher efficiency and better resource utilization. For implementing the RL in our 6G-RQS model, we utilized DQN, which extends traditional Q-learning as was explained previously and defined in pseudocode VI.2.

The layered design of the critic neural network is shown in Figure. VI-33 to effectively capture the complex relation between the state and the optimal actions. The

input to the network is the state representation of the 6G-RQS system, next, we have the first fully connected layer that consists of 24 neurons, capturing the high-dimensional features of the state space.

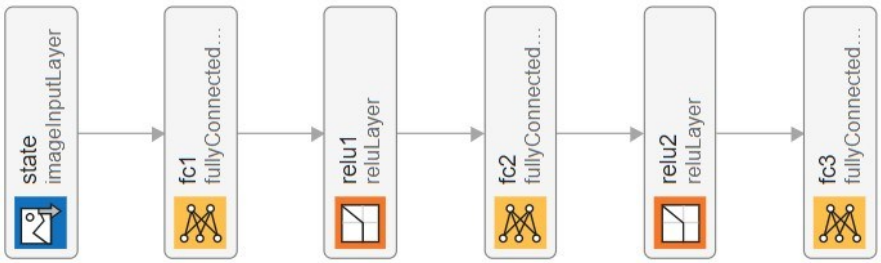

Figure VI-33 Design of the critic neural network.

We used the rectified linear unit (ReLU) activation function as the third layer in the NN to introduce non-linearity, ensuring the network can model complex decision boundaries.

Table VI-9 DQN critic network training parameters.

Parameter	Value	Description
Gradient Threshold	1	Limits the magnitude of a gradient to prevent instability.
Learn Rate	10^{-3}	Controls the step size in weight updates, ensuring smooth convergence.
Target Smooth Factor	10^{-1}	Determines the smoothing factor for updating the target network, for stable learning.
Experience Buffer Length [Bytes]	10^{6}	Defines the size of the replay buffer used for experience replay, improving sample efficiency.
Discount Factor	0.99	Ensures future rewards are considered.
Mini Batch Size	64	Specified the number of samples used per training step for gradient update.
Number of Episodes	10	Defines the number of training episodes used for learning the policy.

The fifth layer is again a fully connected layer; this layer further refines the learned features and contributes to the depth of the network. It follows that the second ReLU activation function enhances non-linearity and stability, and finally, a third fully connected layer as an output, which provides the Q-values for each possible action that the agent uses to select the optimal action for a certain state based on the highest predicted reward.

Table. VI-9 presents the key hyperparameters used for the DQN-based critic network, these parameters are carefully selected to ensure stable and efficient learning, balancing convergence speed and generalization performance. These hyperparameters play a crucial role in refining the performance of the DQN model, ensuring that critic network effectively learn optimal actions to enhance the 6G-RQS system efficiency.

Table. VI-10 presents the parameters used in the simulated model, where we systematically varied three key factors to analyze the system's performance under different conditions. The first parameter is the arrival rate λ which we adjusted to six different values to examine its impact on the system behavior and congestion level. Additionally, the queue size K we modified across four different cases to assess how varying buffering capacities affect service efficiency.

Table VI-10 Used parameters for the simulation.

Parameter	**Value**
Arrival rate (λ)	[20, 30, 50, 70, 90, 100]
Service rate (μ)	0.5
Retry rate (θ)	1
Queue size (K)	[10, 15, 20, 40]
Scaling factor (α)	[0.1, 0.3, 0.5, 0.7, 0.9]
Weight (β)	$1 - \alpha$
Simulation time	100 time units

Moreover, the scaling factor α in the reward function also varied across five distinct values and always between 0 and 1, to investigate its influence on the RL agent's decision-making process.

This results in a total of 120 simulated scenario cases ($6 \times 4 \times 5$). The simulation time was fixed to 100 time units for all cases to ensure consistency and comparability.

To assess the impact of reinforcement learning on system dynamics, we analyzed different performance metrics over the learning process and across 10 training episodes. Figures VI-34 and VI-35 illustrate system behavior under two different fixed queue sizes (K), and reward parameters (α, β), while considering all six different arrival rates λ Scenarios. The weight $\beta = 1 - \alpha$ ensures that the reward function always maintains a balanced trade-off between different objectives, such as the KPIs throughput and delays, without arbitrarily amplifying or diminishing their combined influence. By doing so, the total weight sum is constant ($\alpha + \beta = 1$), preserving the relative importance of each term while allowing controlled adjustments through α. Each figure has three subplots that show the evolution of three metrics: the number of served MTs, the number of queued MTs, and the number of orbited MTs throughout the simulation time. By analyzing these trends, we could evaluate the model's ability to optimize the AP's service efficiency, reduce congestion, and balance the resource allocation in a 6G-driven queueing model.

Figure VI-34.a represents the number of served MTs for a queue size of 20, scaling factor 0.1, and reward penalty weight 0.9, under six different arrival rate scenarios. The plot spans 10 episodes, each episode consists of 100 time unit steps, exporting the system's performance across the overall learning time. One can notice the gradually increasing trend in the number of served MTs from episode to episode for all arrival rate cases, reflecting the improvement of the system's performance as the RL agent learns and adapts to the environment.

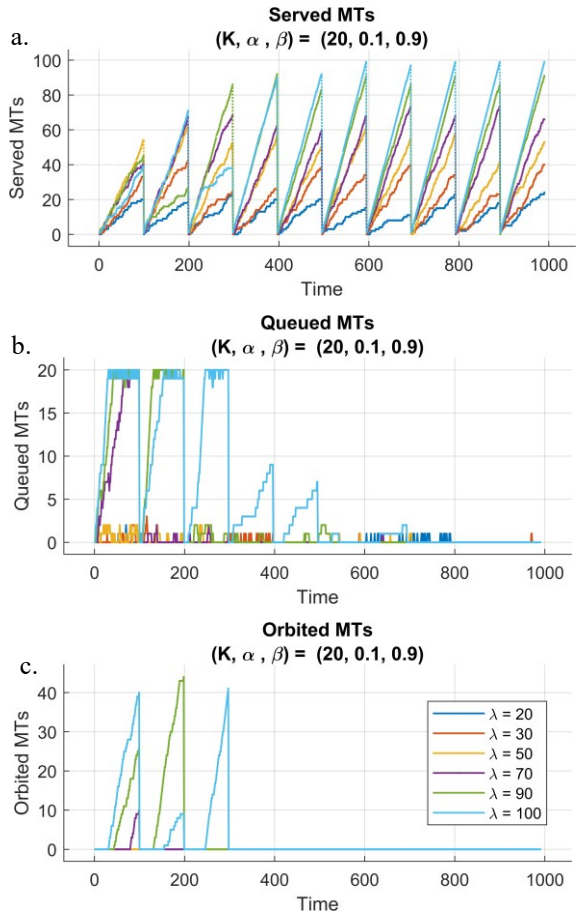

Figure VI-34 Performance of 6G-RQS with RL Integration: Served (a), Queued (b), and Orbited (c) MTs for (K,α,β) = (20,0.1,0.9).

The improvement proves the agent's ability to optimize the decisions over time, gradually improving its understanding of the queueing dynamics. However, in certain cases, there are periodic decreases in performance, where the number of served MTs drops for some time during specific episodes.

This behavior can reflect the inherent nature of the RL, where the agent tries to explore other strategies in the early stages of learning, leading to suboptimal actions before convergence to better policies. But this behavior happens temporarily, because the number of served MTs consistently increases in subsequent episodes, demonstrating the effectiveness of the RL algorithm in balancing exploration and exploitation, leading to an improvement in system performance across simulation

periods. We can say that this behavior is indicative of the agent's continuous learning process, progressively adjusting to the system dynamics.

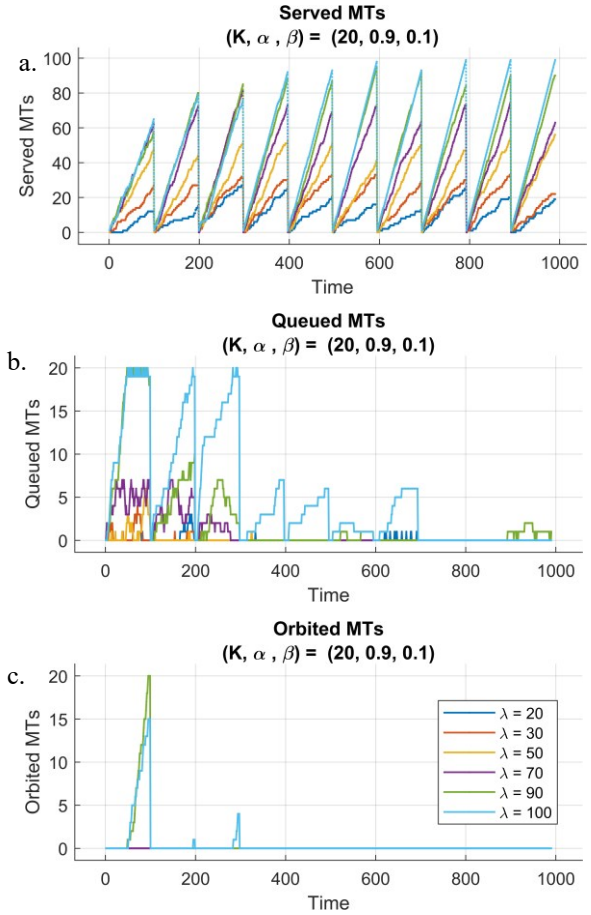

Figure VI-35 Performance of 6G-RQS with RL Integration: Served (a), Queued (b), and Orbited (c) MTs for (K,α,β) = (20,0.9,0.1).

Figure VI-34.b illustrates the evolution of the queued MTs across 100 time steps repeated for 10 episodes under the same scenario. Initially, during the first steps, we can observe that the queue increases till gets full, particularly for higher arrival rates ($\lambda = 70, 90, 100$). This behavior is expected, as the agent has not yet adapted to the environment and has not yet learned the optimal policy for managing the requests and resource allocation. As the agent interacts more with the environment and refines its decision-making over episodes, we can notice a decrease in queued MTs. For certain arrival rates, the queue eventually reaches zero, indicating that all MTs got served,

which demonstrates the agent's ability to effectively balance the system's load and prevent excessive buildup of queueing MTs. In contrast, one can observe that when the queue becomes full at any point, a corresponding rise in the number of orbited MTs is seen. However, this aspect was expected to happen because the MTs who cannot join the queue are sent directly to the orbit rather than allowing them to be lost (see Figure VI-34.c).

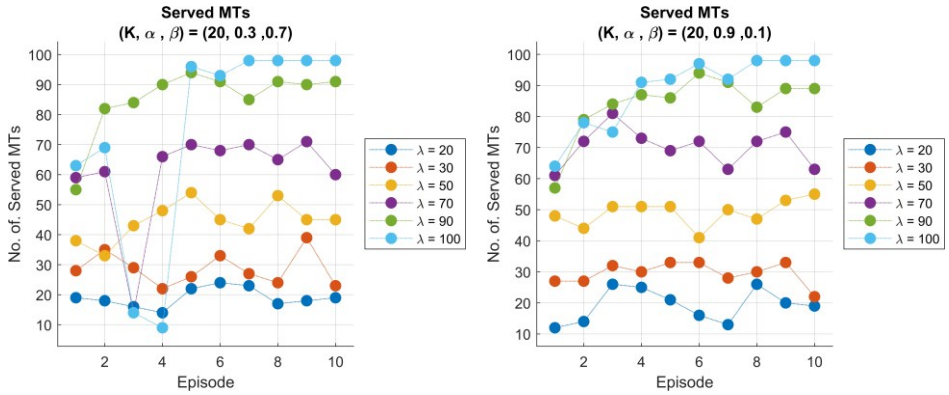

Figure VI-36 Performance of 6G-RQS with RL integration: total served MTs per episode: for (K, α, β) = (20, 0.3, 0.7) (Left), and (K, α, β) = (20, 0.9, 0.1) (Right).

The trends observed for served MTs, queued MTs, and orbited MTs for the previous scenario ($\alpha = 0.1$) are also evident for $\alpha = 0.9$ (see Figure VI-35). However, one noticeable difference exists between the two scenarios, which is the faster increase in the number of served MTs for $\alpha = 0.9$. This can be attributed to the higher scaling factor of the reward function, which influences the agent to maximize the number of served MTs rather than focusing on managing the queue size effectively. This higher scaling factor leads the agent to take actions that directly reduce the number of queued MTs but might not take into account the long-term consequences of this approach. While the agent focuses more on improving the service rate of the AP, it might neglect queue management. This approach highlights the trade-off between the scaling factor in the reward function and the agent's ability to optimize both the served MTs and the queue dynamics. Moreover, we visualize the total number of served MTs per episode for two different scaling factor values, $\alpha = 0.3$ (left) and $\alpha = 0.9$ (right) (see figure VI-36). The plot shows that in cases where the scaling factor equals 0.3, there is a

noticeable drop in the number of served MTs, particularly for higher arrival rates. The drops are characterized by high fluctuations in performance.

This behavior suggests that the agent's decisions may lead to suboptimal actions, mostly during the early learning stage. This could be due to the low reward scaling factor, which causes the agent to be less motivated to focus on enhancing the serving performance and more inclined to balance the system in ways that take time to get the optimal performance. On the other hand, for $\alpha = 0.9$, the total number of served MTs shows a stable and gradual progression compared to the other scaling factor scenario, with a slight decrease in performance observed occasionally. These smaller drops may indicate that if we set a high scaling factor for the reward, we encourage the agent to optimize the number of served MTs over time while maintaining better control over fluctuations. In general, the agent can adapt effectively under various circumstances and avoids large performance drops that are observed in the lower α scenarios. We can conclude that the choice of the scaling factor plays a crucial role in the agent's ability to stabilize the system's performance and manage trade-offs between serving MTs and system dynamics.

To evaluate the performance of the model and analyze the relationship between the components of served MTs, we performed Singular Value Decomposition (SVD) on the overall learning time series of the served MTs for all cases. The SVD of matrix A is given by:

$$A = U \cdot S \cdot V^T \tag{56}$$

U is an $m \times m$ an orthogonal matrix containing the left singular vectors, S is an $m \times n$ diagonal matrix with singular values, and V^T is an $n \times n$ orthogonal matrix containing the right singular vectors. For our model, we have $m = 10$ episodes, and $n = 100$ simulation times for each simulation case. For the purpose of dimensionality reduction and retaining the most significant components of the matrix, we selected rank $r = 2$, meaning that we chose the top two singular values to approximate the original matrix, because these two singular values give over 90% of the information content of all singular values. The reconstructed matrix is calculated as follows:

$$A_r = U_r \cdot S_r \cdot V_r^T \tag{57}$$

S_r contains only the top r singular values, and U_r and V_r are the corresponding reduced matrices. To quantify the approximated error, we calculate the RMSE between the original matrix of served MTs and the reconstructed A_r.

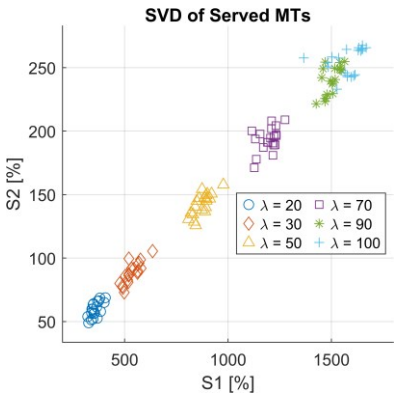

Figure VI-37 SVD of the served MTs.

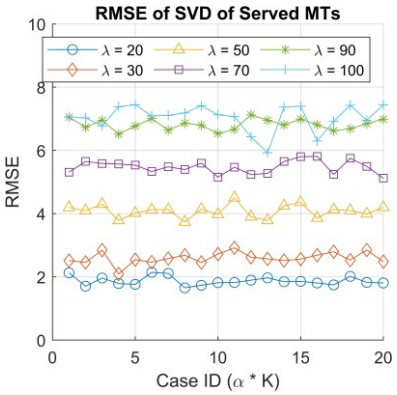

Figure VI-38 RMSE of the original and recomposed served MTs using SVD.

Additionally, for further analysis, we extracted the diagonal of the matrix S, and we plotted its second value versus its first value, which represents a comparison between the second and first singular values. This analysis gives us the right to explore how the most dominant singular values correlate with each other and whether the reduction to two components could effectively capture the features of simulated scenarios. By making this analysis, we not only study the quality of the served MTs' matrix, but also gain insights into the data structure, and check the key factors that influence the performance of the system under varying configurations.

The first and second singular values extracted from the matrix S is represented as a scatter plot for all 120 simulated cases (see Figure VI-37). Interestingly, we could observe that different arrival rate scenarios naturally formed distinct clusters, resulting in six well-defined groups corresponding to the six arrival rate values used in our simulations. One must note that the fifth and sixth clusters, which correspond to arrival rates $\lambda = 90$ and $\lambda = 100$, appear close to each other in the singular value space. This could suggest that the system exhibits similar structural characteristics under these high-load conditions, likely due to the saturation effects of the queueing system as the arrival rate approaches its upper limit. The found clustering behavior proves the strong

impact of the arrival rate on the learned policy and system dynamics. Nevertheless, the distinct clusters reinforce the effectiveness of SVD in capturing the dominant patterns within the served MTs matrix, offering valuable insights into the fundamental structure of the learned 6G-driven RQS system dynamics.

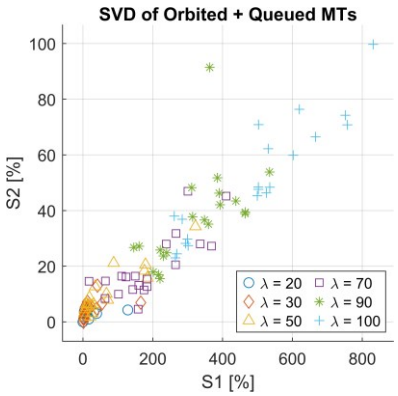

Figure VI-39 SVD of the orbited + queued MTs.

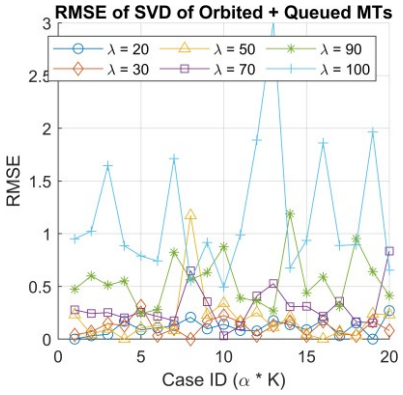

Figure VI-40 RMSE of the original and recomposed orbited + queued MTs data using SVD.

We also plotted the calculated RMSE for all 120 simulated cases to assess the reconstruction accuracy of the SVD-based approximation. Again, we observe a clustering effect in the RMSE values (see Figure VI-38), which appears to correlate with the arrival rates used in the simulations. The higher arrival rates tend to exhibit larger RMSE values, likely due to increased system congestion and variability in decision-making as the agent learns to manage the queue and orbit more efficiently. Moreover, this indicates that for a higher arrival rate, the first two singular values are not enough, and we need more to approximate the original matrix. In contrast, lower arrival rates result in lower RMSE values, indicating more stable system behavior with fewer fluctuations in the served MTs count.

We performed the SVD analysis again, and this time on the combined matrix of orbited MTs and queued MTs, following the same methodology applied previously for the served MTs. We then calculated the RMSE between the original and reconstructed matrices using reduced-rank approximations, $r = 2$. Unlike the served MTs case, the result for both the scatter plot of singular values (see Figure. VI-39) and the RMSE distribution (see Figure. VI-40) did not exhibit a clear clustering pattern. This indicates

the irregular behavior of the queued and orbited MTs and suggests that they are less structured, making it harder to differentiate scenarios based on SVD in this case. A possible explanation for this behavior difference is that the served MTs directly reflect the agent's learning and decision-making process. In contrast, the queued and orbited MTs are more dependent on system congestion and queue dynamics, which fluctuate more unpredictably across different scenarios. The finding highlights the usability of SVD in capturing patterns of served MTs, however, it might be less suitable for decomposing the queued and orbited MTs due to their chaotic nature.

The overall results demonstrate the usability of integrating DQN-based RL in the next 6G and especially in RQS scenarios, significantly optimizing system efficiency and adaptability. The increased number of served MTs across episodes shows that the agent can learn and optimize decision-making over a certain time. Moreover, the reduction of the queued and orbited MTs reflects the balanced resource allocation even under high arrival rates. The ability of the model to adjust the dynamic nature of the environment based on real-time observations underlines the potential of RL approaches in future wireless networks and proves its powerful uses for 6G cellular communication systems, promising improved fairness and greater scalability. One should note that the observed clustering primarily reflects the discrete arrival rate values rather than underlying network dynamics. Future investigation could incorporate variable and bursty arrival rates to further evaluate and enhance the adaptability of the proposed solution.

To evaluate the performance of the DQN in optimizing the 6G-DQN, we analyzed the evolution of Q-value over time. To be more specific, at each time step t within an episode e, we extracted the Q-values corresponding to all possible actions. Based on the DQN decision rule, the action a_t was selected to conform to the maximum Q-value:

$$a_t = arg \max_{a \in A} Q(s_t, a, \theta) \tag{58}$$

Having $Q(s_t, a, \theta)$ is the estimated Q-value for the state s_t and action a given the neural network parameters θ. The set of possible actions is represented by A, and $a_t$is the action selected at the time step t.

a.

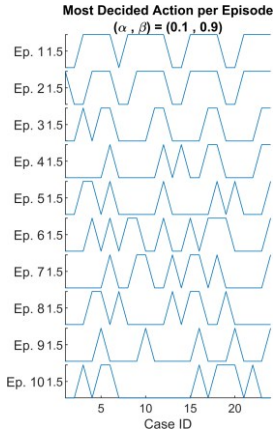

b.

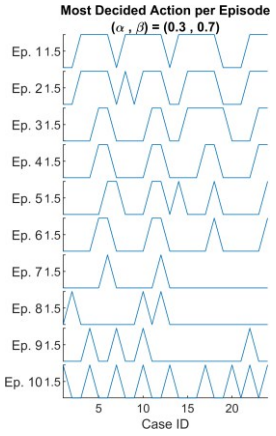

c.

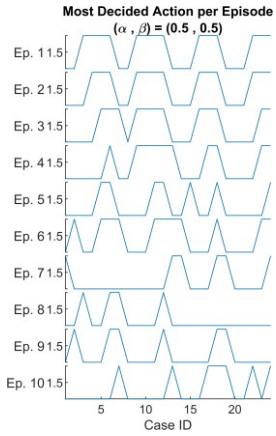

d.

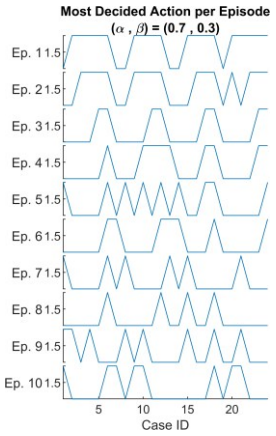

e.

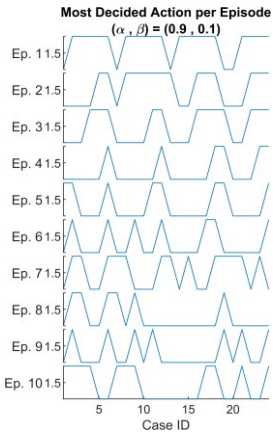

Figure VI-41 DQN-based most decided actions per episode versus case ID.
for: $(\alpha, \beta) = (0.1, 0.9)$ (a), $(\alpha, \beta) = (0.3, 0.7)$ (b), $(\alpha, \beta) = (0.5, 0.5)$ (c), $(\alpha, \beta) = (0.7, 0.3)$ (d), and $(\alpha, \beta) = (0.9, 0.1)$ (e).

Given that we have 120 different simulated cases, each generating a series of 1000 length (i.e., 100 simulation time steps per episode over 10 episodes), therefore, it might be impractical to directly visualize them or try to compare between. To address this, we analyze the most frequently selected action within each episode. Specifically, for each time step e, we calculate the mode of the chosen actions over the 100-time steps. Therefore, we could interpret DQN's learning behavior and optimization performance in the 6G-RQS model.

We visualize the most frequently decided action per episode by using a stacked plot representation (see Figure. VI-41). We construct a stacked plot where:

- The x-axis represents 24 cases, corresponding to the combination of 6 arrival rates λ and 4 queue size K (i.e. 6×4).
- The y-axis represents 10 episodes, progressing from top to bottom, illustrating the evolution of the agent's decision over time.
- It results in five stacked plots, each corresponding to a different scaling factor α of the rewards function.

By the beginning of the learning process (upper sections of the plot), we could observe a structured pattern where the decision-making process exhibits four distinct periods, representing four queue sizes used in the simulation, each period has 6 cases representing the 6 arrival rates λ.

This finding indicates that in the initial learning stage, the agent's policy is still developing, and its behavior is influenced by the predefined queue configuration rather than adaptive learning.

As we progress further down the plot, meaning later episodes, thus a more involved learning stage, we observe that these distinct periods begin to be refined based on the states and cases. This suggests that the DQN-based agent has gradually adapted to the dynamic nature of the 6G-RQS environment, learning to make more context-aware and optimized decisions rather than being rigidly influenced by static queue configurations. This adjustment is consistent across both presented cases and the other three scaling factor cases as well, reinforcing that the learning process is effective for different values of α.

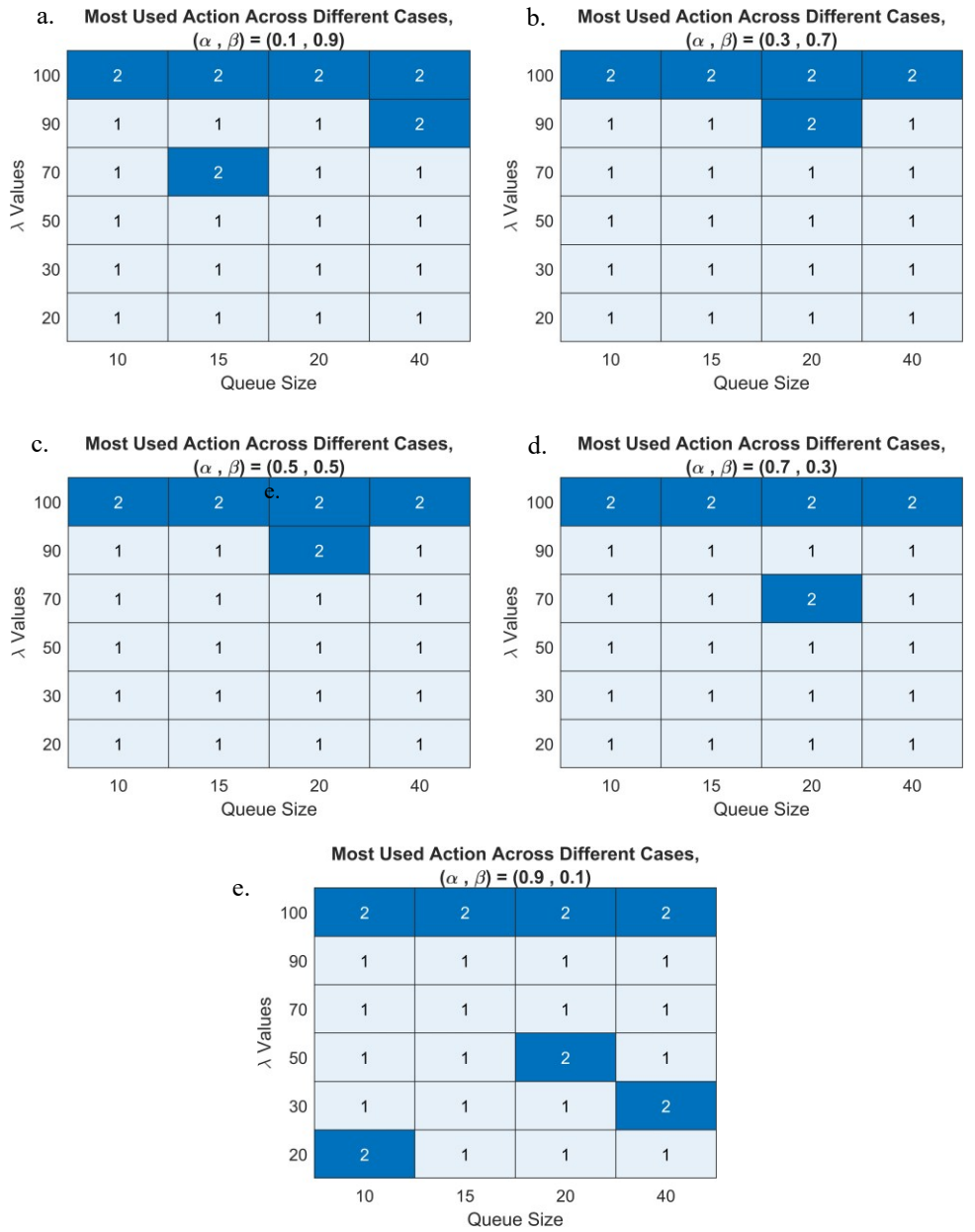

Figure VI-42 DQN-based most decided actions heatmap for: $(\alpha, \beta) = (0.1, 0.9)$ (a), $(\alpha, \beta) = (0.3, 0.7)$ (b), $(\alpha, \beta) = (0.5, 0.5)$ (c), $(\alpha, \beta) = (0.7, 0.3)$ (d), and $(\alpha, \beta) = (0.9, 0.1)$ (e).

We further analyzed the decision-making trends of the DQN-based 6G-DQN model, as we visualized the most decided actions throughout all learning episodes using a heatmap representation.

We can see in all heatmaps the following: the columns correspond to the four different queue sizes K, the rows represent the six-arrival rate λ, resulting in a 24-box grid (i.e. 4×6) where each box indicates the most chosen action for that specific scenario. Since the most used action varies depending on the reward scaling factor α, we generate five separate heatmaps presented in Figure. VI-42.

The results demonstrate that for arrival rates between 20 and 90, the most frequently selected action is action 1 (Do nothing) across almost all cases, with only a few exceptions. Notably, we saw that during these simulated cases, the performance of the system was enhanced, characterized by an increasing number of served MTs with a decreasing number of queued MTs, and efficient resource utilization, ensuring that the AP operates optimally without any necessity to force servicing. This finding suggests that the DQN agent has successfully learned to regulate the queue dynamics and only forces the AP to serve when it is necessary to maintain an optimal system rate. The model effectively identifies the right moments to allow natural service progression versus when to take action, thereby preventing unnecessary congestion and ensuring high throughput.

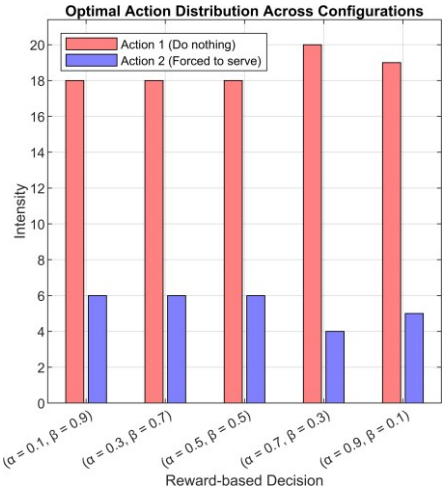

Figure VI-43 Critic NN learned weights-based most decided actions histogram for all cases.

In contrast, for the highest arrival rate case ($\lambda = 100$), the agent consistently favors action 2 (‘force to serve one MT’) as the most frequently chosen action across all queue sizes. This result can be attributed to the fact that at extremely high traffic

loads, the natural service rate becomes insufficient to prevent excessive queueing and orbiting. To mitigate queue overflow and maintain stability, the agent chose action 2, forcing service operations, ensuring that MTs are processed at a faster rate to prevent degradation of system performance.

For the critic NN, we mentioned that we have used a fully connected output layer containing 24 neurons. After the simulation is finished, the output layer produces compressed Q-weights for the overall Q-values, resulting in 24×2 (24 neurons output, and 2 actions) for each simulation case. So, we determined again the most used actions, but this time based on the agent's experience after it finishes the simulation. We compared the Q-weights for each neuron output and selected the action with the maximum weight, then extracted the most used action across all simulated cases. The results were then visualized across five different reward scaling factors (α) using histogram representations (see Figure. VI-43). This approach allows us to extract the learned decision-making patterns after the training phase is complete, providing insights into the agent's policy adaptation across different scenarios.

One important aspect to highlight in Figure. VI-43 is that for each α case, the sum of the red bars (action 1: Do nothing) and the blue bars (Action 2: force to serve) always equals 24 cases. For the majority of cases across all scaling factors, action 1 was selected most frequently. This reflects that the DQN agent has effectively learned to maintain system stability by selectively choosing when to intervene, rather than constantly forcing service that leads to unnecessary energy consumption, and we can say that the agent has adapted to the system dynamics, identifying optimal moments to allow natural service progression while ensuring energy efficiency. Interestingly, in approximately four cases per α instance, we observe a higher selection of action 2 (force to serve). Based on earlier analyses, these cases predominantly correspond to high arrival rate values, $\lambda = 100$. This behavior aligns with the agent's learned policy, where at a moderated to low arrival rate, the system operates effectively without frequent intervention, allowing for smooth queueing and processing. At higher arrival rates, natural service progression is insufficient to prevent queue overflow and increased MT orbiting; in such cases, the agent actively forces service operations to maintain performance and prevent system degradation.

Discussion of the RL DQN Simulation Fundings

The research study findings [J5] demonstrate that integrating DQN reinforcement learning into the 6G-RQS model significantly enhances system performance by dynamically adapting service decisions based on network conditions. We could see that the agent's learned policy effectively balances serving MTs, queue management, and resource allocation, ensuring optimal performance while minimizing unnecessary energy consumption. The key observation from the research is that the agent efficiently adjusts to different traffic loads, learning when to prioritize service (high λ), and when to conserve resources (low λ). On the other hand, we have the singular value decomposition analysis, that further highlights distinct patterns in system behavior, particularly in served MTs, where traffic rates naturally formed clusters, an insight that could aid in traffic prediction and resource optimization.

These contributions align with the upcoming 6G cellular network goals of autonomous, intelligent, and ultra-efficient communication systems. The integration of RL in such complex and dynamic applications would overcome many challenges that the 6G faces, enhance URLLC, improve energy efficiency, and enable adaptive service mechanisms. Nevertheless, this integration is valuable for operating in the THz spectrum, where directional communication, high path loss, and dynamic beamforming challenges require intelligent MAC-layer adaptation. Further investigation might be done in analyzing the effect of the retrial rate of the 6G-RQS model, as it plays a crucial role in determining system congestion levels and the efficiency of reattempting service for orbiting MTs. One should note that the current model does not incorporate the real retransmission mechanism of the orbited MT. while including this mechanism in future work could allow for a more accurate assessment of the method's performance.

We could also explore Multi-Agent Reinforcement Learning (MARL) to enable decentralized decision-making for dense ultra-dense network deployments like the 6G networks. The MARL method could be useful for such scenarios that use multiple APs and MTs and interact dynamically, by doing so, the system could adapt itself under various conditions, mobility patterns, and interference conditions, ensuring seamless

connectivity and efficient spectrum utilization in 6G-THz environments. Future validation with real-world datasets and hardware testbeds will be essential to confirm the scalability and robustness of the proposed model.

CHAPTER VII

CONCLUSION

Studying the new MAC mechanism ADAPT from different aspects helps in understanding more the behavior of the protocol which leads to enhancing the new technology. Transmission distances, collision rate, throughput, and received power, all properties were taken into consideration in the analysis while different simulation scenarios were executed in addition to the dual parameters: rotation step and overlapping ratio that played a crucial role in the ADAPT system. Applying a powerful mathematical tool like Shannon entropy contributed to the enhancement of technology, where we evaluated the mutual effect between the two different subsystems introducing usable metrics for characterizing the transmission power of the MTs in ADAPT. Shannon entropy metrics reveal the interactions between subsystems in the THz MAC mechanism, emphasizing their impact on communication performance. Moreover, the use of decomposition techniques, such as EMD, EEMD, and MHS, enables a deeper understanding of the topological effects and their impact on signal quality. The analysis of our throughput data using the EMD method in both left-to-right and right-to-left directions revealed a strong dependence on the processing direction. This dependence is likely attributed to the end effect issue, which affects the EMD's performance. In contrast, when applying the EEMD method, the results indicated its independence from the processing direction, showcasing its superiority in mitigating such issues. Furthermore, the trend extracted through our proposed method (section V.2) demonstrated a remarkable correspondence with the fitting curve, showcasing the reliability and accuracy of our approach in analyzing radio channel throughput signals. This alignment between the extracted trend and the fitting curve underscores the effectiveness of our proposed method. By examining the fitting curve parameters obtained from our method, we observed the emergence of two distinct clusters. These clusters corresponded to the congested and non-congested states of the radio channel throughput signal.

Additionally, applying MHS enables a deeper understanding of the impact of MTs distribution topology type on the received power. These insights are pivotal for designing high-performance, high-speed communication systems, where careful consideration of network topology can significantly enhance overall efficiency and reliability. It was discovered 17 dB ratio between the variance of PRx MHS for

centered and uniform topologies, which shows the importance of the topology design in high-speed radio networks.

The use of DBScan-based unsupervised learning proves its competence in categorizing different classes, meanwhile, wavelet transform proves its capability in feature extraction with an accurate result of the RNN model in a super short time, approximately 47 seconds. In addition to that, the proposed metric WATR could successfully quantify the goodness of the transfer learning multi-layer RNN models by considering both the accuracy and learning time. Other transfer learning models can be studied and applied in the next study stage in order to discover other unknown behaviors. As for the fourth AI method, we applied five different generative AI methods where twenty synthetic data were produced per method. By calculating the similarity using 6 similarity metrics, it was validated that DCGAN had the highest performance. These results indicate testing the labeled GAN in future work and integrating other types of neural networks (convolutional, transformer, etc.) would be interesting and helpful. Higher order flux of the entropy will be analyzed in the continuation of this research. We could demonstrate that the regular RQS model suffers from many challenges, especially under high demand. We proposed using the RL-DQN approach to enhance the system performance by increasing the number of served MTs, reducing queue congestion, and managing retrial processes. The findings revealed that the integration of such a powerful tool adapts to varying traffic conditions, learns optimal service policies, and balances energy efficiency with fair resource allocation. Singular value decomposition identifies structured patterns in served MTs, underlining the system's learning process and decision-making trends. Moreover, the histogram and heatmap analyses of agent decisions confirmed that the RL effectively determined the best moments to force service while ensuring overall system efficiency. And for work we will investigate the impact of the retrial rates, and multi-agent learning approaches and use THz simulated data for validation to extend the proposed model's applicability.

These findings outline the significance of the data processing before AI integration concept in enhancing the performance of communication systems. By combining classical mathematical tools with AI techniques, we could not only optimize data

processing but also improve feature extraction, leading to more accurate models. This contribution is pivotal for advancing the capabilities of the next wireless communication generation, particularly THz-based networks, where efficient resource allocation and robust communication strategies are essential for meeting the demands of future applications. Nevertheless, data processing simplifies the complexity while also reducing costs, making it a solution for future technology.

The current study is analyzing events in micro timescales, therefore future research will focus on extending the scope of our analysis by evaluating events over a macro timescale, specifically within the range of 10 to 60 seconds. This broader temporal perspective will provide a more comprehensive understanding of the overall MAC system. In the next research phase, we plan also to enhance the ADAPT protocol to simulate both uplink and downlink communications, rather than being limited to uplink only. The extension will allow us to explore the full potential of the communication system. Furthermore, we aim to incorporate additional classical mathematical processing tools for enhancing and extracting features for assessing their impact on AI performance, thereby refining our approach to the accuracy of our results. This multi-faceted research agenda will contribute to the development of more efficient and adaptable communication strategies for the upcoming generation of wireless networks.

OWN PUBLICATIONS

List of Own Publications Referred in the Dissertation

[J1] **Talbi, D.**, Gál, Z.: Decomposition Based Congestion Analysis of the Communication in B5G/6G TeraHertz High-Speed Networks. Infocommun. Journal 15 (Special), 43-48, 2023 **(Wos, Scopus, Q3, IF: 0.9)**.

[J2] **Talbi, D.**, & Gal, Z.: AI-driven insights into B5G/6G MAC mechanisms: A comprehensive analysis. *Internet of Things*, *31*, 101571, 2025 **(WoS, Scopus, D1, IF: 7.6)**.

[J3] **Talbi, D.**, Gál, Z.: Analysis of High-Speed Radio Communication in THz Bands: Topological Impacts and Signal Decomposition Using Empirical Mode Decomposition and Marginal Hilbert Spectrum. Lecture Notes on Data Engineering and Communications Technologies. 252, 59-71, 2025 **(Scopus, Q4).**

[J4] **Talbi, D.**, Daoui, Z., & Gal, Z. (2024). Unsupervised Machine Learning-Based Clustering of High-Frequency Radio Channel Properties: Analysis of Sector Communication Efficiency. Procedia Computer Science, 238, 306-313. (**Scopus**).

[J5] **Talbi, D.**, Gál, Z.: Integrating Reinforcement Learning into M/M/1/K Retry Queueing Models for 6G Applications. Sensors. 25 (12), 1-30, 2025. ISSN: 1424-8220. DOI: http://dx.doi.org/10.3390/s25123621, (2024) **(Q1, IF: 3.5).**

[C1] **D. Talbi**, M. A. Korteby and Z. Gal, "Neural Network Based Analysis of Terahertz Frequency Signal Propagation for B5G/6G Wireless Networks," *2022* IEEE 2nd Conference on Information Technology and Data Science (CITDS), Debrecen, Hungary, pp. 267-272, 2022 **(Scopus)**.

[C2] **D. Talbi** and Z. Gal, "Impact of Multi-Layer Recurrent Neural Networks in the Congestion Analysis of TeraHertz B5G/6G MAC Mechanism," 2022 International Conference on Software, Telecommunications and Computer Networks (SoftCOM), Split, Croatia, pp. 1-6, 2022 **(Scopus)**.

[C3] Gál, Z., **Talbi, D.**: "B5G/6G kommunikációs csatorna torlódásának elemzése mesterséges intelligenciával = Artificial Intelligence Based Analysis of the B5G/6G Communication Channel Congestion, " XXIII. Energetika-Elektrotechnika - ENELKO és XXXII. Számítástechnika és Oktatás : SzámOkt Multi-konferencia / szerk. Sebestyén-Pál György, Szabó Loránd. - p. 101-107, 2022.

[C4] **Talbi, D.**, Gál, Z.: "Localization Behaviour of the THz Radio Communication Based on Unsupervised Machine Learning, " Az elmélet és a gyakorlat találkozása a térinformatikában XIII.: Theory meets practice in GIS, Debrecen, 293-300, ISBN: 9789636150396, 2022.

[C5] **D. Talbi**, Z. Gal, "Entropy-Based Interdependence Analysis of the B5G/6G THz Network", Automation, Robotics & Communications for Industry 4.0/5.0 (ARCI' 2024): 4th IFSA Winter Conference, Barcelona, 170-176, (ISSN 2938-4796) ISBN: 9788409582198, 2024.

[C6] **Talbi, D.**, Gal, Z., "Analysis of the B5G/6G Communication Power Entropy Patterns Based on Generative AI Methods", 2024 IEEE 3rd Conference on Information Technology and Data Science (CITDS), Debrecen, Hungary, 2024 **(WoS)**.

[C7] Gál, Z., **Talbi, D.**, 'Analysis of Received Power Entropy Interdependence in B5G/6G Radio Cell', 2024 IEEE 13th International Conference on Cloud Networking (CloudNet), Piscataway, 1-6, ISBN: 9798350376562, 2024.

List of Own Publications not Referred in the Dissertation

[C8] Y. Mudhafar, **D. Talbi** and Z. Gal, "Neural Network Based Comparison of Real and Synthetic Data Series in TeraHertz Domain," 2022 IEEE 2nd Conference on Information Technology and Data Science (CITDS), Debrecen, Hungary, pp. 207-211, 2022 **(Scopus)**.

[C9] M. A. Korteby, **D. Talbi** and Z. Gal, "Fractals and Wavelets Based Energy Analysis of Cost-Balanced LEACH Sensor Network," 2022 IEEE 2nd Conference on Information Technology and Data Science (CITDS), Debrecen, Hungary, pp. 159-164, 2022.

[C10] **T. Djamila**, K. M. Amine, G. Zoltan, “Decomposition Based Congestion Analysis of the Communication in B5G/6G TeraHertz High-Speed Networks”, ABSTRACT, The 12th International Conference on Applied Informatics, Eger, Hungary, March 2-4,2023.

[C11] M. A. Korteby, **D. Talbi** and Z. Gal, " Effect of the Modulation on the Cluster Head Election in Cost Balanced LEACH”, ABSTRACT, The 12th International Conference on Applied Informatics, Eger, Hungary, March 2-4,2023.

[C12] **D. Talbi**, and Z. Gal, “High-Speed Communication Service Based on Low Earth Orbit Satellite Constellation ”, The meeting of theory and practice in GIS XIV. Theory meets practice in GIS, Debrecen, 291 - 301, ISBN: 9789636150846, 2023.

[C13] **D. Talbi**, M. Tourky, Z. Gál, “Localization Behavior of Swarm Intelligence Algorithms”, The meeting of theory and practice in GIS XIV. Theory meets practice in GIS, Debrecen, 303 – 311, ISBN: 9789636150846, 2023.

[C14] **D. Talbi**, Z. Gal, J. Sztrik, “Low Latency and High-Speed Communication Service with LEO Satellite Constellation”, IEEE, Information and Digital Technologies 2023, June 20th - 22nd, ISBN: 9798350305869 , p. 251-256, 2023 **(Scopus)**.

[C15] Z. Gal, **D. Talbi**, M. Tourky “On the Localization Properties of Swarm Intelligence Algorithms”, IEEE, Information and Digital Technologies 2023, ISBN: 9798350305869 , p. 97-104, 2023 **(Scopus)**.

[C16] Z. Gal, M. Korteby, **D. Talbi**, “Impact of Modulated Routing Mechanism on Wireless Sensor Network Systems: A Comprehensive Analysis”, IEEE, ICKII 2023, ISBN: 9798350323535, p. 70-76, 2023 **(Scopus)**.

[C17] Z. Gal, **D. Talbi**, L. Filep, “On the Required Iteration Number of the Representant Swarm Intelligence Algorithms Based on Coefficient of Variation”, IEEE Proceedings of 2023 9th International Conference ICOA, ISBN: 9798350312546, p. 1-6, 2023.

[C18] Gál, Z., **Talbi**, D., Korteby, M., “Entropy Analysis of Hierarchical Routing in Heterogeneous Wireless Sensor Network.” IEEE 5th Eurasia Conference on

IOT, Communication and Engineering (ECICE) / Meen, IEEE-INST ELECTRICAL ELECTRONICS ENGINEERS INC, Piscataway, 61-67, ISBN: 9798350314694, 2024. **(Scopus, Best Paper Award)**.

[C19] Gál, Z., **Talbi, D.**, "Insights into Low Earth Orbit Satellite Communication Dynamics: Quality of Service Analysis of Connection Behavior, Latency, and Doppler Shift", 2024 IEEE 4th International Conference on Electronic Communications, Internet of Things and Big Data. April 19-21, 2024 **(Best Paper Award)**.

[C20] Phoebe, G., **Talbi, D.**, Gál, Z., "Actual Trajectory and High Speed Internet Service Aspects of a Low Earth Orbit Satellite Constellation." Az elmélet és a gyakorlat találkozása a térinformatikában XV. = Theory meets practice in GIS. Debrecen, 21-29, ISBN: 9789634906193, 2024.

BIBLIOGRAPHY

[1] TALEB, Tarik, AGUIAR, Rui Luis, GRIDA BEN YAHIA, I., et al. White paper on 6G networking. 2020.Ali, S., Saad, W., & Steinbach, D. White Paper on Machine Learning in 6G Wireless Communication Networks. White paper. 6G Research Visions, No.7, June 2020.

[2] XIA, Qing, HOSSAIN, Zahed, MEDLEY, Michael, et al. A link-layer synchronization and medium access control protocol for terahertz-band communication networks. IEEE Transactions on Mobile Computing, 2019, vol. 20, no 1, p. 2-18.

[3] AKYILDIZ, Ian F., JORNET, Josep Miquel, et HAN, Chong. Terahertz band: Next frontier for wireless communications. Physical communication, 2014, vol. 12, p. 16-32.

[4] KOENIG, Swen, LOPEZ-DIAZ, Daniel, ANTES, Jochen, et al. Wireless sub-THz communication system with high data rate. Nature photonics, 2013, vol. 7, no 12, p. 977-981.

[5] SURESH, Krishnamoorthy, ALQAHTANI, Ali, RAJASEKARAN, Thangaraj, et al. Enhanced metaheuristic algorithm-based load balancing in a 5G cloud radio access network. Electronics, 2022, vol. 11, no 21, p. 3611.

[6] HAN, Chong, WU, Yongzhi, CHEN, Zhi, et al. Terahertz communications (TeraCom): Challenges and impact on 6G wireless systems. arXiv preprint arXiv:1912.06040, 2019.

[7] GHAFOOR, Saim, BOUJNAH, Noureddine, REHMANI, Mubashir Husain, et al. MAC protocols for terahertz communication: A comprehensive survey. IEEE Communications Surveys & Tutorials, 2020, vol. 22, no 4, p. 2236-2282.

[8] JIANG, Wei et SCHOTTEN, Hans D. Full-spectrum wireless communications for 6G and beyond: From microwave, millimeter-wave, terahertz to lightwave. In: 2023 IEEE 3rd International Conference on Computer Communication and Artificial Intelligence (CCAI). IEEE, 2023. p. 353-357.

[9] MAS, Lluís, VILAPLANA, Jordi, MATEO, Jordi, et al. A queuing theory model for fog computing. The Journal of Supercomputing, 2022, vol. 78, no 8, p. 11138-11155.

[10] KATAYAMA, Yukiko et TACHIBANA, Takuji. Optimal task allocation algorithm based on queueing theory for future internet application in mobile edge computing platform. Sensors, 2022, vol. 22, no 13, p. 4825.

[11] RODRIGUES, Tiago Koketsu, LIU, Jiajia, et KATO, Nei. Application of cybertwin for offloading in mobile multiaccess edge computing for 6G networks. IEEE Internet of Things Journal, 2021, vol. 8, no 22, p. 16231-16242.

[12] ROY, Arnab, PACHUAU, Joseph Lalnunfela, et SAHA, Anish Kumar. An overview of queuing delay and various delay-based algorithms in networks. Computing, 2021, vol. 103, no 10, p. 2361-2399.

[13] NAJIM, Ali Hamzah, MANSOUR, Hassnen Shakir, et ABBAS, Ali Hashim. Characteristic analysis of queue theory in Wi-Fi applications using OPNET 14.5 modeler. Eastern-European Journal of Enterprise Technologies, 2022, vol. 2, no 9, p. 116.

[14] MAZHAR, Tehseen, MALIK, Muhammad Amir, MOHSAN, Syed Agha Hassnain, et al. Quality of service (QoS) performance analysis in a traffic engineering model for next-generation wireless sensor networks. Symmetry, 2023, vol. 15, no 2, p. 513.

[15] PHUNG-DUC, Tuan, AKUTSU, Kohei, KAWANISHI, Ken'ichi, et al. Queueing models for cognitive wireless networks with sensing time of secondary users. Annals of Operations Research, 2022, vol. 310, no 2, p. 641-660.

[16] ADAMU, Aminu, SURAJO, Yusuf, et JAFAR, Muhammad T. SARED: Self-adaptive active queue management scheme for improving quality of service in network systems. Computer Science, 2021, vol. 22.

[17] AKAR, Nail et DOGAN, Ozancan. Discrete-time queueing model of age of information with multiple information sources. IEEE Internet of Things Journal, 2021, vol. 8, no 19, p. 14531-14542.

[18] MENG, Tianhui, ZHAO, Yubin, WOLTER, Katinka, et al. On consortium blockchain consistency: A queueing network model approach. IEEE Transactions on Parallel and Distributed Systems, 2021, vol. 32, no 6, p. 1369-1382.

[19] CARVALHO, Celso, MOTA, Edjair, FERRAZ, Eric, et al. Entropy based routing for mobile, low power and lossy wireless sensors networks. International Journal of Distributed Sensor Networks, 2019, vol. 15, no 7, p. 1550147719866134.

[20] ZHANG, Jing, LIN, Zhiwei, TSAI, Pei-Wei, et al. Entropy-driven data aggregation method for energy-efficient wireless sensor networks. Information Fusion, 2020, vol. 56, p. 103-113.

[21] LI, Lin et WANG, Juzhen. Research on feature importance evaluation of wireless signal recognition based on decision tree algorithm in cognitive computing. Cognitive Systems Research, 2018, vol. 52, p. 882-890.

[22] WANG, Zhong Lin. Entropy theory of distributed energy for internet of things. Nano Energy, 2019, vol. 58, p. 669-672.

[23] GABRIÉ, Marylou, MANOEL, Andre, LUNEAU, Clément, et al. Entropy and mutual information in models of deep neural networks. Advances in neural information processing systems, 2018, vol. 31.

[24] CECI, Michelangelo, CORIZZO, Roberto, MALERBA, Donato, et al. Spatial autocorrelation and entropy for renewable energy forecasting. Data Mining and Knowledge Discovery, 2019, vol. 33, no 3, p. 698-729.

[25] OMAR, Yamila M. et PLAPPER, Peter. A survey of information entropy metrics for complex networks. Entropy, 2020, vol. 22, no 12, p. 1417.

[26] XIE, Liang-Liang et KUMAR, Panganamala R. A network information theory for wireless communication: Scaling laws and optimal operation. IEEE transactions on information theory, 2004, vol. 50, no 5, p. 748-767.

[27] COON, Justin P. et SMITH, Peter J. Topological entropy in wireless networks subject to composite fading. In: 2017 IEEE International Conference on Communications (ICC). IEEE, 2017. p. 1-7.

[28] ALI, Aqib, ANAM, Sania, et AHMED, Muhammad Munawar. Shannon entropy in artificial intelligence and its applications based on information theory. Journal of Applied and Emerging Sciences, 2023, vol. 13, no 1, p. 09-17.

[29] COON, Justin P. et SMITH, Peter J. Topological entropy in wireless networks subject to composite fading. In: 2017 IEEE International Conference on Communications (ICC). IEEE, 2017. p. 1-7.

[30] T. Wang, M. Zhang, Q. Yu, H. Zhang. Comparing the applications of EMD and EEMD on time–frequency analysis of seismic signal. Journal of Applied Geophysics 83 (2012), pp. 29– 34, issn: 0926-9851, doi: https://doi.org/10.1016/j.jappgeo.2012.05.002.

[31] P. Seyrek, B. Şener, A. M. Özbayoğlu, H. Ö. Ünver. An Evaluation Study of EMD, EEMD, and VMD For Chatter Detection in Milling. Procedia Computer Science 200.C (Jan. 2022), pp. 160–174, issn: 1877-0509, doi: 10.1016/j.procs.2022.01.215.

[32] J.-M. Poggi. Empirical Mode Decomposition for Trend Extraction. Application to Electrical Data. in: 2010.

[33] S. Lu, X. Wang, H. Yu, H. Dong, Z. Yang. Trend extraction and identification method of cement burning zone flame temperature based on EMD and least square. Measurement 111 (2017), pp. 208–215, issn: 0263-2241, doi: https://doi.org/10.1016/j.measurement.2017 .07.047.

[34] Yaguo Lei, Zhengjia He, Yanyang Zi. Application of the EEMD method to rotor fault diagnosis of rotating machinery. Mechanical Systems and Signal Processing, Volume 23, Issue 4, 2009, pp. 1327-1338,issn 0888-3270. Doi: https://doi.org/10.1016/j.ymssp.2008.11.005.

[35] Tong Wang, Mingcai Zhang, Qihao Yu, Huyuan Zhang. Comparing the applications of EMD and EEMD on time–frequency analysis of seismic signal. Journal of Applied Geophysics, Volume 83, 2012, pp. 29-34, issn 0926-9851, doi: https://doi.org/10.1016/j.jappgeo.2012.05.002.

[36] L. Fangyu, Z. Bo, V. Sumit, M. Kurt. Seismic signal denoising using thresholded variational mode decomposition. Journal of Exploration Geophysics, Volume 49, 2018, issn 0812-3985, doi 10.1071/EG17004.

[37] S. Hadiyoso, E. M. Dewi, I. Wijayanto. Comparison of EMD, VMD and EEMD Methods in Respiration Wave Extraction Based on PPG Waves. Journal of Physics: Conference Series, Volume 1577, 2020, issn 1742-6596, doi 10.1088/1742-6596/1577/1/012040.

[38] S. Habib and A. Haque. Impulsive noise mitigation in wireless communication systems using EMD technique. 2012 7th International Conference on Electrical and Computer Engineering, Dhaka, Bangladesh, 2012, pp. 291-294, doi: 10.1109/ICECE.2012.6471543.

[39] Cao, Y., Ji, R., Huang, X., et al. Empirical Mode Decomposition-empowered Network Traffic Anomaly Detection for Secure Multipath TCP Communications. Mobile Network Application 27, 2254–2263 (2022). https://doi.org/10.1007/s11036-022-02005-6

[40] Mara, H.M., Elwekeil, M., Taha, T.E. et al. Hilbert Transform and Statistical Analysis for Channel Selection and Epileptic Seizure Prediction. Wireless Pers Commun 116, 3371–3395 (2021). https://doi.org/10.1007/s11277-020-07857-3.

[41] Daikoku, Kazuhiro. Hilbert transform applications in asynchronous demodulation for real zero single sideband signals in mobile radio path. Journal of Signal Processing 25.1 (2021).

[42] C. M. Melgoza et al. Wavelet Analysis Using Hilbert Transform and Matching Algorithm for Radar Receiver System. 2021 IEEE 11th Annual Computing and Communication Workshop and Conference (CCWC), NV, USA, 2021, pp. 0233-0237, doi: 10.1109/CCWC51732.2021.9375953.

[43] Huang, Kai, et al. A method for extracting fingerprint feature of communication satellite signal. Wireless Communications and Mobile Computing 2022.1 (2022): 7796017.

[44] J. Zheng et al. Time-Frequency Analysis of Scalp EEG With Hilbert-Huang Transform and Deep Learning. in IEEE Journal of Biomedical and Health Informatics, vol. 26, no. 4, pp. 1549-1559, April 2022, doi: 10.1109/JBHI.2021.3110267.

[45] Morteza Kamalian-Kopae, Anastasiia Vasylchenkova, Dmitry Shepelsky, Jaroslaw E. Prilepsky, and Sergei K. Turitsyn, Full-Spectrum Periodic Nonlinear Fourier Transform Optical Communication Through Solving the Riemann-Hilbert Problem. J. Lightwave Technol. 38, 3602-3615 (2020).

[46] E. T. Chelmiah and D. F. Kavanag. Hilbert Marginal Spectrum for Failure Mode Diagnosis of Rotating Machines. IECON 2021 – 47th Annual Conference of the IEEE Industrial Electronics Society, Toronto, ON, Canada, 2021, pp. 1-6, doi: 10.1109/IECON48115.2021.9589472.

[47] Zheng, J., Ying, W., et al. Multiscale three-dimensional Holo–Hilbert spectral entropy: a novel complexity-based early fault feature representation method for rotating machinery. Nonlinear Dyn 111, 10309–10330 (2023). https://doi.org/10.1007/s11071-023-08392-z.

[48] Sakar, C.O., Polat, S.O., Katircioglu, M. et al. Real-time prediction of online shoppers' purchasing intention using multilayer perceptron and LSTM recurrent neural networks. Neural Comput & Applic 31, 6893–6908, 2019.

[49] Tao Ren, Xuefeng Liu, Jianwei Niu, Xiaohui Lei, Zhao Zhang. Real-time water level prediction of cascaded channels based on multilayer perception and recurrent neural network. Journal of Hydrology, Volume 585, 2020.

[50] ALI K, Shoukath, KHAN, Arfat Ahmad, UR REHMAN, Ateeq, et al. Learned-SBL-GAMP based hybrid precoders/combiners in millimeter wave massive MIMO systems. Plos one, 2023, vol. 18, no 9, p. e0289868.

[51] Md. Kamrul Hasan, Md. Toufick E. Elahi, Md. Ashraful Alam, Md. Tasnim Jawad, Robert Martí. DermoExpert: Skin lesion classification using a hybrid convolutional neural network through segmentation, transfer learning, and augmentation. Informatics in Medicine Unlocked, Volume 28. 2022.

[52] Dario Jozinović, Anthony Lomax, Ivan Štajduhar, Alberto Michelini. Transfer learning: improving neural network-based prediction of earthquake ground shaking for an area with insufficient training data. Geophysical Journal International, Volume 229, Issue 1, April 2022.

[53] Santosh Kolagati, Thenuga Priyadharshini, V. Mary Anita Rajam. Exposing deepfakes using a deep multilayer perceptron – convolutional neural network model. International Journal of Information Management Data Insights, Volume 2, 2022.

[54] PIMPALKAR, Amit, et al. MBiLSTMGloVe: Embedding GloVe knowledge into the corpus using multi-layer BiLSTM deep learning model for social media sentiment analysis. Expert Systems with Applications, 2022, vol. 203, p. 117581.

[55] UTHANSAKUL, Peerapong, ANCHUEN, Patikorn, UTHANSAKUL, Monthippa, et al. Estimating and synthesizing QoE based on QoS measurement for improving multimedia services on cellular networks using ANN method. IEEE Transactions on Network and Service Management, 2019, vol. 17, no 1, p. 389-402.

[56] UTHANSAKUL, Peerapong, ANCHUEN, Patikorn, UTHANSAKUL, Monthippa, et al. QoE-Aware self-tuning of service priority factor for resource allocation optimization in LTE networks. IEEE Transactions on Vehicular Technology, 2019, vol. 69, no 1, p. 887-900.

[57] COLEMAN, Cody, KANG, Daniel, NARAYANAN, Deepak, et al. Analysis of dawnbench, a time-to-accuracy machine learning performance benchmark. ACM SIGOPS Operating Systems Review, 2019, vol. 53, no 1, p. 14-25.

[58] PSAROS, Apostolos F., MENG, Xuhui, ZOU, Zongren, et al. Uncertainty quantification in scientific machine learning: Methods, metrics, and comparisons. Journal of Computational Physics, 2023, vol. 477, p. 111902.

[59] LAKSHMANNA, Kuruva, KALURI, Rajesh, GUNDLURU, Nagaraja, et al. A review on deep learning techniques for IoT data. Electronics, 2022, vol. 11, no 10, p. 1604.

[60] LIU, Bai, XIE, Qiaomin, et MODIANO, Eytan. RL-QN: A reinforcement learning framework for optimal control of queueing systems. ACM Transactions on Modeling and Performance Evaluation of Computing Systems, 2022, vol. 7, no 1, p. 1-35.

[61] RAEIS, Majid, TIZGHADAM, Ali, et LEON-GARCIA, Alberto. Queue-learning: A reinforcement learning approach for providing quality of service. In : Proceedings of the AAAI Conference on Artificial Intelligence. 2021. p. 461-468.

[62] DAI, Jim G. et GLUZMAN, Mark. Queueing network controls via deep reinforcement learning. Stochastic Systems, 2022, vol. 12, no 1, p. 30-67.

[63] TAM, Prohim, ROS, Seyha, SONG, Inseok, et al. A survey of intelligent end-to-end networking solutions: Integrating graph neural networks and deep reinforcement learning approaches. Electronics, 2024, vol. 13, no 5, p. 994.

[64] KIM, Minsu, JASEEMUDDIN, Muhammad, et ANPALAGAN, Alagan. Deep reinforcement learning based active queue management for iot networks. Journal of Network and Systems Management, 2021, vol. 29, no 3, p. 34.

[65] [16] DU, Hongyang, ZHANG, Ruichen, LIU, Yinqiu, et al. Enhancing deep reinforcement learning: A tutorial on generative diffusion models in network optimization. IEEE Communications Surveys & Tutorials, 2024.

[66] [17] WALTON, Neil et XU, Kuang. Learning and information in stochastic networks and queues. In : Tutorials in Operations Research: Emerging Optimization Methods and Modeling Techniques with Applications. INFORMS, 2021. p. 161-198.

[67] Morales, Daniel & Jornet, Josep. ADAPT: An Adaptive Directional Antenna Protocol for medium access control in Terahertz communication networks. Ad Hoc Networks, vol.119, Mai 2021.

[68] Zahed Hossain, Qing Xia, Josep Miquel Jornet. TeraSim: An ns-3 extension to simulate Terahertz-band communication networks. Nano Communication Networks, vol.17, pp. 36-44, September 2018.

[69] Cover TM, Thomas JA. Entropy, relative entropy and mutual information. Elements of information theory 2 no. 1. 1991, p. 12-3.

[70] N. E. Huang, Z. Shen, S. R. Long, M. C. Wu, H. H. Shih, Q. Zheng, N.-C. Yen, C. C. Tung, H. H. Liu. The empirical mode decomposition and the Hilbert spectrum for nonlinear and non-stationary time series analysis. Proceedings of the Royal Society of London A: mathematical, physical and engineering sciences 454.1971 (1998), pp. 903–995.

[71] U. B. de Souza, J. P. L. Escola, L. da Cunha Brito. A survey on Hilbert-Huang transform: Evolution, chal lenges and solutions. Digital Signal Processing 120 (2022), pp. 103292, issn: 10512004, doi: https://doi.org/10.1016/j.dsp.2021.103292,

[72] AOUEDI, Ons, PIAMRAT, Kandaraj, HAMMA, Salima, et al. Network traffic analysis using machine learning: an unsupervised approach to understand and slice your network. Annals of Telecommunications, 2022, vol. 77, no 5, p. 297-309.

[73] ALRUBAYE, Jaafar Sadiq et SHAHGHOLI GHAHFAROKHI, Behrouz. Resource-aware DBSCAN-based re-clustering in hybrid C-V2X/DSRC vehicular networks. Plos one, 2023, vol. 18, no 10, p. e0293662.

[74] ZHUANG, Fuzhen, QI, Zhiyuan, DUAN, Keyu, et al. A comprehensive survey on transfer learning. Proceedings of the IEEE, 2020, vol. 109, no 1, p. 43-76.

[75] AMEER, Iqra, BÖLÜCÜ, Necva, SIDDIQUI, Muhammad Hammad Fahim, et al. Multi-label emotion classification in texts using transfer learning. Expert Systems with Applications, 2023, vol. 213, p. 118534.

[76] LU, Huiming, WU, Jiazheng, RUAN, Yingjun, et al. A multi-source transfer learning model based on LSTM and domain adaptation for building energy prediction. International Journal of Electrical Power & Energy Systems, 2023, vol. 149, p. 109024.

[77] KARAPANTELAKIS, Athanasios, ALIZADEH, Pegah, ALABASSI, Abdulrahman, et al. Generative AI in mobile networks: a survey. Annals of Telecommunications, 2024, vol. 79, no 1, p. 15-33.

[78] TAO, Zhenyu, XU, Wei, HUANG, Yongming, et al. Wireless network digital twin for 6G: Generative AI as a key enabler. IEEE Wireless Communications, 2024, vol. 31, no 4, p. 24-31.

[79] SATEA, Huda Dhari, IBRAHEM, Amer A., FAIQ, Maher, et al. Similarity measurement's comparison with mapping and localization in large-scale. In : AIP Conference Proceedings. AIP Publishing, 2023.

[80] SENIN, Pavel. Dynamic time warping algorithm review. Information and Computer Science Department University of Hawaii at Manoa Honolulu, USA, 2008, vol. 855, no 1-23, p. 40.

[81] BUZUTI, Lucas F. et THOMAZ, Carlos E. Fréchet AutoEncoder distance: a new approach for evaluation of generative adversarial networks. Computer Vision and Image Understanding, 2023, vol. 235, p. 103768.

[82] SARA, Umme, AKTER, Morium, et UDDIN, Mohammad Shorif. Image quality assessment through FSIM, SSIM, MSE and PSNR—a comparative study. Journal of Computer and Communications, 2019, vol. 7, no 3, p. 8-18.

[83] YANG, Mengmeng, GUO, Taolin, ZHU, Tianqing, et al. Local differential privacy and its applications: A comprehensive survey. Computer Standards & Interfaces, 2023, p. 103827.

[84] XU, Runhua, BARACALDO, Nathalie, et JOSHI, James. Privacy-preserving machine learning: Methods, challenges and directions. arXiv preprint arXiv:2108.04417, 2021.

[85] MOLTCHANOV, Dmitri, SOPIN, Eduard, BEGISHEV, Vyacheslav, et al. A tutorial on mathematical modeling of millimeter wave and terahertz cellular systems. arXiv preprint arXiv:2109.08651, 2021.

[86] KODA, Yusuke, OUYANG, Ruiting, OHMI, Norichika, et al. THz Deployments in 6G. Authorea Preprints, 2023.

[87] GOLOS, Elizaveta, DARASELIYA, Anastasia, SOPIN, Eduard, et al. Optimizing service areas in 6g mmwave/thz systems with dual blockage and micromobility. Mathematics, 2023, vol. 11, no 4, p. 870.

[88] MOLTCHANOV, Dmitri, SOPIN, Eduard, BEGISHEV, Vyacheslav, et al. A tutorial on mathematical modeling of 5G/6G millimeter wave and terahertz cellular systems. IEEE Communications Surveys & Tutorials, 2022, vol. 24, no 2, p. 1072-1116.

[89] WANG, Jun, WANG, Cheng-Xiang, HUANG, Jie, et al. A novel 3D non-stationary GBSM for 6G THz ultra-massive MIMO wireless systems. IEEE Transactions on Vehicular Technology, 2021, vol. 70, no 12, p. 12312-12324.

[90] SOPIN, Eduard, BEGISHEV, Vyacheslav, PROSVIROV, Vladislav, et al. The Impact of Traffic Characteristics on System and User Performance in 5G/6G Cellular Systems. arXiv preprint arXiv:2411.04474, 2024.